2023-05-12

Computational Study of Metal-Organic Frameworks for CO2 Capture and Reduction

Weerawardhena, Oshadhi Aishcharya

UNIVERSITY OF CALGARY

Computational Study of Metal-Organic Frameworks for CO_2 Capture and Reduction

by

Oshadhi Aishcharya Weerawardhena

A THESIS

SUBMITTED TO THE FACULTY OF GRADUATE STUDIES

IN PARTIAL FULFILMENT OF THE REQUIREMENTS FOR THE

DEGREE OF MASTER OF SCIENCE

GRADUATE PROGRAM IN CHEMISTRY

CALGARY, ALBERTA

MAY, 2023

Abstract

The escalating levels of carbon dioxide in the Earth's atmosphere present one of the most crucial environmental challenges facing humanity today. Carbon dioxide acts as a heat-trapping agent, leading to an increase in global temperatures. The consequences of unbridled carbon dioxide emissions are vast and concerning, encompassing the potential for widespread devastation to ecosystems, loss of biodiversity, and significant economic and social upheaval. Hence, it is imperative that we undertake meaningful steps to curtail our carbon emissions and reduce the impact of this critical environmental issue. To this end, various technologies have been developed, including carbon dioxide capture and reduction. However, the state-of-the-art catalysts for both these technologies are often expensive and exhibit low selectivity.

This thesis endeavors to identify alternative Metal Organic Framework based catalysts for both the capture and reduction of carbon dioxide. Metal Organic Frameworks present an excellent alternative due to their tunability. To assess the ability of the HCALF-50 and CALF-50 MOFs for carbon dioxide capture, Molecular Dynamics Simulations were employed. It was discovered that both systems, especially CALF-50, were unstable due to temperature variations. Nonetheless, the use of template molecules allowed the systems to retain their configurations. Regrettably, neither system proved capable of capturing carbon dioxide, as determined by the diffusion of carbon dioxide between the pores of both systems.

The Computation-Ready Experimental Metal-Organic Framework database was utilized to identify Metal Organic Frameworks for the reduction reaction. For this reaction, the focus was on the two-electron reaction since carbon monoxide is a precursor to the

production of syngas. Three Zeolitic Imidazolate Frameworks, specifically ZIF-8, ZIF-70, and ZIF-82, were identified and studied using Density Functional Theory. It was determined that the newly identified ZIF-70 and ZIF-82 were not suitable candidates towards the production of carbon monoxide, and preferentially produced hydrogen gas.

Consequently, the findings of this study indicate that HCALF-50 and CALF-50 are inadequate for capturing carbon dioxide, while two catalysts, ZIF-70 and ZIF-82, have been identified as unsuitable catalysts for the reduction reaction to carbon monoxide.

Keywords: Carbon dioxide; Carbon dioxide Capture; Carbon dioxide Reduction Reaction; Metal Organic Framework; Zeolitic Imidazolate Framework

Preface

This thesis is original, unpublished, independent work by the author, O. A. Weerawardhena.

Chapter 3 is a computational study based on experiment conducted by David Evans, Racheal Huynh and Dr. George Shimizu.

Acknowledgements

This research was undertaken, in part, thanks to funding from the Canada First Research Excellence Fund (CFREF) program. I also acknowledge the computational resources and technical support provided by Advanced Research Computing (ARC) Services group at the University of Calgary and Compute Canada (www.computecanada.ca). I would like to thank my university, University of Calgary, for providing me with the opportunity of pursuing a master's in science. This degree has allowed me to gain knowledge in fields such as programming and computational chemistry. It has also led me to work on and write the thesis as presented here.

I would like to give a special thanks to my supervisor, Dr. Samira Siahrostami, for taking me under her wing and guiding me through this stage of my life. Her supervision and guidance were vital for helping me learn how to lead a project independently and teaching me professional skills which I will continue to use going forward. I am also grateful for her continuous support and assistance with any questions I had, and for giving me advice I will never forget. Her support was critical in ensuring the success of my thesis.

I would also like to thank my family for always supporting me and keeping me focused on my thesis. I am incredibly grateful for their presence in my life and the role they have played in helping me achieve this accomplishment. Their belief in me and their support have been invaluable, and I am forever grateful for their unwavering presence in my life. Without them, I would not be where I am today.

I would like to express my deepest gratitude to my boyfriend for his unwavering emotional support throughout my academic journey. His constant encouragement, understanding, and patience have been a source of strength and motivation. I cannot

thank him enough for being there for me during the ups and downs of this challenging process.

Table of Contents

List of Tables

List of Figures

List of Symbols, Abbreviations and Nomenclature

Acronym	Meaning
CO_2	Carbon Dioxide
CO	Carbon Monoxide
CO_2RR	Carbon Dioxide Reduction Reaction
MOF	Metal Organic Framework
ZIF	Zeolite Imidazolate Framework
MD	Molecular Dynamics
HAC	Hexaaquachromium (III)
CoRE MOFs	Computation-Ready Experimental Metal-Organic Framework
PLD	Pore Limiting Diameter
DFT	Density Functional Theory
HOMO	Highest Occupied Molecular Orbital
LUMO	Lowest Unoccupied Molecular Orbital

Symbol	Meaning
E^o	Standard Electrode Potential
U	Applied Potential
η	Overpotential
U_L	Limiting Potential

1 Introduction

In this chapter, we will discuss the motivation behind the research that was conducted (1.1), which focuses on the negative effects of carbon dioxide (CO_2) in the atmosphere. Then we will go over current methods to resolve this issue, including CO_2 capture (1.1.1) and the CO_2 reduction reaction (CO_2RR) (1.1.2). We will also discuss a proposed catalyst that can be used for both CO_2 capture and reduction, known as Metal-Organic Frameworks (MOFs) (1.1.3). We will then go over the current state-of-the-art MOFs (1.2) that's utilized for CO_2 capture (1.2.1) and reduction (1.2.2). We will go over the problems (1.3) associated with these MOFs in CO_2 capture (1.3.1) and reduction (1.3.2). Following that, we will go over the objectives of this thesis (1.4) and the expected outcomes (1.5). Lastly, the structure of this thesis is presented (1.6).

1.1) The Current Issue with CO_2 Emissions

Since the industrial revolution, humans have increasingly turned to fossil fuels as a major source of world energy supply.[1] The biggest issue associated with the combustion of fossil fuels is the release of greenhouse gases, such as CO_2 and CH_4 in the atmosphere, which trap some of the Sun's energy emitted by the Earth's surface, resulting in an increase in Earth's temperature.[2,3] CO_2 possesses the capacity to absorb infrared radiation (IR), undergo vibrational activity, and subsequently re-emit it in a shorter wavelength.[4] This process results in the entrapment of IR within the atmosphere, leading to the Earth's temperature increase.[4] Despite the increasing usage of alternative and renewable sources of energy, such as wind, solar and geothermal, there is still a major dependence on fossil fuels. [1,2,5]

According to data from the National Oceanic and Atmospheric Administration, by the end of 2020, there was a concentration of 415 ppm of CO_2 in the atmosphere.[6] Radiative Forcing looks at the solar energy imbalance of the Earth's system due to some imposed perturbation.[7–9] When the radiative forcing is greater than zero, it has a warming effect; when it is lower than zero, it has a cooling effect.[7–9] The Annual Greenhouse Gas Index (AGGI) was created in 2006, which looks at the influence of greenhouse gases in the warming of the planet and is an index of radiative forcing compared to the year 1990.[7–9] In 2020 the AGGI was at 1.47, meaning there was a 47% increase in the influence of greenhouses gases on the warming of the planet since 1990, when the AGGI was 1, with CO_2 accounting for 80% of this increase.[10] For comparison, it took 240 years for the AGGI to go from 0 to 1, but it only took an additional 30 years for it to go from 1 to nearly 1.5,[10] showcasing the dramatic increase of greenhouse gases and their respective impact on Earth's rising temperature. Thus, it is imperative to reduce the impact of CO_2 on Earth, by employing an array of methods and technologies, as shown in Figure 1.

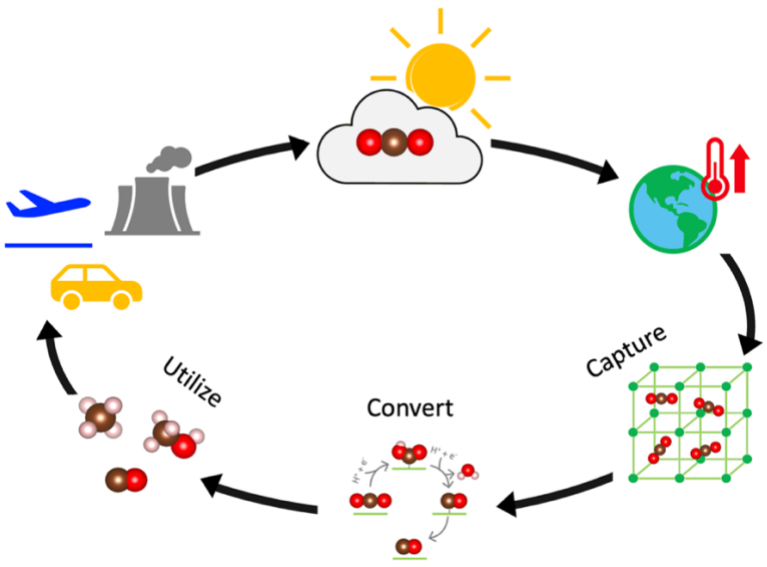

Figure 1: Methods of decreasing the impact of CO_2 on Earth

1.1.1) A Brief Introduction to CO_2 Capture Technologies

Different technologies have been developed in the past decade to reduce the CO_2 concentration in the atmosphere. One technology which has been implemented to reduce the impact of CO_2 is Carbon Capture and Storage (CCS), which allows for the continued use of fossil fuels while reducing greenhouse gas emissions.[11] In the CCS, the CO_2 is captured at the source of emissions like power plants,[11,12] the cement industry,[13] the iron and steel sector,[14] petroleum refineries,[15] and the chemical industry.[16] The captured gas would then be pressurized to about 100 bar before being transported and stored underground.[11,17] Unfortunately, the capture of the CO_2 is very expensive, as a result of the reduced plant efficiency and the increased costs related to investment, maintenance, transportation and storage.[11]

Currently, there is post-combustion capture, pre-combustion capture and oxy-combustion.[2] Post-combustion capture involves separating the CO_2 from combustion exhaust gases using liquid solvents or other methods.[2] Pre-combustion capture entails converting the fuel into a gaseous mixture of both CO_2 and hydrogen, where the hydrogen is separated by burning, and the CO_2 is then compressed and transported to storage.[2] Oxy-fuel combustion uses oxygen for combustion of the fuels, producing exhaust gas which is comprised of water vapour and CO_2, which can then easily be seperated.[2] Figure 2 demonstrates how these processes occur.

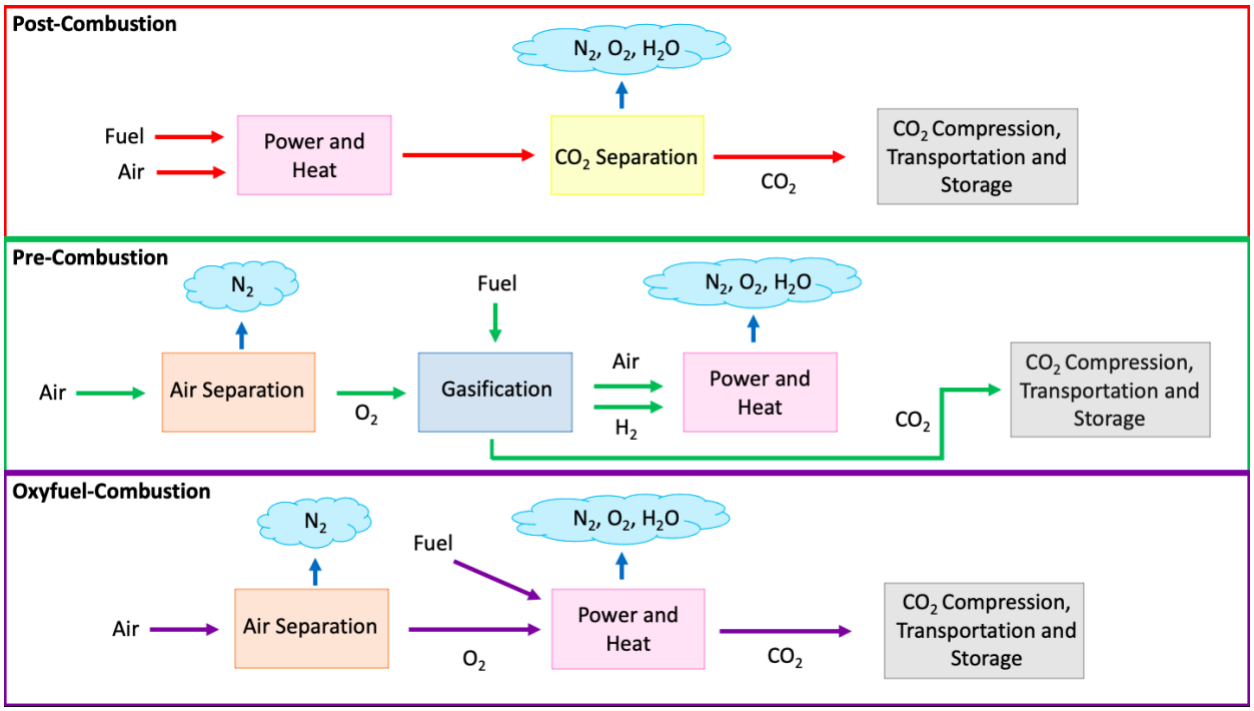

Figure 2: Summarization of CO_2 capture technologies, including post-combustion, pre-combustion, and oxy-fuel combustion.

Out of the three methods of capturing CO_2, only the post-combustion and pre-combustion capture requires a capture system. Possible capture systems include chemical absorption,[14,15] physical adsorption,[2,18] membrane,[12,19,20] biological capture,[21,22] cryogenic capture,[20,23] liquid amines, [20,24] chemical and calcium looping.[25] The advantages and disadvantages of these methods are summarized in Table 1, and their examples are shown in Figure 3.

Table 1: Advantages and disadvantages of current methods for capturing CO_2.

Technology	Advantages	Disadvantages	Reference
Chemical Absorption	● High capacity at low pressures	● Regeneration is energy intensive ● Corrosion ● Absorbent degradation ● High cost	2,14,15,18
Physical Absorption	● High capacity at low temperature and high pressure ● Cheap solvent	● Low selectivity ● Requires a high energy ● Low capacity at high temperature and low pressure ● Absorbent loss	2,18
Amine sorbent	● Low waste generation ● High capacity at low pressure ● High selectivity ● Works in mild conditions ● Less corrosion	● High energy consumption ● Performance loss with cycles ● Thermal and oxidative degradation ● Contaminant-induced degradation ● High heat required	2,18,20,24,26
Membrane	● Low operating cost ● Easy to handle and operate	● High cost for manufacture ● Low separation selectivity	2,12,19,20
Biological absorption	● No hazardous chemicals used	● Long-time required ● Large area required ● Can affect biological diversity	2,21,22
Cryogenic separation	● Coproduction of food and biofuels ● High capture efficiency	● Sensitive to other flue gas contaminants and culture conditions ● High energy required ● Pre-removal of moisture required	2,20,23
Chemical and Calcium Looping	● Efficient heat recovery ● Pellets can be used continuously ● Low cost ● No energy required to separate CO_2	● High temperature required ● Energy penalties present ● Quality of CaO effects CO_2 capacity and reaction rate	17,25,27

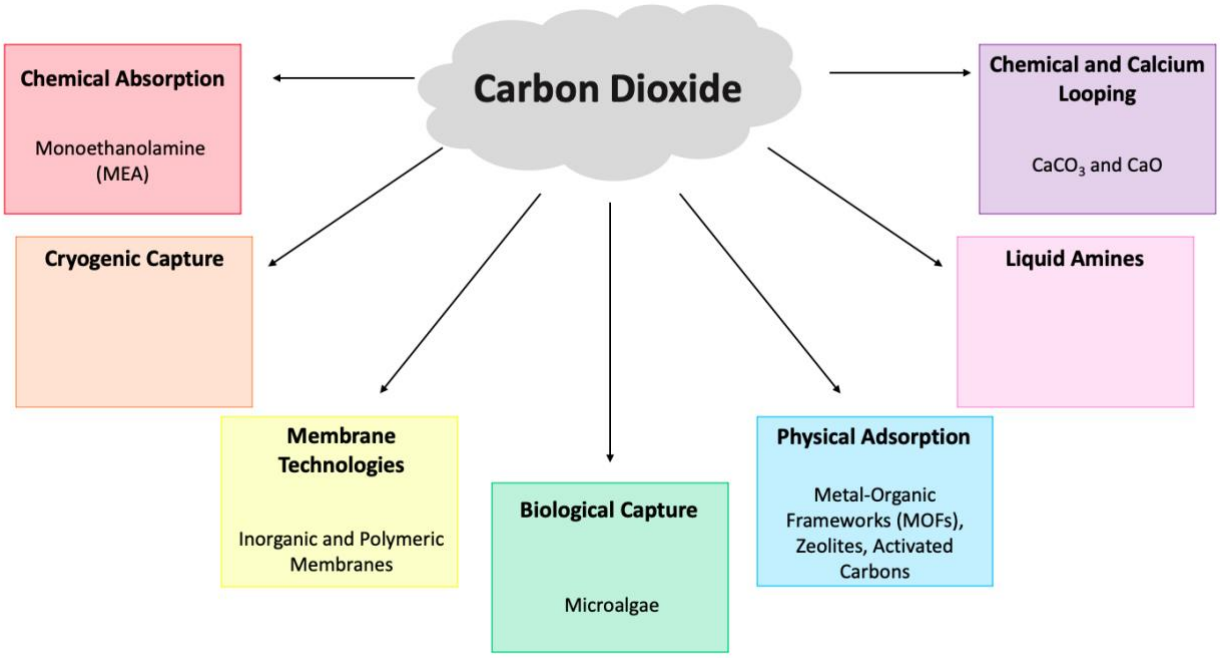

Figure 3: Current methods, and their examples, for CO_2 capture

An alternative to these methods is the use of sorbent materials. Sorbent materials have the capability of adsorbing and/or absorbing liquids and gases.[28] In order to select the sorbent material to use in CO_2 capture, the following criteria must be considered: adsorption capacity for CO_2, selectivity for CO_2, adsorption/desorption kinetics for CO_2, mechanical strength of the sorbent particles, chemical stability, tolerance to impurities, regeneration of sorbents, sorbent costs and working CO_2 capacity.[29,30]

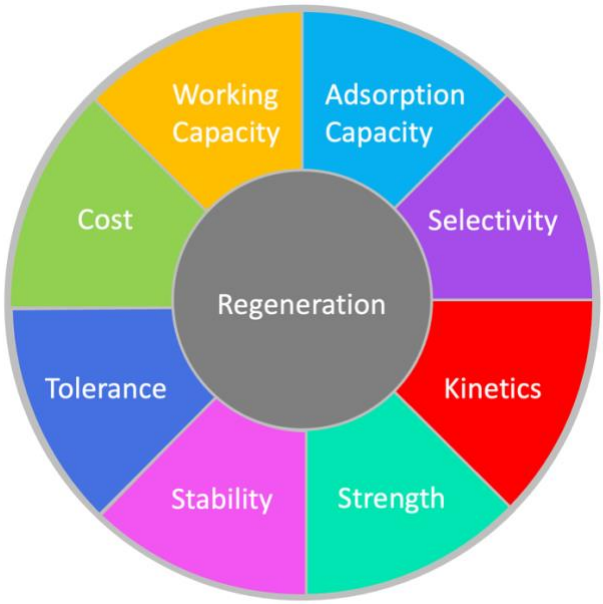

Figure 4: Criteria for identifying the best sorbent materials for CO_2 capture.

The adsorption capacities of these sorbents can be improved via amine functionalization,[31] as well as nitrogen doping.[32] Nitrogen doping, in particular, improves the electron density of the sorbent material, thereby increasing the basicity, thus enabling the electron deficit CO_2 to anchor onto the pore surface through Lewis acid/base interactions.[32] Many different physical sorbent materials such as activated carbon,[30,33,34] carbon molecular sieves,[35,36] zeolites,[30,37] metal oxides,[29] and metal-organic frameworks (MOFs),[29,30] have been proposed and examined in the literature during the past decades. The advantages and disadvantages of various physical sorbent materials can be found in Table 2. Among different classes of the sorbent materials introduced above, we will focus on MOFs which have shown a great promise for CO_2 capture in recent years.[29,38–41]

Table 2: Advantages and disadvantages of sorbent materials for capturing CO_2.

Technology	Advantages	Disadvantages	Reference
General Physical Adsorbents	• High capacity at low temperature and high pressure • Low waste generation	• Low CO_2 selectivity • Capture capacity decreases with temperature • Requires a high pressure • Moisture degradation of performance	2,18
Activated Carbons	• Low cost • Fast adsorption kinetics • Low regeneration energy	• Low CO_2 selectivity • Capture capacity decreases with temperature • Unfavourable adsorption isotherms • Competitive binding with water	30,33,34
Carbon Molecular Sieves	• High selectivity • High capacity	• Capture capacity decreases with temperature • Micro-pore diffusion is rate limiting	35,36
Zeolites	• High selectivity • Fast adsorption kinetics • Capacity increases with pressure	• Competitive binding with water • Capture capacity decreases with temperature	30,37
Metal Oxides	• High abundance • Low toxicity • Cost-effective	• Slow chemical reaction • Desorption requires high temperatures • Energy intensive	29

1.1.2) A Brief Introduction to the CO_2 Reduction

The CO_2 molecules can be converted to useful chemicals through chemical conversion,[42,43] biological transformation,[44] photocatalytic,[45,46] and electrocatalytic reduction.[47] Among these methods, electrochemical reduction of CO_2 (CO_2RR) has emerged as the most promising due to its several advantages.[47] Firstly, renewable but intermittent energy sources, such as solar, wind, tidal, or geothermal power, can be used as the driving force for reducing CO_2 to valuable products.[47] Secondly, the products obtained from CO_2RR are either fuels or important chemicals that are compatible with existing industries.[47] Thirdly, the process is controllable and can be carried out under mild reaction conditions.[47] Lastly, electrocatalysis systems are simple and easy to scale-up.[47]

However, CO_2RR kinetics are limited by high activation barriers and multiple electron transfer steps that result in high overpotentials and poor selectivity.[48,49] Hence, the development of efficient electrocatalysts is critical for the success of CO_2RR processes. Various electrocatalysts have been widely studied in the literature, including metal-organic complexes,[50,51] metal-based materials such as metals, metal oxides, metal alloys, metal chalcogenides,[49,52–54] and metal-free carbon-based materials.[55] The electrocatalytic reduction of CO_2 involves two half reactions,[56] that occur through a two to fourteen-electron exchange process, as shown in Figure 5.

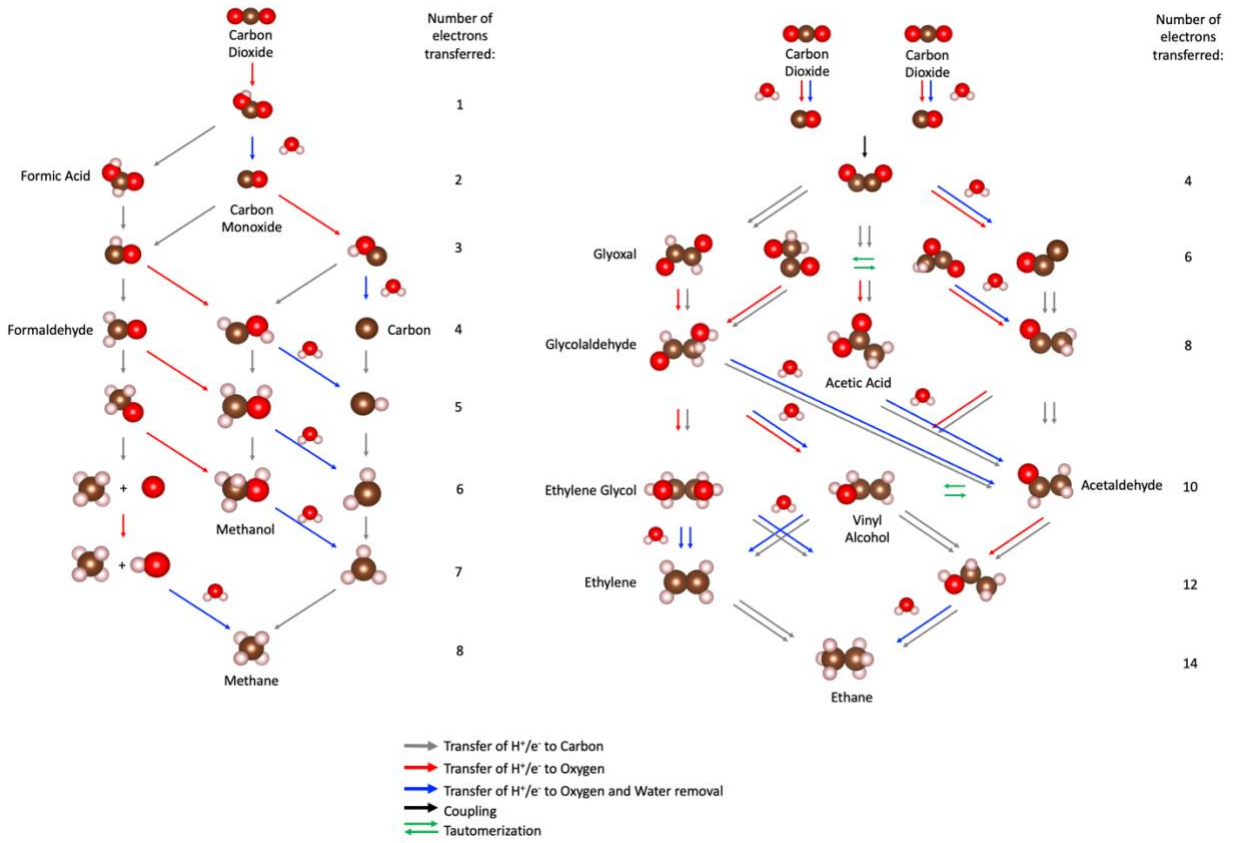

Figure 5: Mechanism for the CO_2 Reduction Reaction

The CO_2RR can produce a variety of valuable chemicals, including CO, H_2, methanol, formic acid, and ethylene. The product distribution is highly dependent on the electrode material, operating conditions, and the applied potential. For example, copper-based electrocatalysts tend to produce CO with high selectivity, while silver-based electrocatalysts tend to produce H_2 with high selectivity.[57] The production of methanol, formic acid, and ethylene requires further optimization of the CO_2RR process, including the selection of appropriate electrocatalysts and operating conditions.

Syngas is a versatile gas mixture composed mainly of carbon monoxide (CO) and hydrogen (H_2), with smaller amounts of CO_2 and other gases such as nitrogen (N_2) and methane (CH_4).[58] It can be used as a fuel in many applications, including power generation, transportation, and chemical synthesis.[58,59] One of the most promising applications of syngas is as a feedstock for the production of valuable chemicals, such as methanol and other alcohols, that can be used as fuels or precursors for other chemicals,[59] done via the Fischer-Tropsch process.[60] There are several methods for producing syngas, including steam methane reforming (SMR), partial oxidation of hydrocarbons, and gasification of coal or biomass.[58,59,61,62] SMR is the most widely used method for syngas production and involves reacting methane with steam to produce hydrogen and carbon monoxide.[61,62] However, SMR is a carbon-intensive process that produces a significant amount of CO_2 as a byproduct, contributing to greenhouse gas emissions (Figure 6).[62]

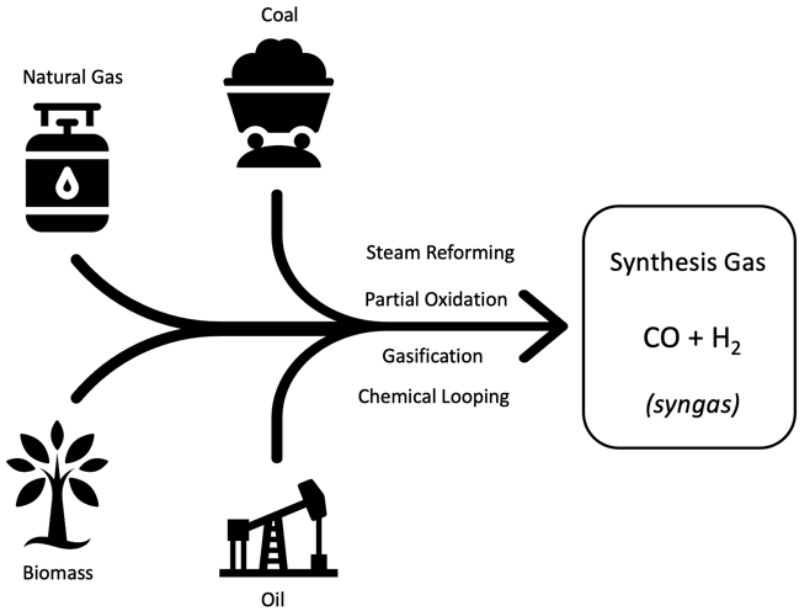

Figure 6: Production of syngas using natural gas, coal, biomass, and oil sources.

The electrochemical production of syngas has gained significant attention as a promising application of CO_2RR,[63] as it is possible to selectively tune the reaction to produce a mixture of CO and H_2.[63] The CO_2RR process is a more favorable method for producing syngas due to its potential to mitigate carbon emissions and provide a sustainable route for producing chemicals (Figure 7). Moreover, the electrochemical production of syngas has several advantages over traditional syngas production methods, such as steam methane reforming, including lower energy consumption, higher selectivity, and more flexible operation.[47,63,64] To achieve high selectivity and activity for the electrochemical production of syngas, efficient electrocatalysts are required.[63]

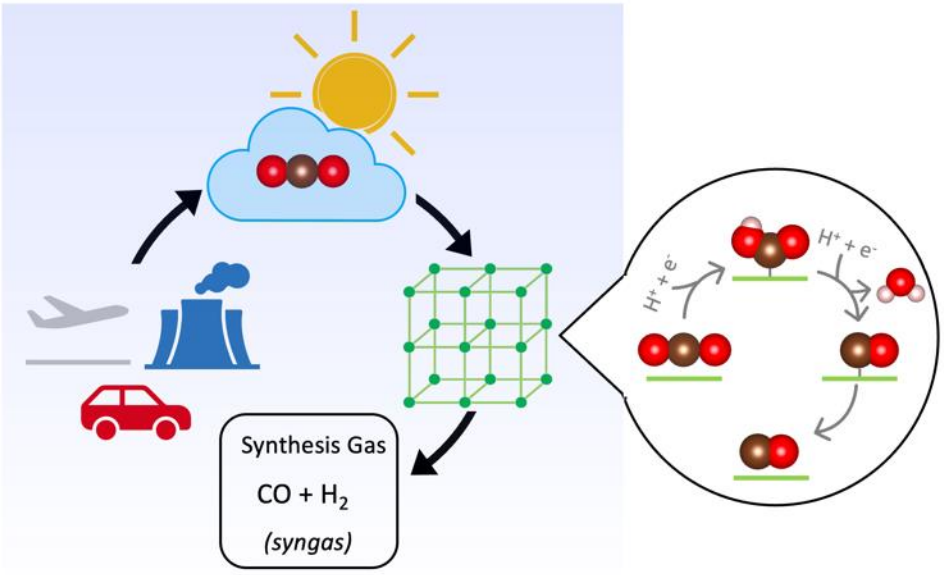

Figure 7: Production of syngas utilizing the CO_2 reduction reaction with a metal-organic framework catalyst.

1.1.3) Metal-Organic Frameworks as a Possible Catalyst

Metal-organic frameworks (MOFs), also known as porous coordination polymers,[65] are a class of materials consisting of metal ions or clusters coordinated to organic ligands,[66] forming three-dimensional networks with high porosity and surface area. Figure 8 shows the formation of MOFs using metal ions and organic linkers. The ability to control the pore size, shape, and the chemical potentials of adsorbing surfaces results in the ability to control the selectivity, kinetics, and capacities of the MOFs.[30]

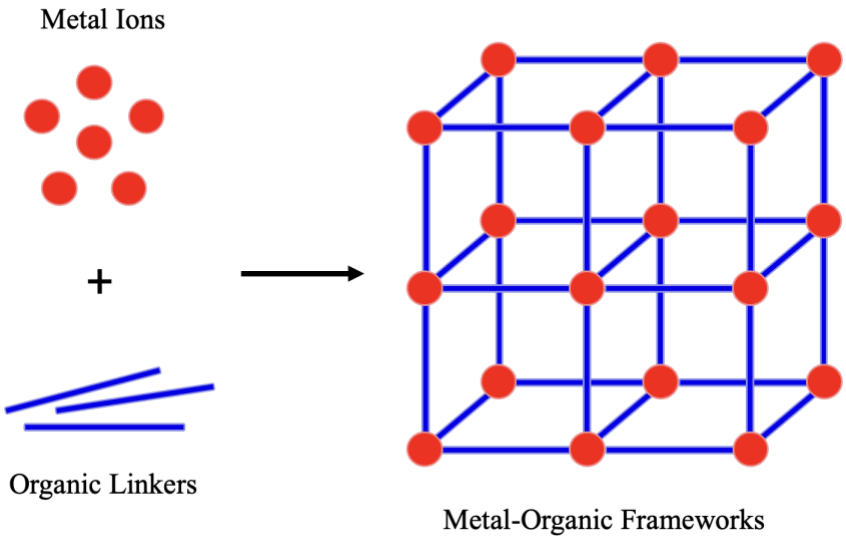

Figure 8: Illustration of MOF formation.

The first report on MOFs dates to the early 1990s, where researchers synthesized a porous coordination polymer using $Cu(NO_3)_2$ and pyrazine ligands.[67] Since then, MOFs have been extensively studied due to their unique properties and potential applications in gas storage,[68] separation,[69] heterogeneous catalysis,[70] sensing,[71] and luminescence.[72]

MOFs gained widespread attention in the early 2000s after the discovery of MOF-5, which had a surface area of over 5000 m^2/g.[73] This sparked a new wave of research in MOFs, leading to the synthesis of thousands of new MOFs with varying structures, compositions, and properties.

The development of MOFs has also been driven by advances in synthetic chemistry and characterization techniques, such as X-ray crystallography, gas sorption, and spectroscopy.[74–77] These tools have allowed researchers to tailor the properties of MOFs for specific applications, such as selective gas adsorption, [68] catalysis, [70] and drug delivery.[78]

Sub-classes of MOFs include zeolitic imidazolate frameworks (ZIFs), [79–83] covalent organic frameworks (COFs),[84–87] Materials Institute Lavoisier (MILs),[79,88–90] iso-reticular metal–organic frameworks (IR-MOFs),[79] porous coordination networks (PCNs),[79,91–94] porous coordination polymers (PCPs),[79,95–98] and hydrogen bonded organic frameworks (HOFs or HMOFs).[99,100]

There are many advantages associated with utilizing MOFs, including their high surface area,[29,30,76] tailorable pore size and shape,[29,30,77] high selectivity, [29,30,101] structural diversity, [29,30,77] environmental sustainability,[29,30,102] and versatility.[29,30,78,103] Unfortunately, they also have some issues with stability,[30,77] synthesis,[104,105] cost,[77] toxicity,[103] and scalability.[77] The benefits of utilizing MOFs outweighs their costs, thus allowing us to study MOFs for both the capture and reduction of CO_2.

1.2) State of the Art

In this section we will go over the current state-of-the-art MOF-based catalysts for both CO_2 capture (1.2.1) and reduction (1.2.2).

1.2.1) Current State of the Art MOFs for CO_2 Capture

There are several MOFs that have been identified as promising materials for CO_2 capture. One of the most widely studied MOFs for this application is MOF-74, which has demonstrated high CO_2 uptake capacity and selectivity over other gases, such as N_2 and CH_4, due to the presence of unsaturated metal sites in the structure.[106] MOF-74 is a highly porous MOF with a tetrahedral structure composed of metal clusters and organic linkers.[106] Another MOF that has shown promise for CO_2 capture is UiO-66, a zirconium-based MOF which has a high surface area, high thermal stability and can be readily synthesized in large quantities.[107,108] It has been shown to have a high CO_2 adsorption capacity and good selectivity for CO_2 over N_2 and CH_4 due to its open metal sites and polarizable zirconium nodes.[107,108] Other MOFs that have been studied for CO_2 capture include MIL-101,[109] ZIF-8,[110–112] and NOTT-300.[113] In addition, MIL-101(Cr) has been identified as a promising MOF for CO_2 capture due to its high surface area, tailorable pore size, good stability, and high CO_2 adsorption capacity and selectivity.[109,114] Soltanolkottabi et al. (2019) found that MIL-101(Cr) had excellent CO_2 capture performance with a CO_2 uptake capacity of 7.7 mmol/g at 298 K and 1 bar.[115] ZIF-8 is a zeolitic imidazolate framework with a high surface area and high thermal stability. It has been shown to have a high CO_2 adsorption capacity and good selectivity for CO_2 over N_2 and CH_4 due to its small pore size and strong interaction with CO_2.[110–112] NOTT-300 is a nickel-based MOF with a high

CO_2 adsorption capacity and selectivity due to its open metal sites and polarizable nickel nodes.[113,116] Mu et al. (2015) reported that NOTT-101 exhibited high selectivity for CO_2 over N_2 and CH_4, with a CO_2 uptake capacity of 3.92 mmol/g at 293 K and 1 bar.[116] These MOFs have been found to have some of the highest CO_2 adsorption capacities at 298 K and 1 bar, [117] of which Mg-MOF-74 was shown to have the highest at 8.6 mmol/g. [118]

The M-MOF-74 (M = metal) series have been studied for their high performance in gas separation and hydrogen storage.[119–122] Out of the different metals in the series, the Mg-MOF-74 (or CPO-27-Mg; [Mg2(DOT); DOT: 2,5-dioxidoterephthalate]) has the largest CO_2 capacity and selectivity over other gases.[123,124] This MOF has a five-coordinate square-pyramidal geometry around the Mg sites, and the bond angles at these sites are constrained, resulting in the Mg coordination sphere being available to adsorb other gases.[125]

Figure 9 shows the CO_2 uptake capacities of different M-MOF-74 (M = Zn, Co, Ni, and Mg). The blue line shows the CO_2 uptake capacities at 0.1 bar and 296 K,[119] while the orange line shows the uptake capacities at 0.15 bar and 298 K.[106] As can be seen in the chart, the Mg-MOF-74 outperforms all other M-MOF-74s, further displaying the high CO_2 adsorption capacity of this MOF.

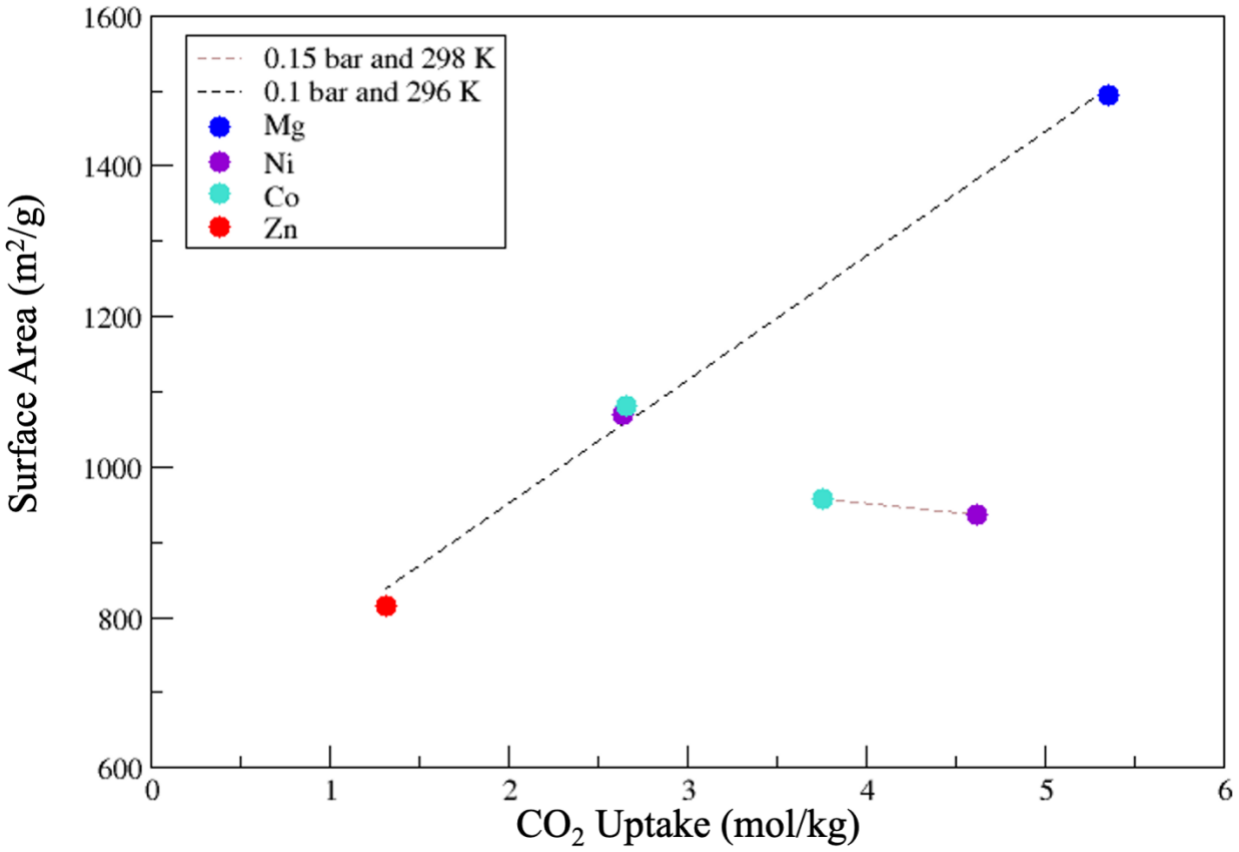

Figure 9: The CO_2 uptake of MOF-74 using Zinc, Cobalt, Nickel, and Magnesium, with different surface areas and at different temperatures and pressures.

1.2.2) Current State of the Art MOF-Based Catalysts for CO_2 Reduction

Due to their high surface area and their tunable chemical structures, MOFs have become an interesting catalyst for the CO_2RR. The structured and permeable heterogeneous network enables unrestricted diffusion of electrolytes, counter ions, and dissolved CO_2 into the inner core of the MOF.[126] Additionally, MOFs are commonly made up of elements that are readily available, including Fe, Co, Cu, Ni, and Mn, along with organic ligands comprising of C, H, O, and N. [126] The wide range of inorganic building blocks and organic ligands provides the opportunity to precisely fine-tune the properties of MOFs, thereby optimizing the pore size and reactant diffusion while also enhancing the

affinity towards important intermediates.[126,127] MOFs can be used as the precursor of electrocatalysts, the electrocatalyst and supports, where Table 3 shows the activity of MOF electrocatalysts.[126]

Table 3: Summary of CO_2RR activity towards the production of CO with recent reported MOF-based electrocatalysts.

MOF	Potential (V)	Faradaic Efficiency (%)	Reference
ZIF-Fe-CNT-FA-p	-0.86	100	[128]
CoPc derived Co−N_5/HNPCSs	-0.73	99.2	[129]
M-PMOF	-0.8	98.7	[130]
CoPP@CNT	-0.49	98.3	[131]
Ni_2-CPD_{py}	-0.8	94	[132]
Co/Zn ZIFs derived Co-N_2	-	94	[133]
Re-SURMOF	-1.6	93	[134]
C-AFC@ZIF-8	-0.6	93	[135]
CoPc/CNT	-0.63	92	[136]
ZIF-8 derived Fe-N-C	-0.6	91	[137]
Ligand-doped ZIF	-1.1	90.57	[138]
Zn-ZIF	-1.1	81	[139]
Ag_2O/layered ZIF	-1.2	80.6	[140]
$Al_2(OH)_2$TCPP-Co	-0.7	76	[141]
ZIF-8 derived Ni SAs/N-C	-1.0	71.9	[142]
ZIF-8	-1.8	65.5	[143]
Fe-MOF-525/FTO	-	41	[144]

Overall, these MOFs offer promising potential for the electrochemical reduction of CO_2, and further research is needed to optimize their properties and develop practical applications for this technology.

1.3) Problem

Although the identified state-of-the-art MOFs are viable options for both CO_2 capture and reduction, there are several problems associated with them. These issues will be discussed in sections focusing on CO_2 capture (1.3.1) and reduction (1.3.2), respectively.

1.3.1) Issues Associated with MOFs Utilized for CO_2 Capture

Many MOFs are prone to degradation in the presence of moisture or high temperatures, which limits their practical applications. [145,146] For example, UiO-66 has been reported to degrade under humid conditions, leading to a decrease in its CO_2 adsorption capacity.[147] MOF-74 is also not water stable, and instead has a high water affinity which makes the MOF undergo structural and chemical transformations at ambient temperatures, in the presence of water.[146,148–150] Another issue of MOF-74 is that it forms a weak physisorption with CO_2, thus making this MOF suitable for low temperature and pressure environments, thus restricting the practical applications of this system.[151] The reproducibility of MOF synthesis can be a challenge, as slight variations in the synthetic conditions can lead to significant changes in the final material properties. This can make it difficult to scale up MOF synthesis for large-scale applications. For example, the synthesis of ZIF-8 can be sensitive to slight variations in temperature, pressure, and reaction time, which can affect its crystal size and morphology.[152] Moreover, some MOFs may contain toxic or environmentally harmful components, such as heavy metals or organic solvents, which can raise concerns about their potential impact on human health and the environment. For example, the synthesis of MOF-74 typically involves the use of

dimethylformamide (DMF), which is a toxic and potentially carcinogenic solvent.[153] Finally, the production of MOFs can be relatively expensive, particularly when compared to other porous materials like activated carbon or zeolites. The cost of MOFs can be influenced by factors such as the cost of raw materials, energy consumption during synthesis, and the complexity of the synthetic process.[105] Due to these issues, it is important to identify another MOF that can be used for the efficient capture of CO_2.

1.3.2) Issues Associated with the Current Catalysts for CO_2 Reduction

The electrochemical conversion of CO_2 into reduced carbon species is the first step in reducing CO_2, but it is difficult due to the poor and sluggish kinetics observed for the electroreduction of CO_2.[154–156] However, the subsequent reduction steps occur almost instantaneously.[157] Therefore, the stabilization of the high-energy intermediate is crucial for achieving a high rate and energy-efficient CO_2 reduction process.[157] In electrocatalytic CO_2 reduction reactions, the product selectivity and efficiency are the most important factors.[157] Metal catalysts art classified into different groups according to their product selectivity,[158] such as Sn for producing formate, Cu for producing hydrocarbons and alcohols, and Au, Ag, and Zn for generating CO.[159,160]

Compared to other metals investigated for CO_2RR, zinc is relatively lower in cost and can stabilize radicals for both CO_2RR and HER.[161–164] It is also more abundant and cheaper than Au and Ag,[165,166] making its deployment for industrial-scale CO_2 electrolysis more economically viable.[167] However, planar Zn electrodes have low selectivity toward CO.[167] This can be improved by using Zn nanostructures, such as nanowires,[168]

dendrites,[169] nanosheets,[170–172] nanoplates,[173] and porous structures.[174,175] Zn-based catalysts, including dendritic Zn, porous Zn catalysts, Zn foam, and hexagonal Zn catalysts, have been demonstrated to effectively convert CO_2 into CO with an over 80% faradaic efficiency (FECO).[158]

However, when it comes to Zn-MOFs in the CO_2RR, researchers found that the Zn center in ZIF-8 was not reduced to metallic Zn.[176] Additionally, MOFs with different ligands showed varying electrocatalytic activities, suggesting that the ligands may act as the active sites for CO_2RR in ZIFs.[127] Ligands can also enhance electrocatalytic performance by creating unsaturated metal sites and improving charge transfer.[127] For example, Dou et al. (2019) increased the activity of MOFs for CO_2RR by doping them with the strong electron-donating molecule 1,10-phenanthroline.[138] Experimental and theoretical results showed that the electron-donating nature of phenanthroline facilitates charge transfer and induces adjacent active sites at the sp^2-C atoms in the imidazole ligand, which possesses more electrons, leading to improved activity and FE towards CO production.[126] Thus, when utilizing ZIFs for the CO_2RR, the focus should be placed on the ligands as the active sites.

In general, MOFs have poor stability in aqueous environments, which limits their potential applications in areas such as catalysis and sensing. However, some ZIFs have been found to have relatively good aqueous stability compared to other MOFs, such as MOF-74, [146,148–150] and UiO-66. [147] For example, ZIF-8 (composed of zinc ions and 2-methylimidazole ligands) has been shown to be stable in water at pH values up to 7.5 for several hours without significant degradation.[177] Other ZIFs, such as ZIF-67 (composed of cobalt ions and 2-methylimidazole ligands), have also been found to be relatively stable

in water.[178] Compared to other types of MOFs, ZIFs generally have higher stability in aqueous environments due to the strong coordination bonds between the metal ions and ligands.

1.4) Objectives

This thesis consists of two sections: MOFs for CO_2 capture; and MOFs for CO_2 reduction reaction.

The goal of the first part of the research is to design a Metal-Organic Framework adsorbent material to for the direct air capture of CO_2. The MOF should be able to efficiently capture CO_2 at ambient pressure conditions, while having hydrolytic stability and overall structural stability.

To accomplish this, it will be necessary to:

- Study the system using Molecular Dynamics.
- Investigate the effects of temperature change on the system under ambient pressure conditions.
- Study the result of dehydrating the system by removing water molecules.
- Understand the stability and performance of the system towards CO_2 capture by the addition of template molecules.
- Explore the CO_2 capture ability and test the overall performance of the system.

The goal of the second part is to identify a Zinc-based Metal-Organic Framework which can act as a bifunctional catalyst for the capture and reduction of CO_2 to form CO, as a precursor for syngas.

To accomplish this, it will be necessary to:

- Screen the Computation-Ready Experimental Metal-Organic Framework (CoRE MOF) database to identify MOFs that are zinc-based, and water stable.
- Study the two-electron CO_2 Reduction Reaction on the ligands and identify the most active sites using Density Functional Theory calculations.
- Evaluate the reasons behind activity of different active sites by identifying the HOMO and LUMO orbitals.

1.5) Expected Outcomes

Based on the objectives set out for the thesis, the system in the first part of the project is expected to have the ensuing capabilities:

- The system should be stable under varying temperature conditions, particularly at ambient conditions.
- It should also be stable in the presence/absence of water and should not become amorphous.
- The addition of template molecules is expected to improve both the stability and affinity towards CO_2.
- The system should be able to successfully capture CO_2.

Based on the objectives set out for the thesis, the systems identified in the second part of the project is expected to have the ensuing capabilities:

- The systems should be water stable and can capture CO_2.
- The systems should be able to successfully reduce CO_2 to CO.

1.6) Report Structure

Chapter 1 commences with the introduction of the thesis, wherein the background and motivations are explained, followed by a concise summary of the deficiencies of the current state-of-the-art. Lastly, the objectives and expected outcomes of the thesis are articulated.

Moving onto Chapter 2, it commences with an overview of the programs employed in this research, namely Molecular Dynamics simulations and Density Functional Theory. The chapter provides a brief exposition of the functioning of these technologies. Subsequently, a comprehensive account of the methods utilized in both research projects is delineated, encompassing the preparation and identification of structures and the type of investigations conducted.

Chapter 3 is exclusively focused on the systems employed for scrutinizing the direct air capture of CO_2. In this chapter, we investigated the impact of temperature, dehydrated and template molecules, before ultimately examining the ability of the systems to capture CO_2.

Chapter 4 delves into the utilization of zinc-based MOFs for the two-electron CO_2 reduction reaction. The MOFs identified via a screening of a database were studied for the production of CO. The activity of the identified active sites was confirmed by scrutinizing the HOMO/LUMO and charge density of each system.

Chapter 5 concludes the thesis by initially presenting the objectives and determining whether they were achieved or not, followed by suggestions for future research, ending with a final appreciation over the whole thesis.

2 Methodology

In this chapter, an overview of the methodologies utilized were discussed, with an introduction to Molecular Dynamics (2.1), followed by the computational details used for studying CO_2 capture (2.2). Then an introduction to Density Functional Theory (2.3) will be discussed before introducing the computational methods used to study the CO_2 reduction (0.

2.1) Introduction into Molecular Dynamics[179]

Molecular Dynamics (MD) is a computational technique used to study the behavior of molecules and molecular systems over time. It is based on the laws of classical mechanics and involves the simulation of the motions and interactions of atoms and molecules in a given system. The goal of MD simulations is to understand the properties and behavior of the system under study, such as its thermodynamic properties, kinetics, and structure.

MD simulations involve the numerical integration of the equations of motion for a set of particles in a system. To perform these simulations, a force field is used to describe the interactions between the particles. The force field consists of mathematical functions that describe the energy and forces between pairs of atoms or molecules. These functions are typically parameterized based on experimental data or quantum chemical calculations.

Parameterizing the force field is an essential step in MD simulations because it determines the accuracy and reliability of the simulation results. The force field describes

the interactions between atoms or molecules, and it is based on a set of mathematical functions that relate the potential energy of the system to the atomic or molecular coordinates. The parameters of the force field, such as bond lengths, bond angles, torsion angles, and van der Waals and electrostatic interaction parameters, are obtained by fitting the force field to experimental data or ab initio calculations.

It is important to parameterize the force field because the accuracy of the simulation results depends on the quality of the force field parameters. A poorly parameterized force field can lead to unrealistic or incorrect simulation results, which can affect the interpretation of the results and the validity of the conclusions drawn from the simulation. On the other hand, a well-parameterized force field can provide accurate and reliable predictions of the behavior of complex materials, which can help to guide experimental research and design new materials with desired properties.

In addition, the parameters of the force field can affect the efficiency of the simulation, as they determine the computational cost of the simulation. The number of parameters and the complexity of the mathematical functions used in the force field can affect the speed and accuracy of the simulation. Therefore, it is important to choose a force field that balances accuracy and computational efficiency, depending on the specific research question and the available computational resources.

The equations of motion for a particle in a molecular dynamics' simulation can be written as:

$$m_i \vec{r}_i = -\frac{\partial U_{pot}}{\partial \vec{r}_i} = \overrightarrow{f_i} \qquad [1]$$

where m_i is the mass of the ith particle, and $\vec{f_i}$ the force acting on it, which we assume to be entirely due to interactions with other particles. These equations can be integrated numerically using algorithms such as the Verlet algorithm or the leapfrog algorithm to obtain the positions and velocities of the particles at each time step. The Verlet algorithm uses the positions and velocities of particles at different time points to calculate their accelerations and update their positions. The leapfrog algorithm, on the other hand, updates the positions and velocities of particles at different time points based on their previous values.

The forces acting on each particle in the system are calculated using the force field. The force on each particle is calculated by taking the negative gradient of the potential energy with respect to its position:

$$\vec{F_i} = -\nabla U \qquad [2]$$

where U is the potential energy of the system, which depends on the positions of all particles in the system.

Furthermore, the potential energy function describes the energy associated with the interactions between particles in the material. The Lennard-Jones potential energy function is a commonly used example in MD simulations. It describes the interaction between two particles as a combination of a repulsive term (proportional to r^{12}, where r is the distance between the particles) and an attractive term (proportional to r^6).

To simulate bulk systems, periodic boundary conditions are often used. These conditions mimic an infinite system by replicating the simulation cell in all directions. The positions of particles are then wrapped back into the simulation cell at each time step.

The distance between two particles in the simulation cell can be calculated using the minimum image convention.

In addition to these fundamental concepts, another important technique is equilibration which involves running the simulation for a period of time to allow the system to reach a steady state. This ensures that the initial configuration of the material does not significantly impact the simulation results. The initial positions and velocities of particles can be generated randomly or from experimental data. To minimize the potential energy of the system, an energy minimization algorithm can be used to iteratively adjust the positions of the particles until the forces on each particle are minimized.

The equations used in MD simulations depend on the specific force field and algorithm used, but, in general, the key parameters that are included in the equations are:

1. Potential energy function: The potential energy function describes the interactions between atoms or molecules in a system. It includes terms for bond stretching, bond bending, torsion, van der Waals interactions, and electrostatic interactions.

2. Newton's equations of motion: These equations describe how the position, velocity, and acceleration of each atom or molecule in the system change over time. The equations include terms for the forces acting on each atom, which are derived from the potential energy function.

3. Time step: The time step is the interval between successive updates of the positions and velocities of the atoms or molecules. It is typically on the order of femtoseconds or picoseconds.

4. Temperature: The temperature of the system affects the kinetic energy of the atoms or molecules and is usually controlled by a thermostat.

5. Boundary conditions: The boundary conditions describe how the system interacts with its surroundings. The most common boundary conditions in MD simulations are: periodic boundary conditions, where the system is replicated in all directions to create an infinite lattice; and a box with fixed boundaries, where the atoms or molecules are constrained to stay within the box.

6. Initial conditions: The initial conditions specify the positions, velocities, and possibly other properties of the atoms or molecules at the beginning of the simulation.

2.2) Theoretical Methods and Computational Details for CO_2 Capture

In this section we will go over all techniques utilized in studying the CO_2 capture in the HCALF-50 and CALF-50 systems. This includes the forcefield parameterization (2.2.1), Molecular Dynamics details (2.2.2), how we studied changing the temperature (2.2.3), dehydration (2.2.4), insertion of xylene template molecules (2.2.5), and how we studied CO_2 capture (2.2.6).

2.2.1) Forcefield Parameterization

Figure 1 illustrates that HCALF-50 consists of two components forming a crystal structure. Firstly, there is the hexaaquachromium (III) (HAC) cationic cluster, which is a

metallic node surrounded by water molecules arranged in an octahedral shape (Figure 1c). Secondly, there is the aryl-phosphonate-based H_6L_1 ligand that serves as a linker (Figure 1d). To prepare the forcefield of HCALF-50, the forcefields of the ligands were first parameterized separately, based on parameters that were optimized and published previously, as noted below.

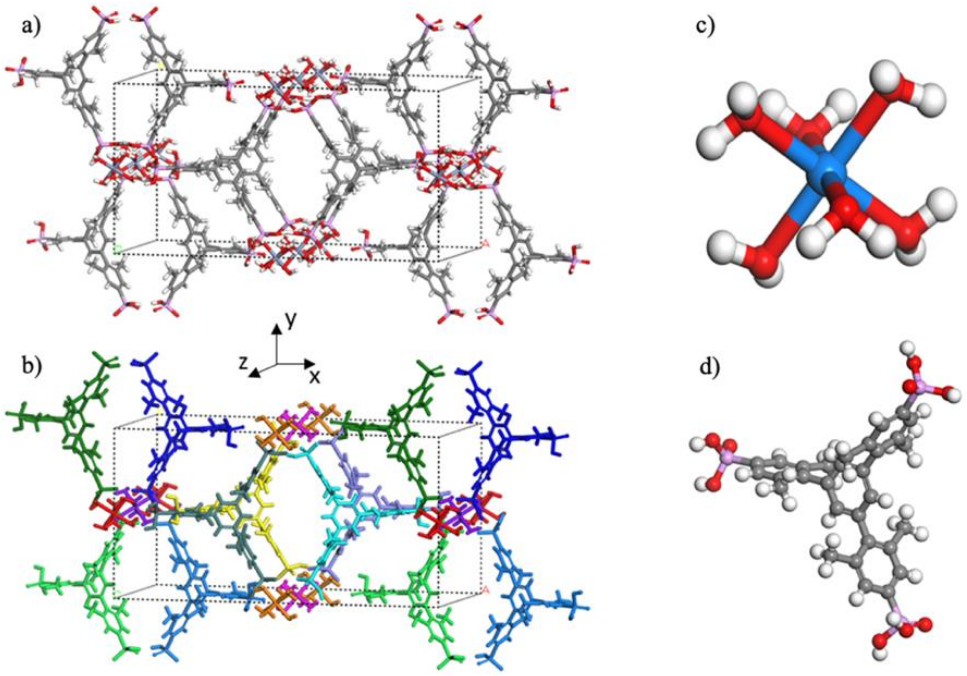

Figure 10: a) HCALF-50 crystal structure (unit cell shown with dotted line). b) Ligands with same color are periodic images. Molecular structures of c) HAC and d) H_6L_1 ligands. Color code: H – white, O – red, C – grey, P – pink and Cr – blue.

To model the HAC cluster, we utilized atomic partial charges that were reported by Martinez et al (1998 and 1999).[180,181] They employed DFT calculations to determine the geometry and charge distribution, factoring in vibration frequencies to calculate the thermal correction and zero-point energy using a statistical mechanical approach. It should be noted that this forcefield was optimized for HAC in a water solvent, which differs

from the chemical environment of the solid-state HCALF-50. Nonetheless, the six water molecules surrounding the Cr^{3+} cation are strongly bound to it via ionic Cr^{3+}–O^{2-} bonds, forming a rigid first hydration shell.[180–187] The Lennard-Jones (LJ) parameters for repulsion-dispersion interactions between Cr and O atoms were obtained from Salles et al. (2008), who modeled the complex structural changes of MIL-53 caused by CO_2 adsorption in the Cr-containing MOF at finite temperatures.[188,189] The non-bonded parameters for the HAC cluster and H_6L_1 ligand are presented in Appendix A.

To generate the forcefield for the H_6L_1 ligand, we employed the parameters reported for hexakis(p-phosphonatophenyl)benzene by Wehmeyer et al. (2013).[190] For the dimethylphenyl groups, the parameters were obtained from Qi et al. (2019).[191] Additionally, we calculated the atomic partial charges of the H_6L_1 ligand at the quantum chemical level, using B3LYP/6-311++G(d,p)/, which is implemented in the Gaussian16 software package.[192] Lastly, the parameters for xylene molecules were obtained from the OPLSAA forcefield. [193,194] The size of the boxes used for both HCALF and CALF-50 were 6.79 x 3.45 x 3.34 nm.

The validity of the forcefield employed in this study with regards to replicating the mechanical characteristics of HCALF-50, as well as accurately representing the interactions involving phosphonate and HAC clusters or chromium ions, remains unverified. To effectively authenticate the forcefield, experimental data would be required. Nonetheless, the forcefield utilized for HAC, hexakis(p-phosphonatophenyl)benzene, and dimethylphenyl groups was based on previously published literature,[180–191] along with the OPLSAA forcefield.[193,194] Consequently, the system can offer qualitative insights into the effects of dehydration and templating, as the interactions involving water, carbon dioxide,

xylene, and the aryl rings or methyl groups of the systems were elucidated using the OPLSAA forcefield. Despite the existence of inaccuracies in the forcefield employed in this study, the research objective was not to achieve exact replication of results, but rather to examine trends associated with system dehydration, temperature variations, exploration of template molecules, and investigation of the systems' capacity for CO_2 capture. For these purposes, the forcefield utilized can be considered valid.

2.2.2) Molecular Mechanics/Dynamics (MM/MD) Computational Details

To simulate all the systems, we first performed a geometry optimization using the quasi-Newtonian Broyden-Fletcher-Goldfarb-Shanno (BFGS) algorithm,[195] with a force threshold of 10 kJ/mol•nm. The BFGS was used to find the minimum energy of the bonding and positioning of the atoms in the systems. Following this, we conducted equilibration using the velocity rescaling thermostat and Berendsen barostat,[196] for 1 ns, in a constant number of particles N, pressure P, and temperature T (NPT) ensemble, with temperature and pressure coupling constants of 0.1 ps and 2 ps, respectively, and a reference pressure of 1 bar. The system was then equilibrated for an additional 1 ns in a constant number of particles N, volume V, and temperature T (NVT) ensemble, using the Nosé-Hoover thermostat. Finally, the structures were allowed to reach equilibrium for 100-200 ns in an NPT ensemble, using Parrinello-Rahman pressure coupling.[197,198]

Throughout all MD simulations, we used the leap-frog algorithm to integrate Newton's equations of motion,[199] with a 1-fs time step and applying linear center of mass motion (COMM) removal, and the Verlet cutoff scheme.[200] No constraints were used for the bonds with hydrogens. The particle-mesh Ewald summation method was employed

to handle the long-range electrostatic and van der Waals (vdW) interactions.[201] The pressure was constrained to 1 atm for the project.

2.2.3) Changing Temperature

To investigate the impact of temperature on HCALF-50 and CALF-50, we conducted molecular dynamics simulations on a 2×2×2 supercell for each unit cell (refer to Figure 2a and b). The temperature was varied between 0 K and 750 K, with increments of 50 K, to obtain a comprehensive understanding of the temperature effect. Subsequently, we explored the impact of annealing on both systems, varying from 0 K to 450 K. Finally, we analyzed the influence of temperature on the volume of the systems.

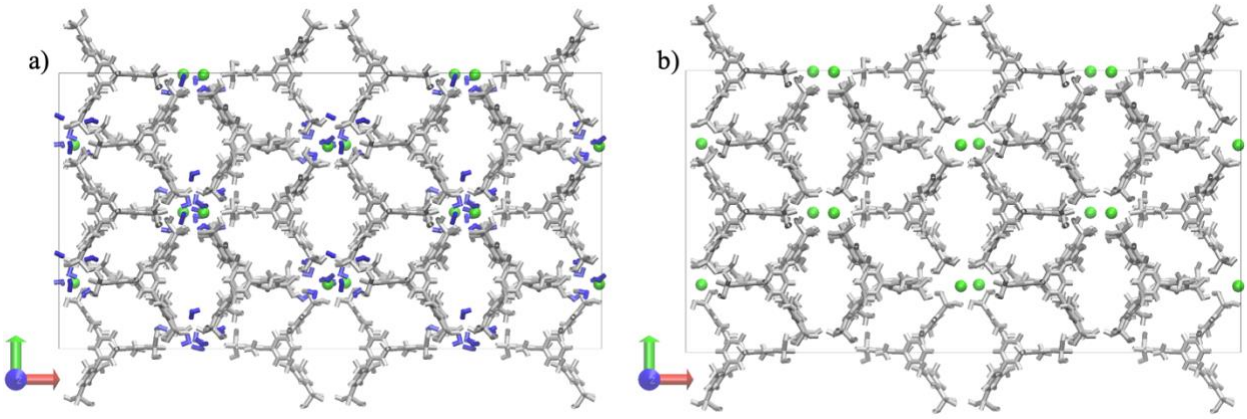

Figure 11: Initial structures of a) HCALF-50 and b) CALF-50. Color code: H_2O – blue, Cr - green, H_6L_1 - grey.

2.2.4) Dehydration

To simulate the dehydration of HCALF-50 to CALF-50, we used an approach similar to that proposed by Larsen et al. (2017).[202] More specifically, we modelled the dehydration process of HCALF-50 by performing MD simulations on a 2×2×2 supercell

from the HCALF-50 unit cell (Figure 11a). In this supercell, there are 64 H_6L_1 ligands, 32 Cr ions and 192 H_2O molecules. To model the slow dehydration, we prepared intermediate structures (states) where H_2O molecules were randomly removed in increments of 24, from the fully hydrated MOF (HCALF-50) until the complete removal of H_2O (i.e., CALF-50) was achieved (Figure 11b). The temperature was set to 425 K to be consistent with the experimental conditions at which the dehydration was performed.

2.2.5) Xylene Template Insertion

To investigate the influence of template molecules on the structural stability of MOFs, we conducted molecular dynamics simulations in the 2×2×2 supercells of both HCALF-50 and CALF-50. Specifically, 150 xylene molecules were added into the pores of both systems using Packmol.[203] All constitutional isomers of xylene molecules (i.e., meta, ortho, and para isomers, referred to as m-xylene, o-xylene, and p-xylene, respectively) were modelled at a temperature of 425 K.

2.2.6) CO_2 Capture

To ascertain the potential suitability of the HCALF-50 and CALF-50 systems for effective CO_2 capture, a single CO_2 molecule was introduced into 2×2×2 supercells of both systems via Packmol.[203] Subsequently, molecular dynamics simulations were conducted to investigate the behaviour of the aforementioned systems. The temperature parameter was established at 425 K, in accordance with the experimental conditions under which the dehydration was executed.

2.3) Introduction into Density Functional Theory [204]

Another technique utilized in computational chemistry is Density Functional Theory (DFT), which is a computational method used to calculate the electronic structure of atoms, molecules, and solids. DFT is based on the principle that the total energy of a system can be expressed as a functional of the electron density, rather than the wave function of the system. The electron density is a probability density that describes the distribution of electrons in the system.

The fundamental equation in DFT is the Kohn-Sham equation, which is a set of coupled partial differential equations that describe the electronic structure of a system. The Kohn-Sham equation is derived from the Hohenberg-Kohn theorem, which states that the electron density uniquely determines the external potential energy of a system.

The Kohn-Sham equation is given by:

$$\left[\frac{h^2}{2m}\nabla^2 + V(\boldsymbol{r}) + V_H(\boldsymbol{r}) + V_{XC}(\boldsymbol{r})\right]\psi_i(\boldsymbol{r}) = \varepsilon_i\psi_i(\boldsymbol{r}) \qquad [3]$$

where h is Planck's constant, m is the mass of the electron, ∇^2 is the Laplace operator, $V(\boldsymbol{r})$ is the external potential that an electron experiences in a given system, $V_H(\boldsymbol{r})$ is the Hartree potential, $V_{XC}(\boldsymbol{r})$ is the exchange-correlation potential, $\psi_i(\boldsymbol{r})$ is the wave function of the ith electron in the system and ε_i is the energy of the ith electron in the system.

The exchange-correlation potential energy is usually calculated using density functional approximations. These approximations are derived from the exact exchange-correlation functional, which is unknown. The most used density functional

approximations are the local density approximation (LDA) and the generalized gradient approximation (GGA).

The LDA assumes that the exchange-correlation potential energy is a function of the electron density at each point in space.[204] The GGA includes additional terms that depend on the gradient of the electron density, which allows for a more accurate description of the electronic structure.[204]

DFT calculations typically involve the following steps:

1. Input geometry: The structure of the system is defined by specifying the positions of the atoms.
2. Calculation of electron density: The Kohn-Sham equation is solved self-consistently to obtain the electron density of the system.
3. Calculation of total energy: The total energy of the system is calculated from the electron density using the density functional approximation.
4. Optimization: The geometry of the system is optimized by minimizing the total energy with respect to the atomic positions.
5. Analysis: The results of the calculation are analyzed to obtain information about the electronic structure and other properties of the system.

While Density Functional Theory (DFT) offers notable advantages in terms of efficiency, versatility, and applicability, it is imperative to acknowledge its inherent

limitations. The reliance on approximations, intricately linked to the choice of functionals, underscores the necessity of discerning the appropriate functionals to ensure reliable results. Furthermore, the computational demands associated with DFT, particularly concerning system size, emphasize the significance of striking a balance between system complexity and computational cost. Adhering to these considerations enables us to harness the capabilities of DFT to address our specific research requirements.

2.4) Theoretical Methods and Computational Details for CO_2RR

In this section, we will discuss how we determined the adsorption energies (2.4.1), and how we studied the HOMO/LUMO and charge density for each system (2.4.2).

2.4.1) Density Functional Theory Computational Details

All systems under investigation were obtained from the Cambridge Crystallographic Data Centre.[205] The unit cells of these systems were generated using the Gaussian16 software package.[192] All atoms, excluding the zinc, and the ligands under study, were constrained. Additionally, this software was employed to conduct both geometry optimizations with frequency and single point energy calculations. The optimization procedure facilitated the determination of the molecular configuration at the minimum energy level,[206] utilizing wb97xd def2svp. The frequency calculation was performed to determine the molecular vibrations.[206] Subsequent to the optimization and frequency calculations, the single point energy was calculated to establish the energy and

wave function using wb97xd def2tzvp.[206] The temperature and pressure were constrained to 298.15 K and 1 atm, and the calculations were done in a vacuum.

2.4.2) HOMO/LUMO and Charge Density

The highest occupied molecular orbital (HOMO) and the lowest unoccupied molecular orbital (LUMO), as well as the charge density for all investigated systems were examined using Gaussian16 software.[192] This was accomplished by employing the formchk files obtained from the optimized clean structures.

3 CO_2 Capture on HCALF-50 and CALF-50

This chapter includes the analysis of HCALF-50 and CALF-50 for the direct air capture of CO_2. First the effect of temperature is discussed (3.1) where we show how temperature results in a decrease in pore volume. Next (3.2), we studied the effect of removing water molecules in increments of 24, where we found that the system collapsed to better stabilize the system in the absence of water. Afterwards, we studied the addition of xylene template molecules (3.3), which showed increased stability in both the HCALF-50 and CALF-50 systems by allowing the pores to remain open. Finally, we investigated the ability of both systems to capture CO_2 (3.4), and found that both systems are unsuited for this endeavor.

3.1) Changing Temperature

Given the emphasis of this project on direct air capture of CO_2, the calculations were performed at a constant pressure of 1 atm. Nevertheless, the temperature range for this process may vary, making it crucial to explore the impact of temperature on the HCALF- and CALF-50 systems. As depicted in Figure 12, elevating the temperature resulted in a reduction in volume for both systems.

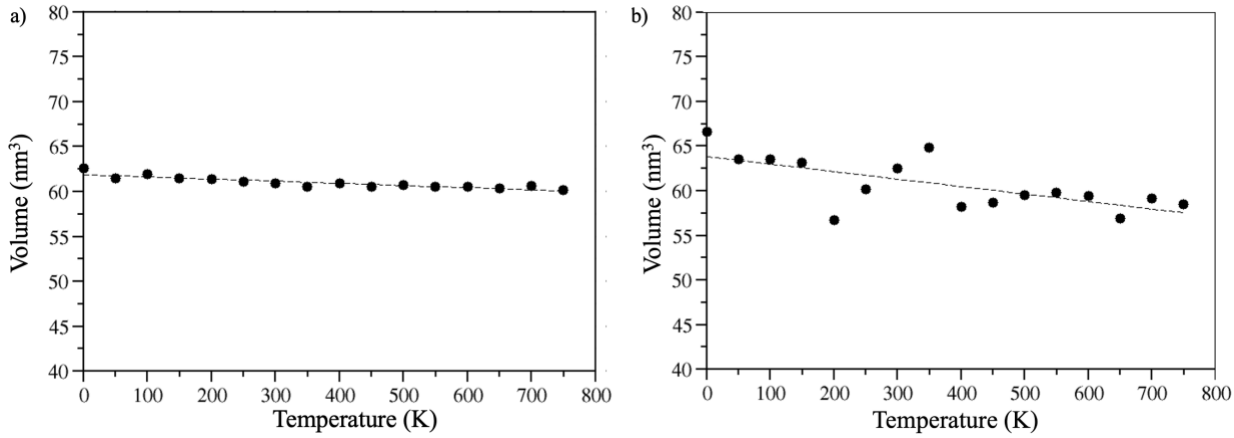

Figure 12: The impact of incremental temperature changes ranging from 0K to 750K on the volumes of a) HCALF-50 and b) CALF-50.

Our research aimed to investigate the underlying cause of the observed volume change in the CALF-50 system. To this end, we conducted a detailed analysis of the system, and our findings revealed the presence of a cluster of six ligands enveloping the H_6L_1-12 ligand, as depicted in Figure 13.

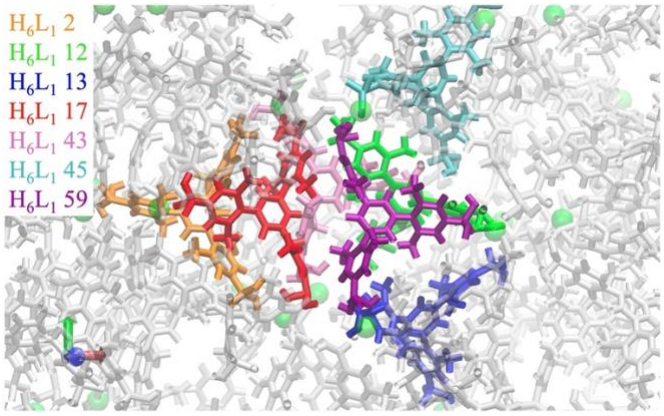

Figure 13: Identified clusters of H_6L_1 ligands, surrounding H_6L_1-12, on CALF-50. Colour code for each ligand is displayed on the legend.

Upon identification of the ligand cluster surrounding H_6L_1-12, we proceeded to measure the inter-ligand distances by using the center of mass, as illustrated in Figure 14. Our analysis revealed a marked increase in slope between ligands H_6L_1 12 and 17, as well as a substantial decrease in slope between H_6L_1 12 and 13. Based on these results, we opted to concentrate on these three ligands for the annealing of CALF-50.

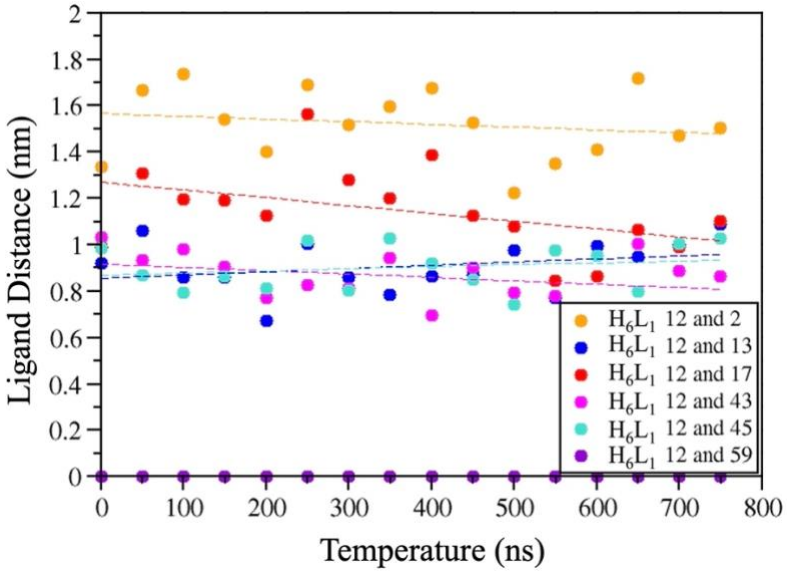

Figure 14: The change in ligand distance between H_6L_1-12 and surrounding ligands because of an incremental temperature change ranging from 0K to 750K on CALF-50.

In the course of the annealing procedure, the system was initially set at a temperature of 0 K, which was gradually raised to 150 K at 5 ns, and subsequently to 450 K at 15 ns, as illustrated in Figure 15. The notable alterations in ligand distance were attributed to the system's stabilization following the temperature change.

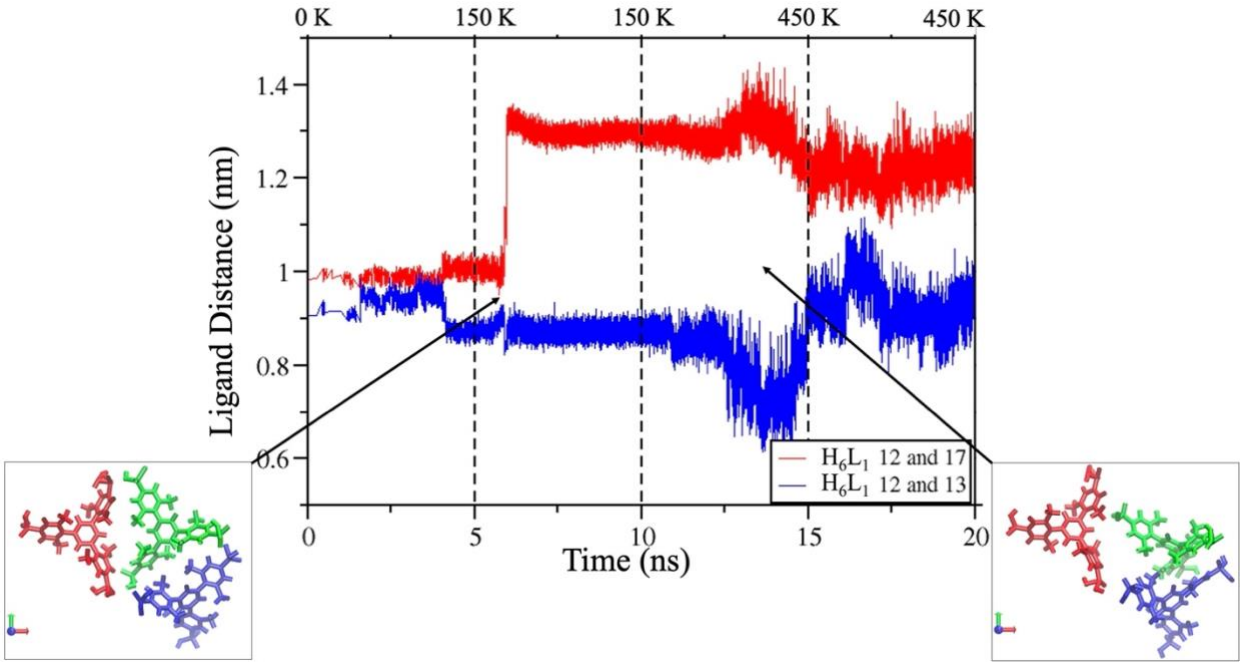

Figure 15: Annealing trajectory of CALF-50 over a duration of 20 ns, from 0K to 450 K, displaying the variation in distance between ligands surrounding H_6L_1-12. The shift in distance between H_6L_1 12 and 17 is shown in red, while the change in distance between H_6L_1 12 and 13 is shown in blue. Furthermore, the placement of these three ligands during two significant distance changes is also illustrated with colour code: H_6L_1 12 – green, H_6L_1 13 – blue, and H_6L_1 17 – red.

The equilibration of CALF-50 resulted in a structure with micropores that were relatively open. Specifically, the presence of methyl groups on the aryl arms resulted in the orthogonalization of the aryl groups concerning the central ring, thereby preventing the formation of π interactions between the aryl arms of neighboring H_6L_1 ligands. The H_6L_1 ligands were aligned parallel to each other, creating an open linear channel in the z-direction. However, the thermal agitation led to a slight distortion of the network, as can be seen in Figure 16. The aforementioned structural distortion led to a gradual reduction in the volume of the pores, ultimately causing a collapse of the MOF. This phenomenon was also observed during the dehydration process.

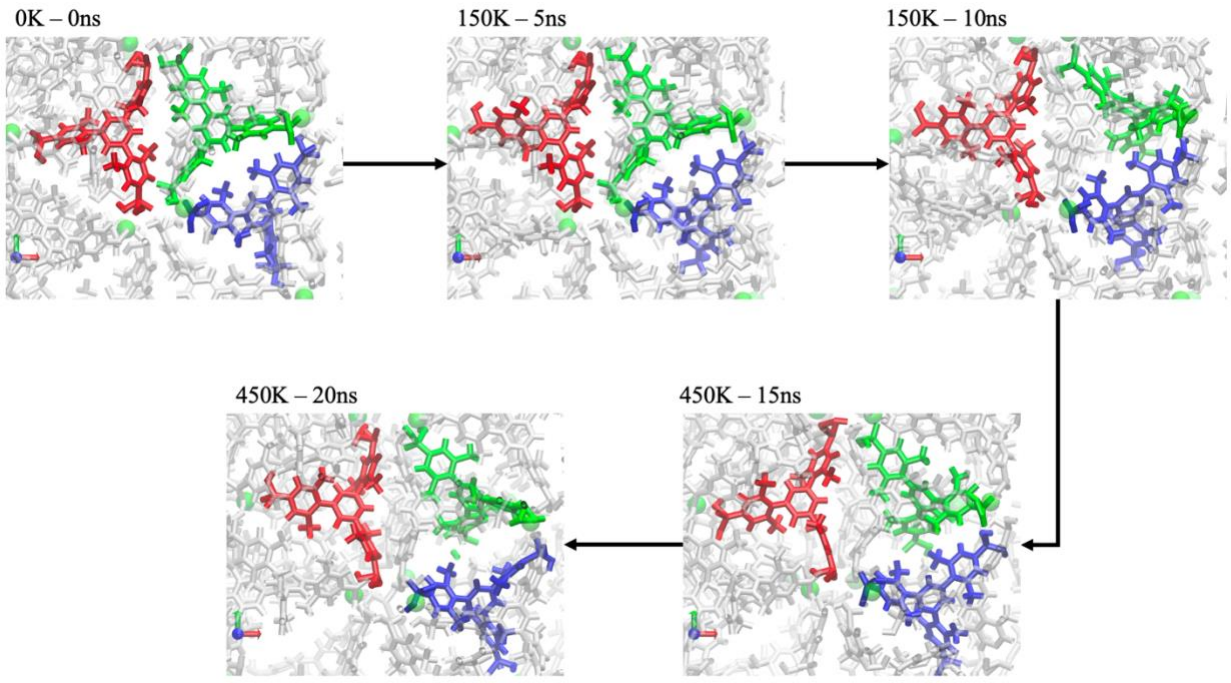

Figure 16: Positioning of the three ligands in 5 ns time intervals. Colour code: H_6L_1 12 – green, H_6L_1 13 – blue, and H_6L_1 17 – red.

3.2) Dehydration

Molecular dynamics simulations were employed again to model the phase transition of the HCALF-50 during the dehydration process of the network, as depicted in Figure 17.

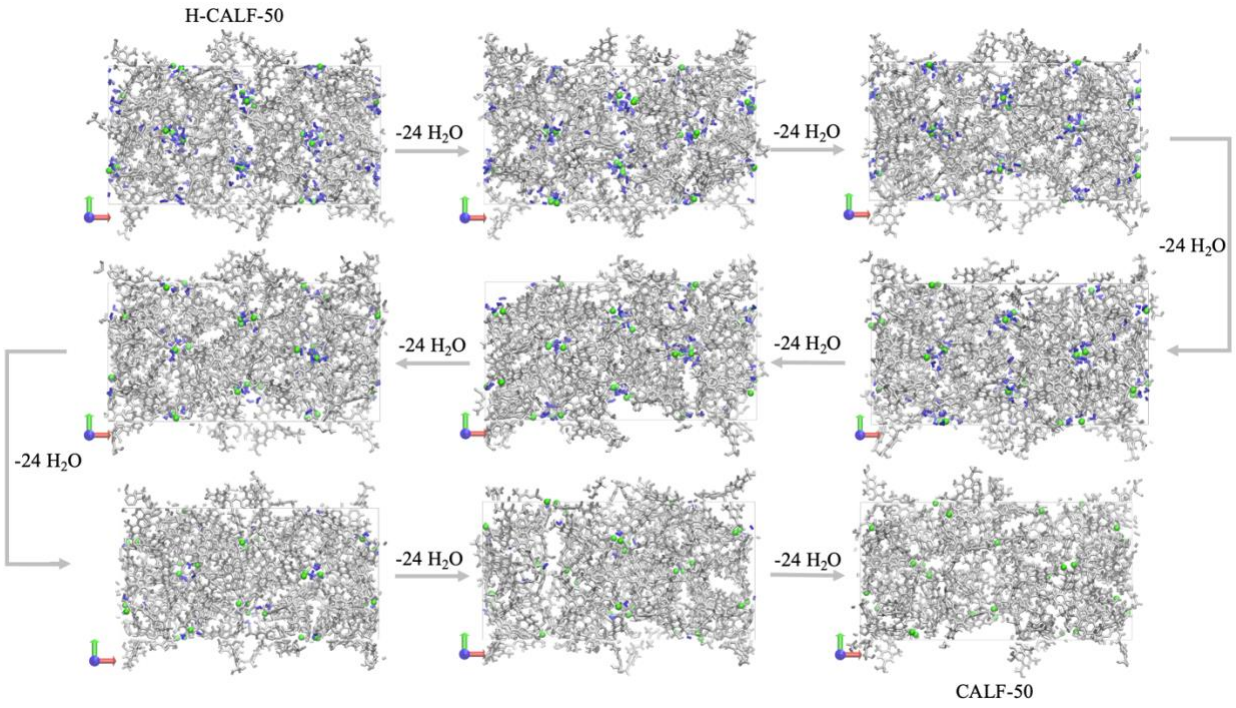

Figure 17: MD simulation of the slow dehydration of HCALF-50 to CALF-50 by consecutive removal of 24 water molecules. The arrows indicate the direction of the dehydration, and the box displays the 2×2×2 cell. Colour code: H_2O – blue, Cr - green, H_6L_1 - grey.

Upon removing the water molecules, we observed a progressive phase transition of the MOF, transforming from a crystalline structure to an amorphous structure. The loss of H-bonds that coordinate the phosphonate groups around the Cr^{3+} ion, which occurs in the absence of water molecules, affects the structural integrity of the network. This phenomenon was demonstrated by the intermediate states showing a gradual collapse of the pores, leading to the once crystalline structure becoming an amorphous CALF-50.

Our findings suggest that the phase transition is a result of the H_6L_1 ligands reorienting themselves to form π interactions and better stabilize the system in the absence of water (Figure 18).

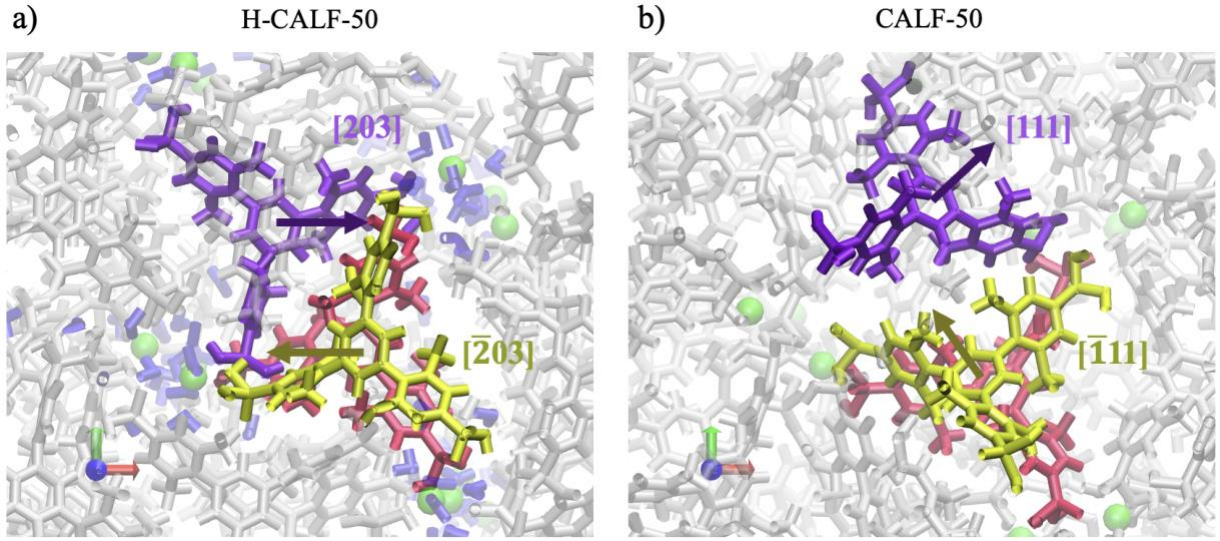

Figure 18: H_6L_1 ligand reorientation due to dehydration from a) HCALF-50 to b) CALF-50. Colour code: H_2O – blue, Cr - green, H_6L_1 – grey, 1- H_6L_1 – purple, 2- H_6L_1 – red, 3- H_6L_1 – yellow.

Specifically, the normal vectors of the planes formed by H_6L_1 ligands were initially oriented along the [203] and [$\bar{2}$03] directions. Upon dehydration, the ligands could reorient with normal vectors pointing along the [$\bar{1}$11] and [$\bar{1}$11] directions, as highlighted in Figure 18 with ligands in purple and yellow, respectively. This reorientation allowed the ligands to interdigitate, leading to the loss of pore volume (Figure 19). In comparison, the dehydration conducted on the HCALF-37 system by Lian and Siahrostami (2023) found that although there was a reordering of the systems, the system remained stable and the pores of the CALF-37 system were preserved.[207]

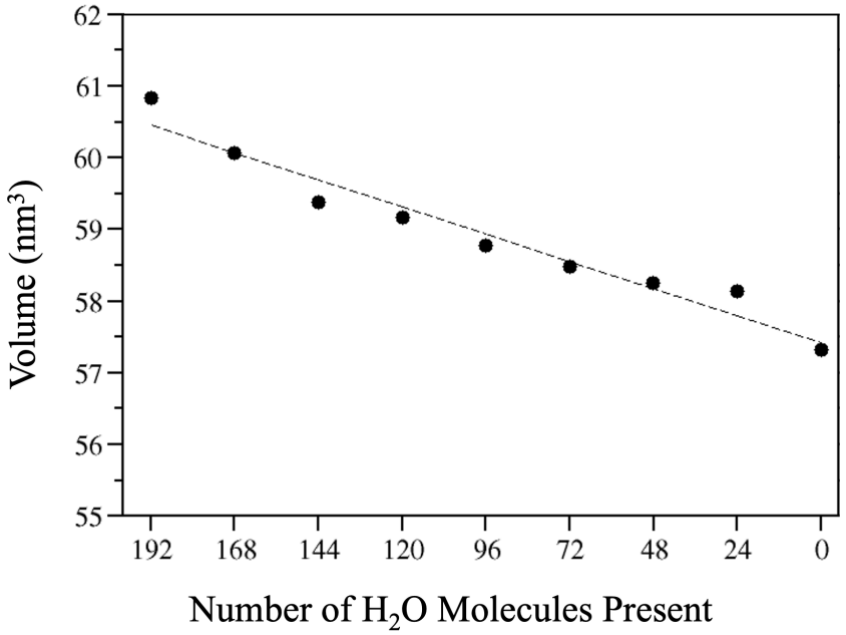

Figure 19: The change in volume following the reduction in the number of water molecules in the HCALF-50 to CALF-50 systems.

3.3) Xylene Template Insertion

To mitigate the amorphization and collapse of the porous network, 150 xylene template molecules were introduced into the individual pores of the 2×2×2 HCALF-50 and CALF-50, as depicted in Figure 20. Xylene was chosen as a suitable guest molecule due to its small size and aromaticity, which was suited for the pores created by the H_6L_1 ligands.

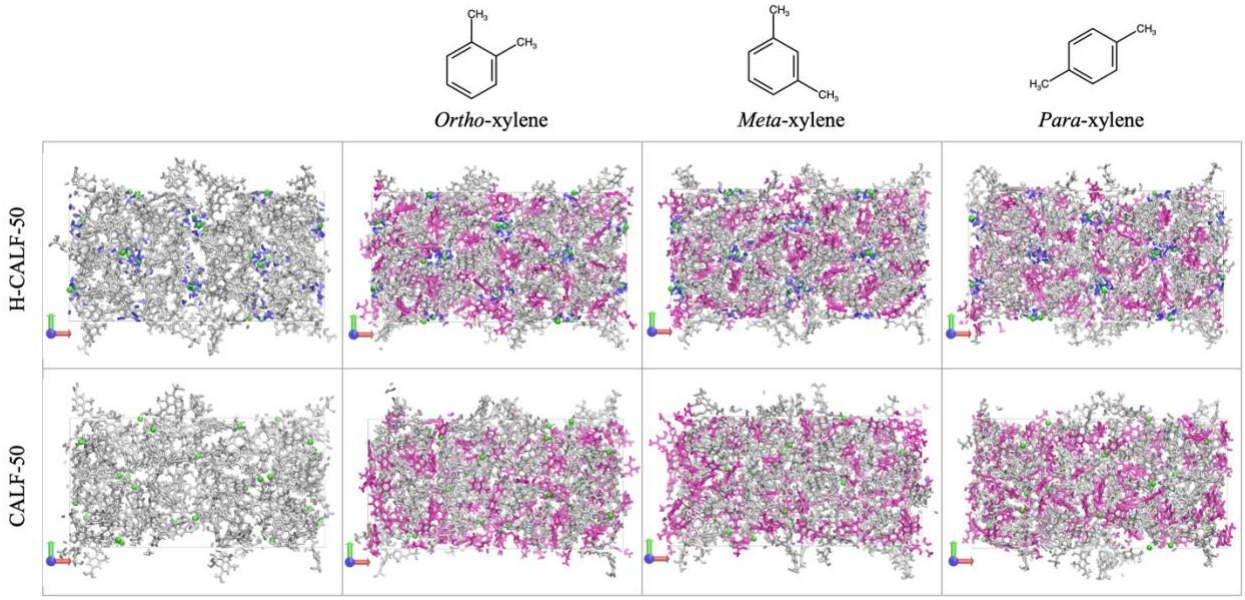

Figure 20: Insertion of *o*-xylene, *m*-xylene and *p*-xylene into HCALF-50 and CALF-50. Residues in grey, blue, and magenta showcase the H_6L_1 ligands, H_2O molecules and xylene template molecules, respectively. To contrast the effect of template molecules, HCALF-50 and CALF-50 without the presence of any template are also displayed.

Our investigation revealed that these template molecules form favorable interactions with the H_6L_1 ligands, which prevent the ligands from interacting with one another, thereby allowing the pores to remain open and preventing collapse. Specifically, we observed a CH-π interaction between the *o*-xylene molecules and the central aryl rings of H_6L_1. Additionally, we studied the interactions between the other xylene isomers and the HMOF/MOF, and found CH-CH interactions between the methyl groups of xylenes and H_6L_1, CH-π interactions between the methyl groups and aromatic rings, and π-π interactions between the aromatic rings of xylene and the central aryl ring of H_6L_1, as depicted in Figure 21. Notably, we observed that the porous network is most effectively preserved by inserting *p*-xylene into the frameworks, followed by *o*-xylene, while *m*-xylene only slightly mitigates the amorphization of the network upon dehydration.

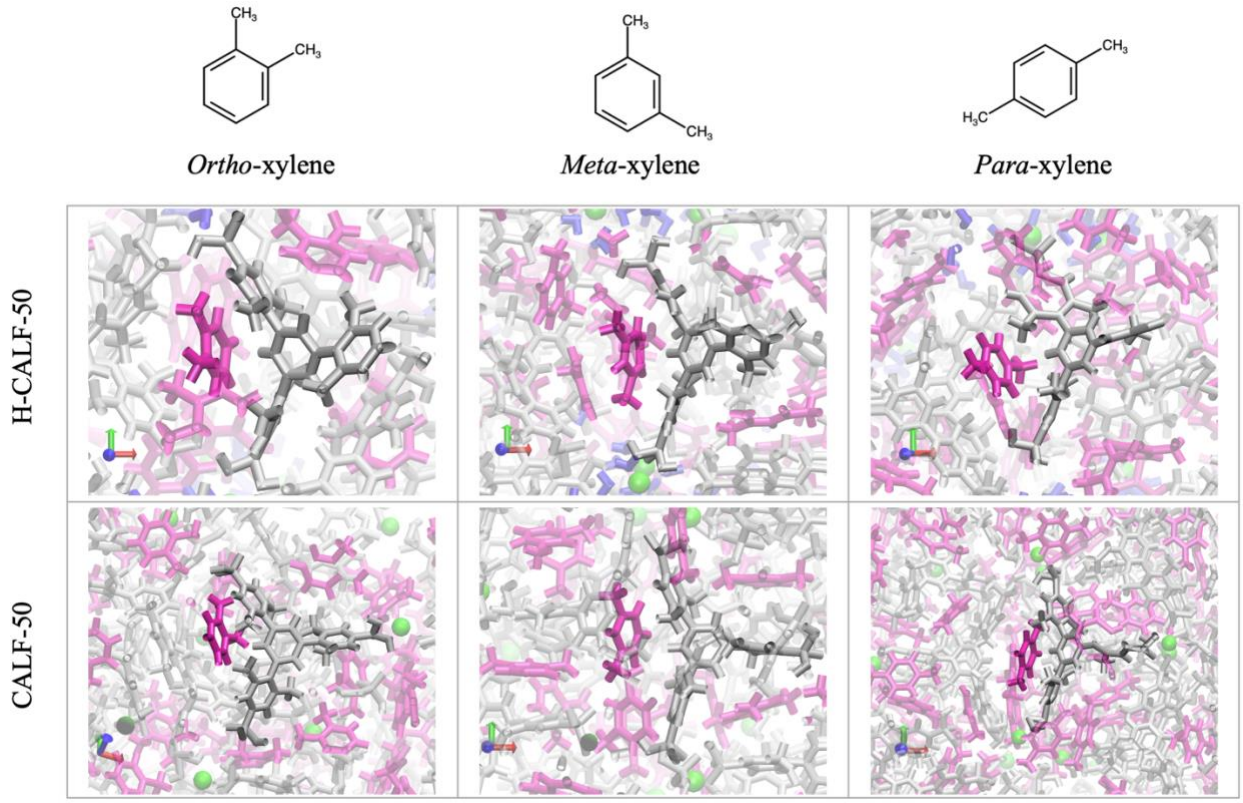

Figure 21: CH–π interactions between *o*-xylene, *m*-xylene and *p*-xylene and central aryl rings of H_6L_1 in HCALF-50 and CALF-50. Colour code: H2O – blue, Cr – green, H_6L_1 – grey, xylene – magenta.

3.4) CO_2 Capture

To assess the CO_2 adsorption capacity of HCALF-50 and CALF-50, a single molecule of carbon dioxide was inserted into 2×2×2 supercells. Additionally, we investigated the impact of template molecules on CO_2 capture by introducing the CO_2 molecule to HCALF-50 and CALF-50 systems containing *o*-xylene, *m*-xylene, and *p*-xylene molecules, as illustrated in Figure 22.

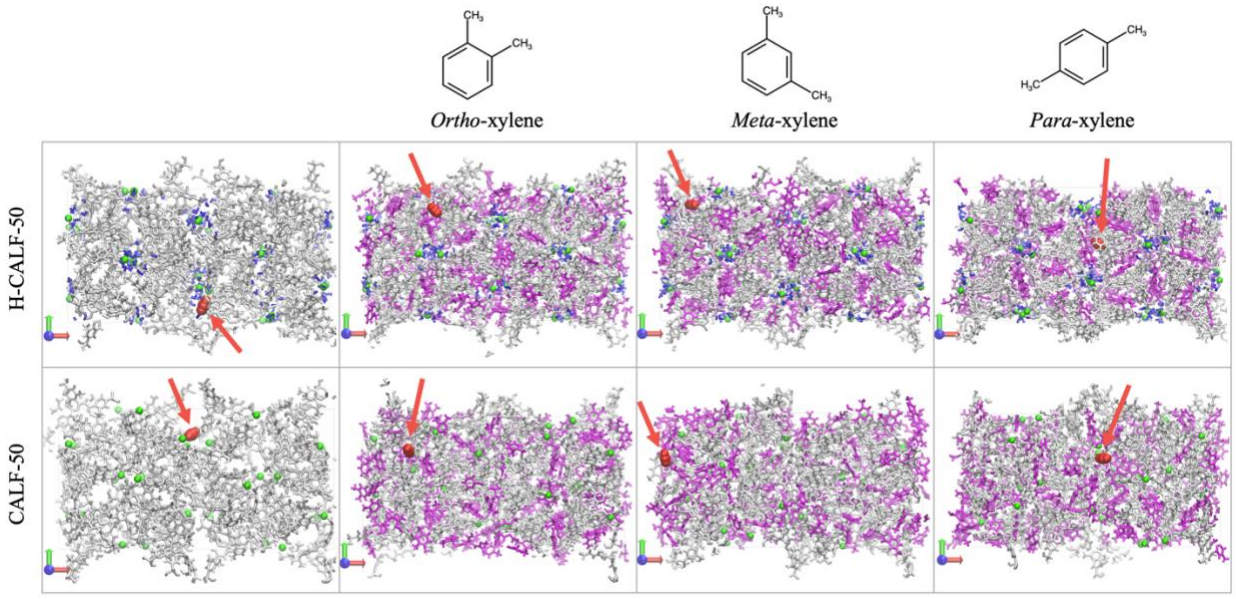

Figure 22: Insertion of CO_2 to HCALF-50 and CALF-50. Residues in grey, blue, and magenta showcase the H_6L_1 ligands, H_2O molecules and xylene template molecules, respectively. To contrast the effect of template molecules, HCALF-50 and CALF-50 without the presence of any template are also displayed.

Our findings reveal that CO_2 diffusion occurs rapidly in CALF-50 in the absence of template molecules. This assertion was substantiated through an examination of the spatial domains predominantly occupied by the CO_2 molecule, as visually depicted in Figure 23. It is evident that CO_2 does not persist within a singular pore, as the black regions exhibit a notable dispersion across the pores within each system.

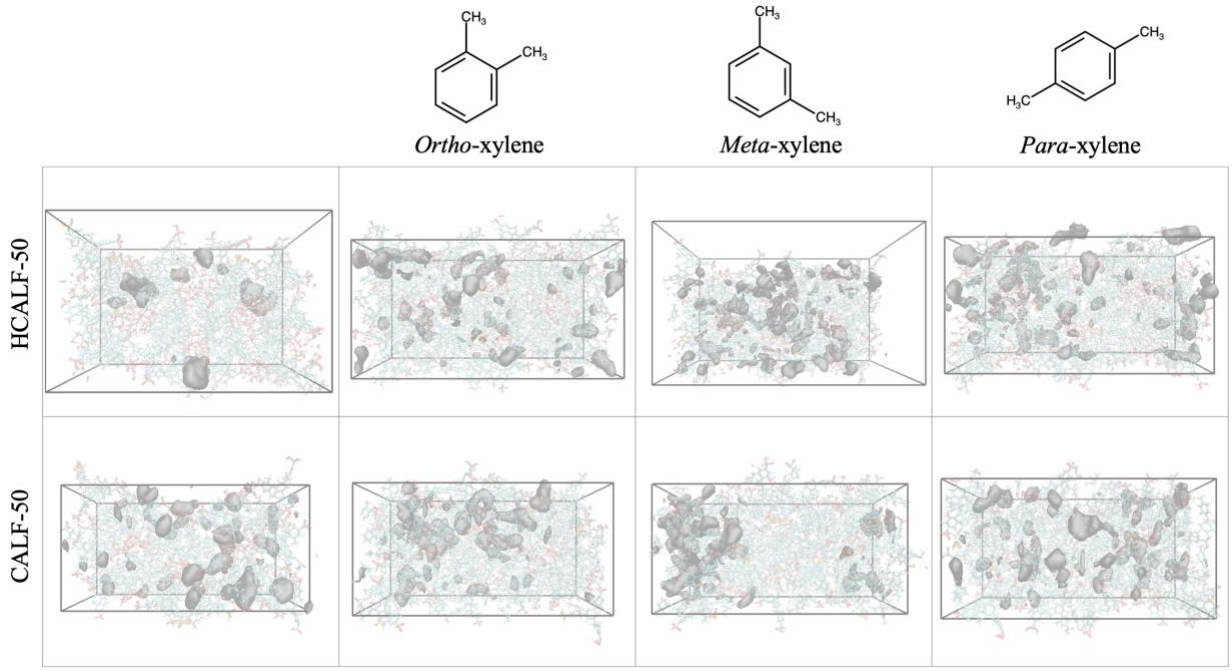

Figure 23: Spatial occupancy of the CO_2 molecule depicted by the areas denoted in black in the HCALF and CALF-50 systems, in the absence and presence of xylene.

We aimed to confirm this further by utilizing diffusion coefficients based on the distance travelled by the CO_2 molecule, as seen in Table 4.

Table 4: Diffusion coefficient (cm^2/s) of CO_2 in HCALF and CALF-50 in the absence and presence of xylene.

MOF	No Template $(1 \times 10^{-5}\ cm^2/s)$	Ortho-xylene $(1 \times 10^{-5}\ cm^2/s)$	Meta-xylene $(1 \times 10^{-5}\ cm^2/s)$	Para-xylene $(1 \times 10^{-5}\ cm^2/s)$
CALF-50	9.06 (±7.24)	0.31 (±0.28)	1.17 (±0.37)	0.15 (±0.14)
HCALF-50	1.32 (±0.16)	0.41 (±0.22)	0.84 (±0.31)	0.25 (±0.01)

The diffusion coefficients indicate that the CO_2 molecule diffused most rapidly in CALF-50 without template molecules, followed by HCALF-50 without template molecules.

The diffusion was the lowest in the systems with the *p*-xylene template molecule, followed by *o*-xylene and *m*-xylene.

We compared our findings to that of Lian and Siahrostami (2023) to confirm our results.[207] When a single CO_2 molecule was added into the HCALF and CALF-37, the authors reported diffusion coefficients as low as 10^{-10} cm^2/s and found that the CO_2 remained in a single pore for the duration of the dynamic.[207] This is opposite to our findings, which showed that the CO_2 was unable to remain in a single pore, and had diffusion coefficients in the range of 10^{-5} to 10^{-6} cm^2/s, which are significantly larger than literature. Thus, this confirms that although the presence of the template molecules increased the absorption of CO_2 in both HCALF- and CALF-50, this system was found to be unsuitable for the direct air capture of CO_2.

In conclusion, this study aimed to explore the impact of temperature and template molecules on the structure and CO_2 adsorption capacity of HCALF-50 and CALF-50. The findings reveal that elevating the temperature leads to a reduction in volume for both systems. The annealing procedure of CALF-50 resulted in micropores that were relatively open, but thermal agitation caused a gradual reduction in the volume of the pores, ultimately leading to the collapse of the MOF. However, the introduction of xylene template molecules prevented the collapse of the porous network by forming favorable interactions with the H_6L_1 ligands. The porous network is most effectively preserved by inserting *p*-xylene into the frameworks, followed by *o*-xylene, while *m*-xylene only slightly mitigates the amorphization of the network upon dehydration. The study also found that the diffusion of CO_2 occurs rapidly in CALF-50 in the absence of template molecules.

Finally, it was discovered that the slowest CO_2 diffusion occurred in the HCALF-50 and CALF-50 systems that contained *p*-xylene molecules.

4 CO_2RR on Zinc-Based MOFs

This chapter includes the screening process from the CoRE MOF Database (4.1) in order to identify suitable MOFs to further study the CO_2RR. After which, we will analyze the results of the DFT calculations on the active sites on each MOF (4.2), and end with the confirmation of the active sites by analyzing the HOMO/LUMO and charge density of each system (4.4).

4.1) CoRE MOF Database

To determine Metal-Organic Frameworks (MOFs) suitable for study in the CO_2 Reduction Reaction, two distinct MOF databases were utilized. The first database, comprised of 69,666 MOFs, was initially identified by Moghadam et al. (2017) through the use of the Cambridge Structural Database (CSD).[207] The second database, consisting of 14,000 3-dimensional MOFs, was identified by Chung et al. (2019).[208] These databases comprise of MOFs that have already been synthesized experimentally, and are able to be studied computationally. Upon compiling both collections, specific criteria were established to curate the MOFs, which included the following:

- A Pore Limiting Diameter (PLD) exceeding 10 Å, to ensure adequate size of the MOFs.
- Containment of a zinc metal center, to ensure a cost-efficient and more effective alternative to the state-of-the-art.
- Stability in water, as a result of MOFs generally exhibiting poor stability in water which limits their application in catalysis.

- Potential for CO_2 capture to identify a bifunctional catalyst for both CO_2 capture and reduction.

The workflow utilized can be seen in Figure 24.

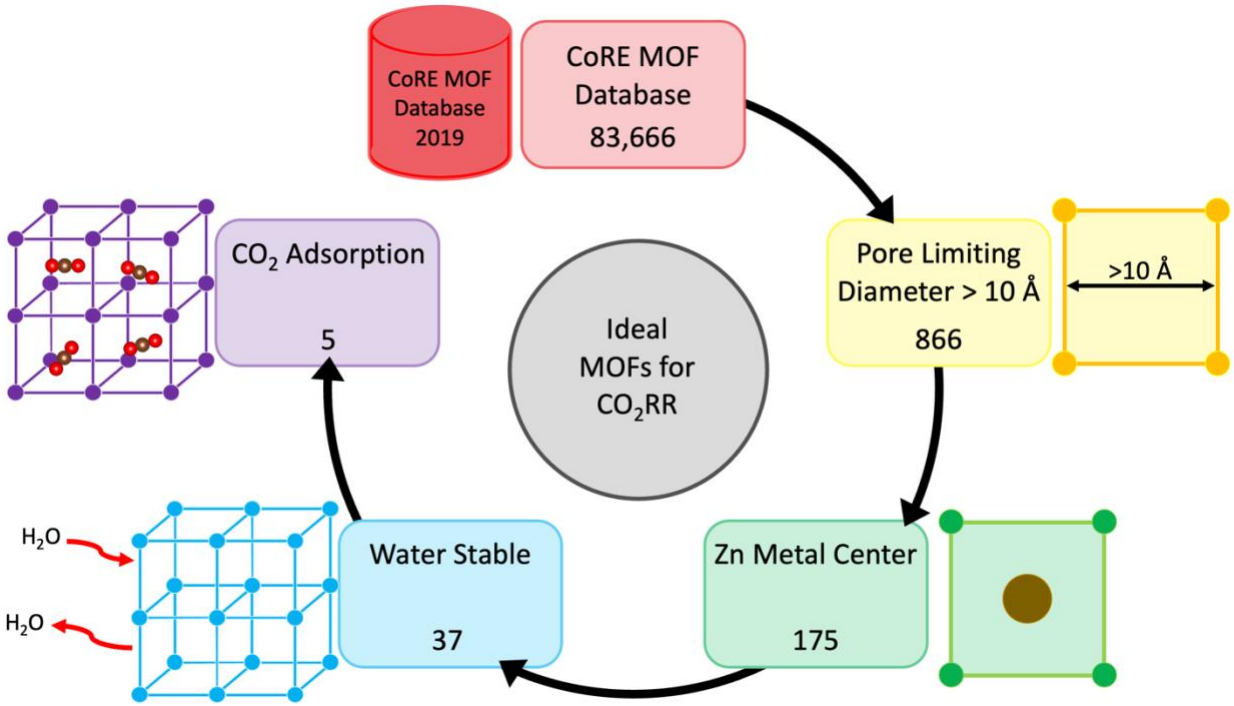

Figure 24: Identifying MOFs to study for the CO_2RR based on five different criteria. The numbers indicate the total number of MOFs that met each of the criteria.

The CoRE MOF Database facilitated the identification of two zeolitic imidazolate frameworks and three metal-organic frameworks that fulfilled the prescribed criteria above. The structures satisfying these criteria are depicted in Figure 25. This study identified five potential systems, including ZIF-70, ZIF-82, tp-PMBB-1-asc-1, MOF-74, and SNU-30.

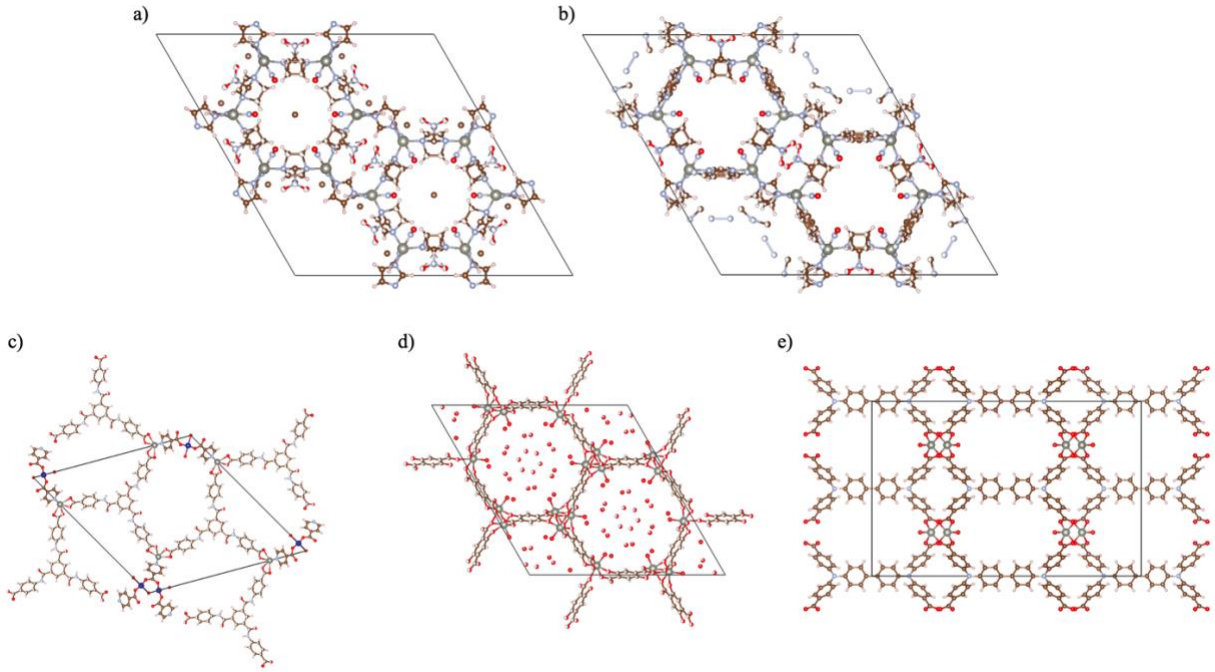

Figure 25: Molecular structures of several ZIFs and MOFs that meet the requisite criteria, namely, the presence of a zinc-metal center, a pore limiting diameter greater than 10 Å, water stability, and demonstrated capacity for CO_2 absorption. The depicted structures include a) ZIF-70, b) ZIF-82, c) tp-PMBB-1-asc-1, d) MOF-74, and e) SNU-30.

Given the superior stability of ZIFs in aqueous environments as compared to MOFs,[177,178] our research endeavor focused on ZIF-70 and ZIF-82. To validate the accuracy of our methodology, we also investigated CALF-20 and ZIF-8, which have also been established as stable systems capable of adsorbing CO_2,[112,209] to compare our findings with those of Al-Attas et al. (2021).[210] In this study, the researchers found that both CALF-20 and ZIF-8 were promising catalysts for the reduction of CO_2 to CO, as a result of their high activity and selectivity.[210] In particular, CALF-20 showed the highest reported Faradaic Efficiency (FE) for zinc-based MOFs, with a FE of roughly 94% at -0.97 V versus reversible hydrogen electrode (RHE).[210] In comparison, ZIF-8 was found to have a FE of 61.1% at -0.97 V vs RHE.[210] [111,208]The structures we analyzed are displayed in Figure 26.

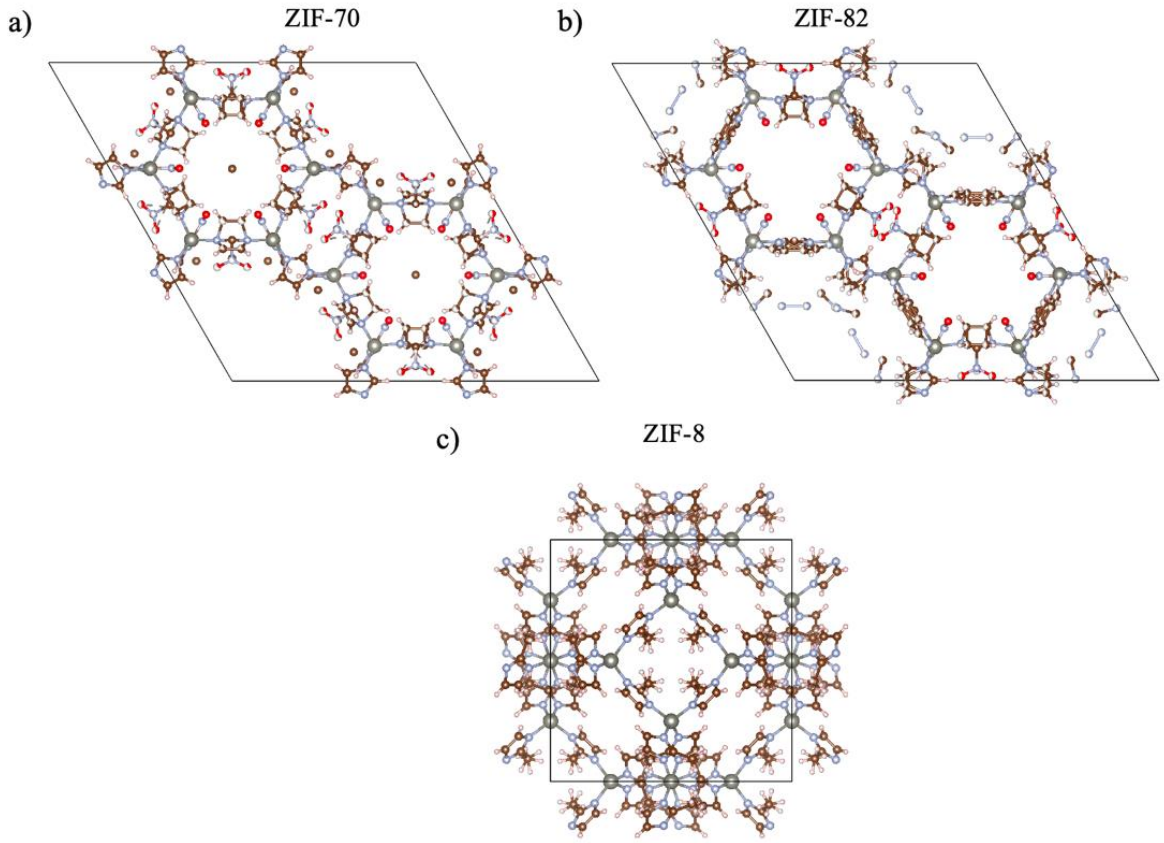

Figure 26: Structures of ZIFs and MOFs investigated in this study, including a) ZIF-70 b) ZIF-82, and c) ZIF-8.

In order to determine the adsorption energies for the two-electron CO_2RR, the unit cells of ZIF-70, ZIF-82 and ZIF-8 were constructed (Figure 27).

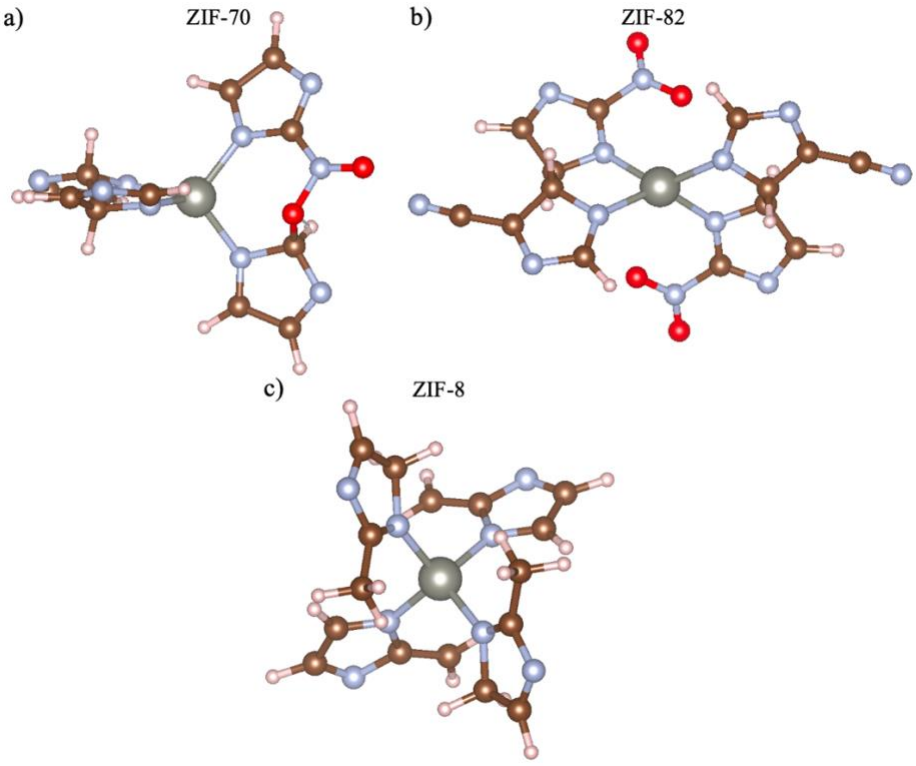

Figure 27: Unit cells of the structures investigated in this study, including a) ZIF-70 b) ZIF-82, and c) ZIF-8.

4.2) Overview of Calculating Adsorption Free Energies

The electrochemical reduction of CO_2 is a complex process that involves multiple electron and proton transfer steps, making it difficult to achieve high selectivity and efficiency for desired products. Therefore, understanding the fundamental concepts of charge transfer efficiency (CHE), limiting potential, and overpotential is crucial in this context.

CHE is a measure of the efficiency with which an electrochemical reaction proceeds with the transfer of charge between the electrode and the electrolyte.[211] This concept represents the ratio of the actual amount of charge transferred in an

electrochemical reaction to the theoretical amount of charge that could be transferred if the reaction were 100% efficient. It plays a significant role in determining the selectivity of the CO_2RR process.[211]

The limiting potential, on the other hand, is the thermodynamic potential at which an electrochemical reaction proceeds with the maximum possible rate, assuming ideal conditions. This potential is determined by the difference in the standard free energies of the reactants and products involved in the reaction. Knowledge of the limiting potential can help us to choose an appropriate operating potential for the electrochemical cell that maximizes the rate of CO_2 reduction while avoiding undesirable side reactions.[211]

Overpotential is a critical factor that affects the efficiency of the CO_2RR process. It is defined as the difference between the applied potential and the limiting potential and represents the energy required to drive the reaction at a given rate.[211] Overpotential is often used as a measure of the efficiency of an electrochemical reaction since higher overpotentials indicate greater energy losses due to non-ideal reaction kinetics, such as charge transfer resistance at the electrode/electrolyte interface.[211] By minimizing the overpotential, researchers can reduce the energy losses associated with non-ideal reaction kinetics, which can significantly improve the energy efficiency of CO_2 reduction.[211] Thus, in the analysis of the identified systems towards the two-electron CO_2RR, we will be also studying the limiting potentials and overpotentials for each active site, to identify the most promising systems.

When studying the two-electron CO_2RR, it is important to first understand the process. The reduction mechanism of CO_2 to CO involves several sequential steps and intermediates, which can be seen in Figure 28.

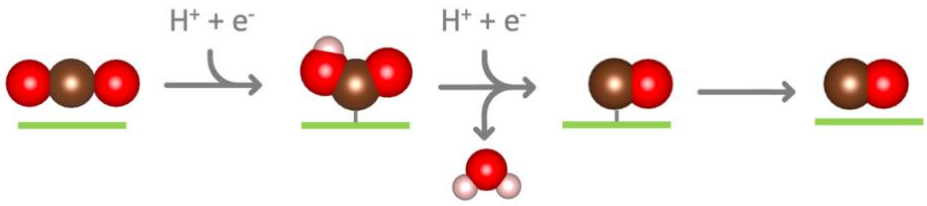

Figure 28: The two-electron CO_2 reduction reaction

Firstly, CO_2 is adsorbed onto the catalyst surface. Subsequently, the CO_2 molecule is activated through surface interactions, which potentially include cleaving one of the carbon-oxygen (C-O) bonds in CO_2. Next, the activated CO_2 undergoes a series of protonation and electron transfer steps, yielding intermediate species such as *COOH and *CO. Finally, these intermediates facilitate the production of CO, which serves as the ultimate product of the two-electron CO_2RR process, as can be noted in Equation 4. The electrons required for the reactions to proceed may be obtained from the ligands which are coordinated around the metal centers.

$$CO_2 + 2(H^+ + e^-) \rightarrow CO + H_2O \qquad E^o = -0.12\,V \qquad [4]$$

A competing reaction which occurs alongside the CO_2RR is the Hydrogen Evolution Reaction (HER) which proceeds via the following reaction:

$$2(H^+ + e^-) \rightarrow H_2 \qquad E^o = 0\,V \qquad [5]$$

HER can be defined as a process in which hydrogen ions and electrons combine to form molecular hydrogen (H_2) at the surface of a catalyst. This reaction holds significant relevance in the context of CO_2 reduction, as it often acts as a competing reaction in electrochemical systems designed for this purpose, thereby interfering with the desired CO_2 reduction reaction.[212] Specifically, in the case of CO_2 reduction via an electrocatalyst, the HER can be a potential side reaction that produces hydrogen gas, rather than reducing CO_2, thus resulting in reduced efficiency and selectivity of the process towards the intended product.[212] Therefore, it becomes imperative to consider the HER to ensure that the CO_2 is favored over the HER, by designing and optimizing electrocatalysts that selectively catalyze the desired reaction while minimizing the competing HER. We did not investigate other potential reactions such as the Oxygen Reduction Reaction or the Oxygen Evolution Reaction, as these would not have had an effect on our results since their potentials are greater than 0 V. In comparison, the CO_2RR occurs at potentials between 0 to -1 V.

4.3) Calculating the Adsorption Free Energies

Various active sites in each Zn-MOFs were investigates including the sp^2-C atoms located on the imidazolate rings in each system, and Zn cores. We find Zn nodes are not active towards CO_2RR. However, the sp^2-C atoms are the active sites for CO_2RR to CO, which is in agreement with the previous reports on Zn-based MOFs.[126,138,213] The calculated adsorption energies can be found in Appendix B. Most of the active sites studied did not yield suitable results as the configurations of the systems had altered; more specifically, the systems were found to be unstable as they lost their original

bonding. Subsequently, the best active sites that were identified for each system were able to maintain their configurations and is illustrated in Figure 29. Among these three systems, ZIF-82 and ZIF-70 exhibited the highest activity as catalysts for CO_2RR to CO. This is an intriguing finding, as ZIF-8 has been previously identified as a good catalyst for CO production.[213–215] However, although the ZIF-70 and ZIF-82 systems shows more activity towards the two-electron CO_2RR, they are unsuitable catalysts due to their strong binding of the *COOH intermediate, resulting in surface poisoning.

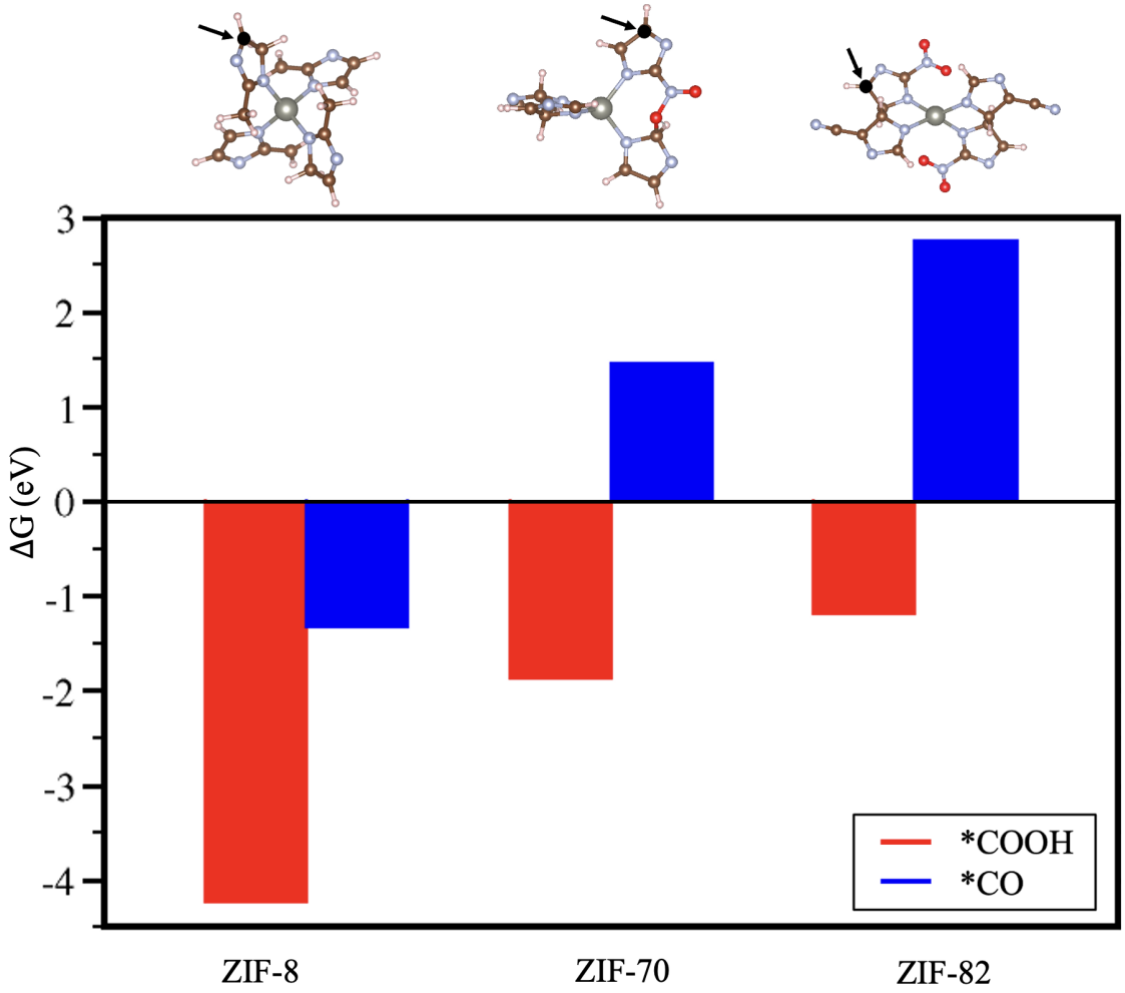

Figure 29: Gibbs free energy (eV) for the *COOH (red) intermediate and *CO (blue) intermediate for ZIF-70, ZIF-82 and ZIF-8. The active site for each molecule is highlighted in black.

We endeavored to conduct a further study aimed at scrutinizing and comparing the adsorption energies of all three systems as presented in Figure 30. The analysis was conducted under distinct applied voltages, where Figure 30s illustrates the reaction under no applied voltage, Figure 30b denotes the reaction under the standard potential for the reaction (-0.12 V), and Figure 30c indicates the reaction under a voltage of -1 V. Our observations from the figure reveal that except for the application of -1 V, applying varying voltages yielded no significant change to the reaction. Upon reviewing Figure 30c, it becomes evident that ZIF-8 is unsuitable for this reaction, followed by ZIF-82 and ZIF-70 in that order. This conclusion is drawn from an analysis of the energy required to overcome each uphill step. Consequently, the application of voltage confirms ZIF-8 as the weakest catalyst for this reaction and shows how the newly identified ZIF-70 and ZIF-82 are also unsuitable for the reaction.

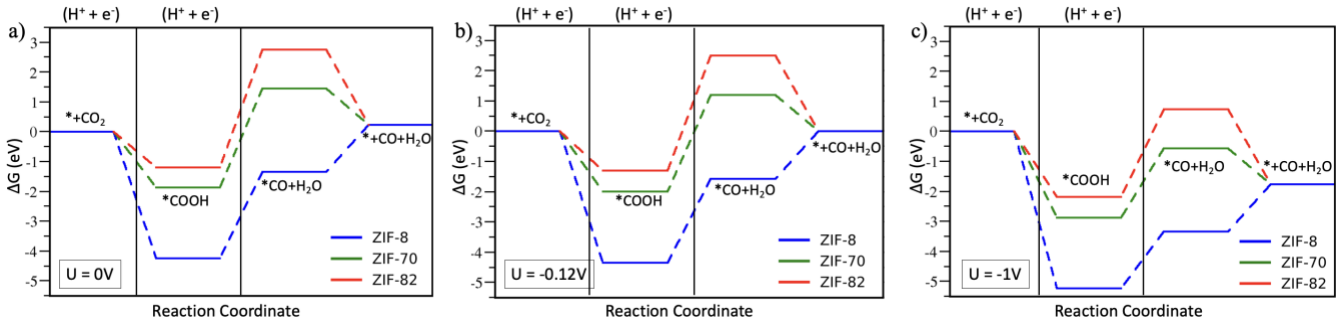

Figure 30: Gibbs free energy diagrams (eV) for the two-electron CO_2 reduction reaction with varying applied voltages a) 0 V, b) -0.12 V and c) 1V for ZIF-70 (green), ZIF-82 (red) and ZIF-8 (blue).

To ascertain the amount of energy that needs to be supplied to the system, we conducted an analysis to determine the overpotential required for each system to surmount their individual rate-determining steps, which for all systems is the formation of

*CO. As demonstrated in Figure 31, ZIF-8 exhibited the lowest overpotential, followed by ZIF-70, and ZIF-82, in that order.

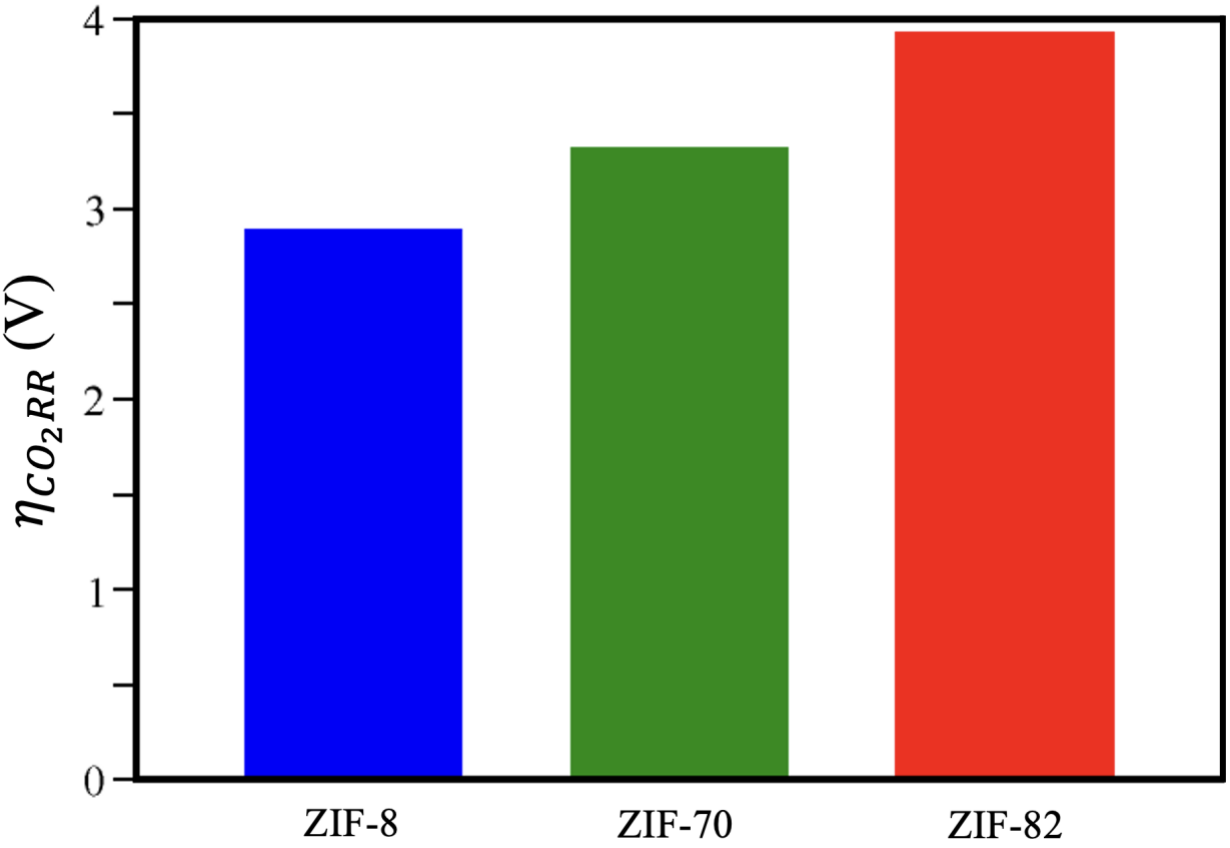

Figure 31: The calculated overpotentials (V) for ZIF-70 (green), ZIF-82 (red) and ZIF-8 (blue). for the identified active sites for each system

We also investigated the limiting potentials for each system, as noted by Table 5. The limiting potential is the minimum potential required for the CO_2RR reaction to proceed. ZIFs 8, 70 and 82 have higher limiting potentials, indicating that they require more energy for the *CO step. Although the systems under study are ill-suited for the CO_2RR, they are quite favorable for the competing Hydrogen Evolution Reaction.

Table 5: Calculated limiting potentials (V) for ZIF-8, ZIF-70, and ZIF-82.

	ZIF-8	ZIF-70	ZIF-82
U_L (V)	3.02	3.45	4.05

We conducted an analysis of the Hydrogen Evolution Reaction to determine the competition between the formation of H_2 and the desired product of CO. The results, as presented in Figure 32, indicate that ZIF-8 exhibit a very low ΔG towards the HER, signifying that this reaction will result in surface poisoning by the *H intermediate. Conversely, both ZIF-70 and ZIF-82 exhibit a less negative ΔG, indicating that the HER is more favorable for these systems.

These findings suggest that the newly identified ZIF-70 and ZIF-82 systems show a higher activity towards the HER over the CO_2RR, as it is energetically more favourable.

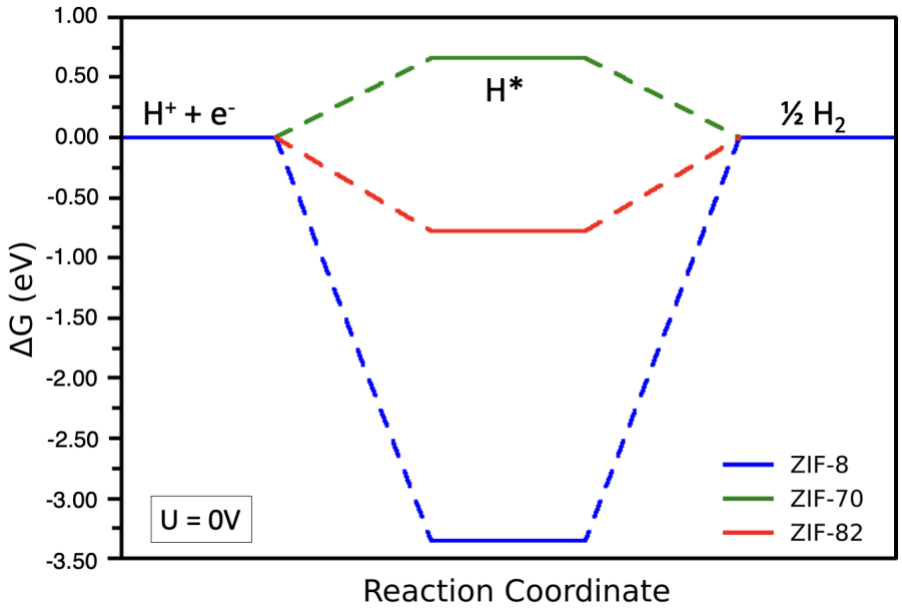

Figure 32: Gibbs free energy (eV) for the hydrogen evolution reaction at 0V for ZIF-70 (green), ZIF-82 (red) and ZIF-8 (blue).

4.4) HOMO/LUMO and Charge Density

In order to understand the reasons behind activity of the sp^2-C atoms located on the imidazolate rings, as well as to confirm our identification of the active sites, we conducted an electronic structure analysis of the charge density, as well as the analysis of HOMO and LUMO for each of the three systems (Figure 33). The HOMO and LUMO orbitals represent the highest and lowest energy levels that electrons can occupy in a molecule, respectively. Generally, the HOMO is the orbital from which electrons are most likely to be removed, while the LUMO is the orbital where electrons are most likely to be added.

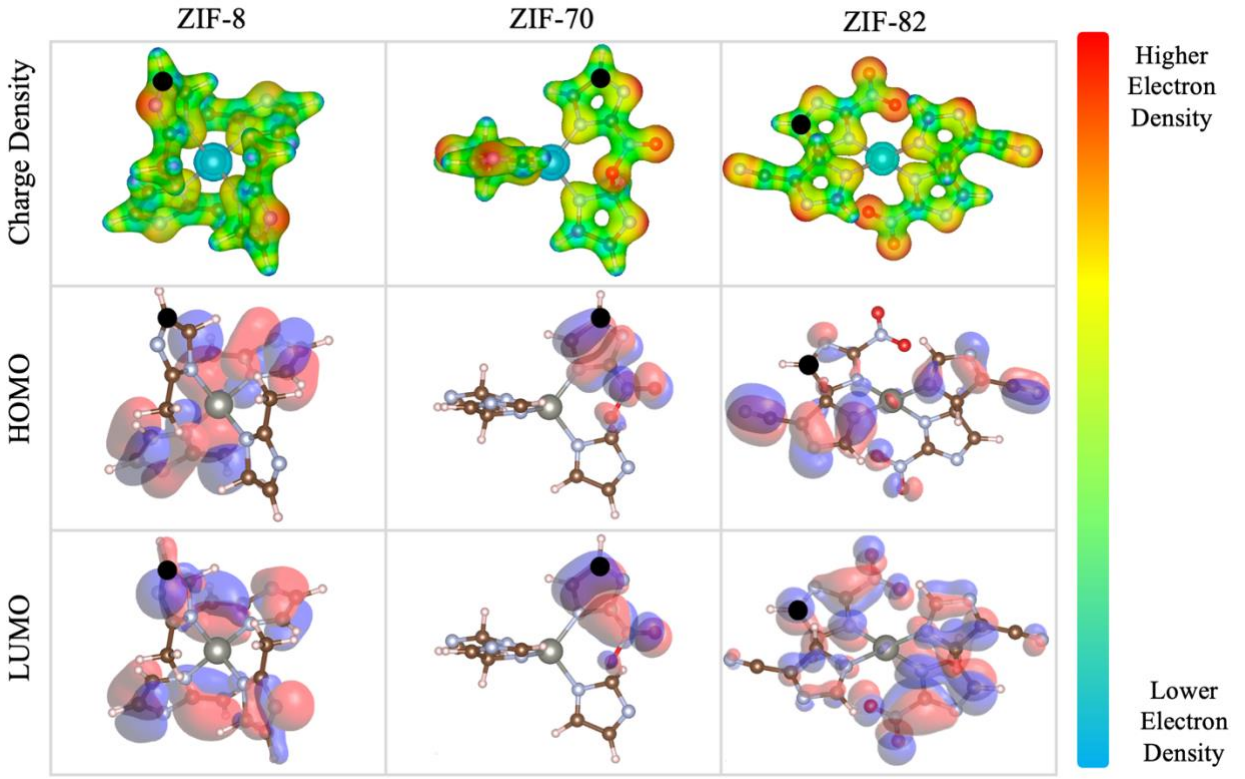

Figure 33: HOMO and LUMO for ZIF-8, ZIF-70, and ZIF-82. The active site for each molecule is highlighted in black. Red colour on the charge density indicates a higher electron density, while the blue indicates a lower electron density.

The blue colour observed in the charge density, as well as the LUMO orbitals around the active site for each system suggests an induced positive charge around the sp^2-C atom located in the imidazolate ring, which in turn, makes it more accessible for the sp^2-C atom to bind with the intermediates. Additionally, the charge density and HOMO orbitals for the neighbouring nitrogen groups reveal a higher electron density around the nitrogen, indicated by the red colour. This characteristic enables a more substantial overlap with the sp^2-C atom and facilitates the binding of the intermediates, *COOH and *CO, ultimately leading to the production of CO. Based on our findings, it can be concluded that the observed active sites are indeed valid and can be explained by the respective HOMO/LUMO orbitals of each system.

In conclusion, the present study investigated the active sites in Zn-MOFs for the reduction of CO_2 to CO. The obtained results demonstrate that the active sites for CO_2 reduction to CO are located on the sp^2-C atoms situated on the imidazolate rings, while the Zn nodes do not exhibit any activity. The three Zn-MOF systems investigated in this study were unsuitable catalysts towards the production of CO as a result of a strong binding of the *COOH intermediate. Furthermore, the investigation of the Hydrogen Evolution Reaction indicated that the ZIF-70 and ZIF-82 systems could be considered as suitable catalysts for the production of hydrogen due to the HER being energetically favorable. An electronic structure analysis of the charge density and HOMO/LUMO orbitals was conducted to comprehend the reasons underlying the activity of the sp^2-C atoms. This analysis confirmed the activity of the active sites and revealed that it was due to the electron-dense nitrogen atoms that drove the activity of the neighbouring sp^2-C atoms.

5 Conclusion

This chapter starts by outlining the objectives of the thesis, which are discussed (5.1). Additionally, an assessment is conducted on potential improvements that could enhance the system's stability and performance, along with other studies that could further reinforce the findings (5.2). Finally, a summary of the entire thesis is presented, culminating in a final evaluation of the work and its results (5.3).

5.1) Goals Accomplishments

At the beginning of the thesis, a list of goals was laid down to help guide the research and to help achieve final positive results. Table 6 lists the goals for the CO_2 capture portion of the thesis and their respective level of accomplishment.

Table 6: Level of accomplishment of the thesis's goals towards CO_2 Capture

Research Goal	Level of Accomplishment
Stable Under Changing Temperature	Not Accomplished
Stable in the Presence/Absence of Water	Not Accomplished
Template Molecules Should Increase Stability	Accomplished
Able to Successfully Capture CO_2	Not Accomplished

Despite most of the objectives not being attained, we were able to identify the underlying cause for the failures. Initially, thermal agitation led to a minor distortion of the network, which resulted in a gradual reduction of the pore volume, ultimately leading to the collapse of the MOF. This phenomenon was further observed during the dehydration process of HCALF-5 to CALF-50. The collapse of the MOF's porous structure was

attributed to the lack of hydrogen bonds coordinating the phosphonates around the metallic center, and the removal of water molecules from the system. However, the incorporation of xylene template molecules into the pores of both HCALF-50 and CALF-50 resulted in the preservation of the pore architecture. Additionally, it was observed that the p-xylene template molecules were most effective in maintaining the structure of CALF-50's pores. Regrettably, despite the presence or absence of the template molecules, both systems were unable to efficiently capture CO_2, as indicated by the diffusion of this molecule throughout the pores of both MOFs. Nonetheless, it was recognized that template molecules can serve as a beneficial means of stabilizing an otherwise unstable system, even though this particular MOF was deemed ineffective in capturing CO_2.

For the second part of the thesis, Table 7 summarizes the goals and level of accomplishment towards to the CO_2RR on identified CoRE MOFs.

Table 7: Level of accomplishment of the thesis's goals towards the CO_2 reduction reaction

Research Goal	Level of Accomplishment
Able to Capture CO_2 and is Water Stable	Accomplished
Able to Successfully Reduce CO_2 to CO	Not Accomplished

The present study identified several MOFs and ZIFs that were water-stable and capable of capturing CO_2, namely ZIF-8, ZIF-70, and ZIF-82. The assessment of their catalytic activity towards the two-electron CO_2 reduction reaction revealed that the systems did not exhibited sufficient CO production as a result of surface poisoning by the

*COOH intermediate. Furthermore, the investigation of the Hydrogen Evolution Reaction indicated that the ZIF-70 and ZIF-82 systems could be considered as good catalysts for this reaction. Finally, an analysis on the charge density, as well as the HOMO/LUMO of each system confirmed the activity of the active sites and revealed that it was due to the electron-dense nitrogen atoms that drove the activity of the neighbouring sp^2-C atoms. Although this investigation did not result in the identification of two new catalysts towards the CO_2RR, we were able to show that the ZIF-70 and ZIF-82 systems were unsuitable for this reaction.

5.2) Future Work

The present study has demonstrated that HCALF-50 exhibits limited efficacy in capturing CO_2 and has identified the factors contributing to the instability of the MOF. However, future investigations may be pursued to explore methods to enhance the stability of the system. Additionally, further research may be conducted to optimize the capacity of the MOFs in retaining CO_2 within their pores, and to prevent its diffusion. We may also study the effect of decreasing the temperature on the systems, to determine if they are able to maintain their porosity and configuration.

Moreover, the identification of the MOFs, tp-PMBB-1-asc-1, MOF-74 and SNU-30, for CO_2 reduction reaction presents a promising avenue for further study. These systems could be studied computationally to determine their efficacy towards the CO_2RR, and later confirmed through additional experiments. We can also change the criteria for the pore limiting diameter from >10Å to >5Å to identify other MOFs that can be used as bifunctional catalysts for CO_2 capture and reduction.

5.3) Final Appreciation

The present investigation aimed to evaluate the efficacy of HCALF-50 and CALF-50 as systems for the direct air capture of CO_2. Regrettably, the endeavor did not yield the intended results. However, the study provided insights into enhancing the stability of both systems, demonstrating that it is indeed feasible.

Additionally, the exploration of the CoRE MOF Database yielded the identification of three MOFs that needs to be studied further, which may serve as bifunctional agents capable of efficiently capturing CO_2 from the atmosphere and reducing it to CO, thereby facilitating the production of syngas in an eco-friendly manner.

The potential of the systems under scrutiny is unequivocally evident, and with sustained research and development efforts, they could achieve the requisite standard for commercial application in both carbon capture and reduction. To conclude, it can be inferred that both research undertakings were successful.

References

1. Olah, G. A.; Prakash, G. K. S.; Goeppert, A. Anthropogenic Chemical Carbon Cycle for a Sustainable Future. *J. Am. Chem. Soc.* **2011**, *133*(32), 12881–12898.

2. Wang, X.; Song, C. Carbon Capture from Flue Gas, and the Atmosphere: A Perspective. *Front. Energy Res.* **2020**, *8*.

3. Shepardson, D. P.; Choia, S.; Niyogi, D.; Charusombat, U. Seventh Grade Students' Mental Models of the Greenhouse Effect. *Environ. Educ. Res.* **2011**, *17*(1), 1–17.

4. Kweku, D. W.; Bismark, O.; Maxwell, A.; Desmond, K. A.; Danso, K. W.; Oti-Mensah, E. A.; Quachie, A. T.; Adormaa, B. B. Greenhouse effect: greenhouse gases and their impact on global warming. *J. Sci. Res.* **2018**, *17*(6), 1-9.

5. Brown, L. R.; Larsen, J.; Roney, J. M.; Adams, E. E. The Great Transition: Shifting from Fossil Fuels to Solar and Wind Energy. *W. W. Norton & Co.*, **2015**.

6. Chen, J. M. Carbon Neutrality: Toward a Sustainable Future. *Innovation*(China) **2021**, *2*,

7. Hofmann, D. J.; Butler, J.; Montzka, S. A.; Harris, J. M.; Elkins, J. W.; Thompson, T. M.; Swanson, T. H. The Role of Carbon Dioxide in Climate Forcing from 1979 to 2004: Introduction of the Annual Greenhouse Gas Index. *Tellus, Ser. B-Chem. Phys. Meteorol.* **2006**, *58*(5), 614–619.

8. NOAA Global Monitoring Laboratory. Annual Greenhouse Gas Index. *Global Change* **2021**.

9. Lindsey, R. Climate Change: Annual Greenhouse Gas Index. *NOAA Climate* **2022**.

10. Butler, J.; Hall, B. D.; Montzka, S. A.; Mondeel, D. J.; Elkins, J. W.; Dutton, G. S.; Hall, G. E.; Nance, D.; Wuebbles, D. J. The NOAA Annual Greenhouse Gas Index (AGGI). *NOAA Earth System Research Laboratory* **2016**, *58*.

11. Johnsson, F.; Kjarstad, J.; Odenberger, M. The importance of CO2 capture and storage - A geopolitical discussion. *Thermal Science* **2012**, *16*, 655–668.

12. Merkel, T. C.; Lin, H.; Wei, X.; Baker, R. Power plant post-combustion carbon dioxide capture: An opportunity for membranes. *J. Memb. Sci.* **2010**, *359*, 126–139.

13. Volkart, K.; Bauer, C.; Boulet, C. Life cycle assessment of carbon capture and storage in power generation and industry in Europe. *Int. J. Greenh. Gas Control* **2013**, *16*, 91–106.

14. Farla, J. C. M.; Hendriks, C. A.; Blok, K. Carbon dioxide recovery from industrial processes. *Climate Change* **1995**, *29*, 439–461.

14. Ho, M. T.; Allinson, G. W.; Wiley, D. E. Comparison of MEA capture cost for low CO2 emissions sources in Australia. *Int. J. Greenh. Gas Control* **2011**, *5*, 49–60.

15. Gabrielli, P.; Gazzani, M.; Mazzotti, M. The role of carbon capture and utilization, carbon capture and storage, and biomass to enable a net-zero-CO2 emissions chemical industry. *Ind. Eng. Chem. Res.* **2020**, *59*, 7033–7045.

16. Boot-Handford, M. E.; Abanades, J. C.; Anthony, E. J.; Blunt, M. J.; Brandani, S.; Mac Dowell, N.; Fernández, J. R.; Ferrari, M. C.; Gross, R.; Hallett, J. P.; Haszeldine, R. S.; Heptonstall, P.; Lyngfelt, A.; Makuch, Z.; Mangano, E.; Porter, R. T. J.; Pourkashanian, M.; Rochelle, G. T.; Shah, N.; Yao, J. Carbon capture and storage update. *Energy Environ. Sci.* **2014**, *7*, 130–189.

17. D'Alessandro, D. M.; Smit, B.; Long, J. R. Carbon dioxide capture: prospects for new materials. *Angew. Chem. Int. Ed.* **2010**, *49*, 6058–6082.

18. Gielen, D. CO2 removal in the iron and steel industry. *Energy Convers. Manage.* **2003**, *44*, 1027–1037.

19. Brunetti, A.; Scura, F.; Barbieri, G.; Drioli, E. Membrane technologies for CO2 separation. *J. Memb. Sci.* **2010**, *359*, 115–125.

20. Kamyab, H.; Ramanan, R. N.; Alkarkhi, A. F. M.; Velloo, R. G.; Nathan, G. Efficiency of *Chlamydomonas* Microalgae on the Removal of Pollutants from Palm Oil Mill Effluent (POME). *Energy Procedia* **2015**, *75*, 2400-2408.

21. Fulazzaky, M. A.; Yusoff, M. S.; Salim, M. R. Biofiltration process as an ideal approach to remove pollutants from polluted air. *Desalination Water Treat* **2014**, *52*, 3600-3615.

22. Tuinier, M. J.; Van Sint Annaland, M. Biogas purification using cryogenic packed-bed technology. *Ind Eng Chem Res* **2012**, *51*, 5552-5558.

23. Camper, D.; Bara, J. E.; Gin, D. L.; Noble, R. D. Room-temperature ionic liquid-amine solutions: Tunable solvents for efficient and reversible capture of CO2. *Ind Eng Chem Res* **2008**, *47*, 8496-8498.

24. Petrescu, L.; Cormos, C. C. Environmental assessment of IGCC power plants with pre-combustion CO2 capture by chemical & calcium looping methods. *J Clean Prod* **2017**, *158*, 233-244.

25. Hwang, C. C.; Cheng, S. T.; Li, S. Y.; Huang, C. C.; Li, Y. C.; Kuo, C. H.; Lee, W. Y.; Wang, C. C. Capturing Carbon Dioxide as a Polymer from Natural Gas. *Nat. Commun.* **2014**, *5*, 4961.

26. Abanades, J. C.; Anthony, E. J.; Benito, Y.; Grande, C.; Lyngfelt, A.; Mattisson, T.; Muraza, O.; Papp, J.; Pourkashanian, M.; Sánchez-Biezma, A.; and Song, C. Emerging CO2 Capture Systems. *Int. J. Greenhouse Gas Control* **2015**, *40*, 126-166.

27. Fingas, M. Physical Spill Countermeasures. In *Oil Spill Science and Technology*; Elsevier Inc., **2011**, 303-337.

28. Pardakhti, M.; Akbari, M. K.; Rahimpour, M. R.; Mohammadi, T. Trends in Solid Adsorbent Materials Development for CO2 Capture. *ACS Appl. Mater. Interfaces* **2019**, *11*, 34533-34559.

29. Samanta, A.; Zhao, A.; Shimizu, G. K. H.; Sarkar, P.; Gupta, R. Post-combustion CO2 capture using solid sorbents: A review. *Ind Eng Chem Res* **2012**, *51*, 1438-1463.

30. Chen, Z.; Wang, Q.; Wang, S.; Zhang, X.; Gong, X.; Li, S. Activated carbons and amine-modified materials for carbon dioxide capture--A review. *Frontiers in Environmental Science & Engineering* **2013**, *7*, 326-340.

31. Kumar, K. V.; Preuss, K.; Lu, L.; Guo, Z. X.; Titirici, M. M. Effect of Nitrogen Doping on the CO2 Adsorption Behavior in Nanoporous Carbon Structures: A Molecular Simulation Study. *J. Phys. Chem. C* **2015**, *119*, 22310-22321.

32. Chue, K. T.; Kim, J. N.; Yoo, Y. J.; Cho, S. H.; Yang, R. T. Comparison of Activated Carbon and Zeolite 13X for CO2 Recovery from Flue Gas by Pressure Swing Adsorption. *Ind. Eng. Chem. Res.* **1995**, *34*, 2499-2506.

33. Wang, Y.; Zhou, Y.; Liu, C.; Zhou, L. Comparative studies of CO2 and CH4 sorption on activated carbon in presence of water. *Colloids Surf. A* **2008**, *322*, 14-18.

34. Foley, H. C. Carbogenic molecular sieves: synthesis, properties and applications. *Microporous Mater.* **1995**, *4*, 433-442.

35. Rutherford, S. W.; Do, D. D. Adsorption dynamics of carbon dioxide on a carbon molecular sieve 5A. *Carbon* **2000**, *38*, 1585-1593.

36. Brandani, F.; Ruthven, D. M. The effect of water on the adsorption of CO2 and C3H8 on type X zeolites. *Ind. Eng. Chem. Res*. **2004**, *43*, 8339-8344.

37. Kitagawa, S.; Matsuda, R. Chemistry of coordination space of porous coordination polymers. *Coord. Chem. Rev*. **2007**, *251*, 2490-2509.

38. Czaja, A. U.; Trukhan, N.; Müller, U. Industrial applications of metal–organic frameworks. *Chem. Soc. Rev.* **2009**, *38,* 1284-1293.

39. James, S. L. Metal-organic frameworks. *Chem. Soc. Rev*. **2003**, *32*, 276-288.

40. Morris, R. E.; Wheatley, P. S. Gas Storage in Nanoporous Materials. *Angew. Chem. Int. Ed*. **2008**, *47*, 4966-4981.

41. Yang, Q.; Yang, C. C.; Lin, C. H.; Jiang, H. L. Metal–Organic-Framework-Derived Hollow N-Doped Porous Carbon with Ultrahigh Concentrations of Single Zn Atoms for Efficient Carbon Dioxide Conversion. *Angew. Chem. Int. Ed*. **2019,** *58*, 3511-3515.

42. Fiorani, G.; Guo, W.; Kleij, A. W. Sustainable Conversion of Carbon Dioxide: The Advent of Organocatalysis. *Green Chem.* **2015**, *17*, 1375-1389.

43. Alissandratos, A.; Easton, C. J. Biocatalysis for the Application of CO2 as a Chemical Feedstock. Beilstein *J. Org. Chem*. **2015**, *11*, 2370-2387.

44. Han, B.; Li, D.; Li, Y.; Li, Z.; Li, X.; Shi, W.; Li, Y. Nickel Metal–Organic Framework Monolayers for Photoreduction of Diluted CO2: Metal-Node-Dependent Activity and Selectivity. *Angew. Chem.* **2018**, *130*, 17053-17057.

45. Li, C.; Wang, H.; Guo, Y.; Shi, R.; Li, C. Photoelectrochemical CO2 Reduction to Adjustable Syngas on Grain-Boundary-Mediated a-Si/TiO2/Au Photocathodes with Low Onset Potentials. *Energy Environ. Sci*. **2019**, *12*, 923-928.

46. Li, M.; Liu, Q.; Gao, J.; Feng, X. Heterogeneous Single-Atom Catalysts for Electrochemical CO2 Reduction Reaction. *Adv. Mater. 2020, 32*, 2001848.

47. Ross, M. B.; De Luna, P.; Li, C.; Kim, T. K.; Yang, P. Designing Materials for Electrochemical Carbon Dioxide Recycling. *Nat. Catal.* **2019**, *2*, 648-658.

48. Vasileff, A.; Xu, C.; Jiao, Y.; Zheng, Y.; Qiao, S. Z. Selectivity Control for Electrochemical CO2 Reduction by Charge Redistribution on the Surface of Copper Alloys. *ACS Catal*. **2019**, *9*, 9411-9417.

49. Takeda, H.; Cometto, C.; Ishitani, O.; Robert, M. Electrons, Photons, Protons and Earth-Abundant Metal Complexes for Molecular Catalysis of CO2 Reduction. *ACS Catal*. **2017**, *7*, 70-88.

50. Franco, F.; Fernández, S.; Lloret-Fillol, J. Advances in the electrochemical catalytic reduction of CO2 with metal complexes. *Curr. Opin. Electrochem*. **2020**, *15*, 109-117.

51. Zhang, L.; Zhao, Z.-J.; Gong, J. Nanostrukturierte Materialien für die elektrokatalytische CO2-Reduktion und ihre Reaktionsmechanismen. *Angew. Chem*. **2017**, *129*, 11482-11511.

52. Luc, W.; Jessop, P. G.; Guo, X.; Wang, S.; Zhang, X.; Li, S. Ag-Sn Bimetallic Catalyst with a Core-Shell Structure for CO2 Reduction. *J. Am. Chem. Soc*. **2017**, *139*, 1885-1893.

53. Kumar, B.; Asadi, M.; Pisasale, D.; Phillips, P.; Abiade, J.; Haasch, R.; Yarin, A. L.; Salehi-Khojin, A. Controlling the Product Syngas H2:CO Ratio through Pulsed-Bias Electrochemical Reduction of CO2 on Copper. *ACS Catal*. **2016**, *6*, 4739-4745.

54. Duan, X.; Xu, Y.; Chen, S.; Wang, Q.; Li, Y. Metal-Free Carbon Materials for CO2 Electrochemical Reduction. *Adv. Mater.* **2017***, 29.*

55. Tekalgne, M. A.; Cao, C.; Wang, X. Two-dimensional materials and metal-organic frameworks for the CO2 reduction reaction. *Mater. Today Adv*. **2020**, *5*.

56. Gattrell, M.; Gupta, N.; Co, A. A review of the aqueous electrochemical reduction of CO2 to hydrocarbons at copper. *J. Electroanal. Chem*. **2006**, *594*, 1-19.

57. Abubackar, H. N.; Veiga, M. C.; Kennes, C. Syngas Fermentation for Bioethanol and Bioproducts. In Sustainable Resource Recovery and Zero Waste Approaches; *Elsevier*: **2019**, 207-221.

58. El-Nagar, R. A.; Ghanem, A. A. Syngas Production, Properties, and Its Importance. **2019**, *2.*

59. Dry, M. E. The Fischer-Tropsch Process: 1950-2000. *Catal. Today* **2002**, *71*, 227-241.

60. Huber, G. W.; Iborra, S.; Corma, A. Synthesis of transportation fuels from biomass: Chemistry, catalysts, and engineering. *Chem. Rev.* **2006**, *106*, 4044-4098.

61. Dincer, I.; Rosen, M. A. Exergy: Energy, environment and sustainable development. *Elsevier*, **2012**.

62. Lu, S.; Zhang, X.; Yu, Q.; Zhang, L.; He, C.; Sun, Y.; Wang, Z.; Liu, Y.; Peng, X.; Lu, Y. Electrosynthesis of Syngas via the Co-Reduction of CO2 and H2O. *Cell Reports Phys. Sci*. **2020**, *1*, 100237.

63. Chen, Q.; Tsiakaras, P.; Shen, P. Electrochemical Reduction of Carbon Dioxide: Recent Advances on Au-Based Nanocatalysts. *Catalysts* **2022**, *12*, 1348.

64. Kitagawa, S.; Kitaura, R.; Noro, S. I. Functional porous coordination polymers. *Angew. Chem. Int. Ed*. **2004**, *43*, 2334-2375.

65. Zhou, H. C. J.; Kitagawa, S. Metal-Organic Frameworks (MOFs). *Chem. Soc. Rev*. **2014**, *43*, 5415–5418.

66. Yaghi, O. M.; Li, G.; Li, H. Selective Binding and Removal of Guests in a Microporous Metal-Organic Framework. *Nature* **1995**, *378*, 703–706.

67. Düren, T.; Bae, Y. S.; Snurr, R. Q. Using Molecular Simulation to Characterize Metal-Organic Frameworks for Adsorption Applications. *Chem. Soc. Rev*. **2009**, *38*, 1237–1247.

68. Ma, S.; Sun, D.; Simmons, J. M.; Collier, C. P.; Yuan, D.; Zhou, H.-C. Framework-Catenation Isomerism in Metal-Organic Frameworks and Its Impact on Hydrogen Uptake. *J. Am. Chem. Soc*. **2007**, *129*, 1858–1859.

69. Lee, J.; Farha, O. K.; Roberts, J.; Scheidt, K. A.; Nguyen, S. T.; Hupp, J. Metal-Organic Framework Materials as Catalysts. *Chem. Soc. Rev*. **2009**, *38*, 1450–1459.

70. Halder, G. J.; Kepert, C. J.; Moubaraki, B.; Murray, K. S.; Cashion, J. D. Guest-Dependent Spin Crossover in a Nanoporous Molecular Framework Material. *Science* **2002**, *298*, 1762–1765.

71. Allendorf, M. D.; Bauer, C. A.; Bhakta, R. K.; Houk, R. J. T. Luminescent Metal-Organic Frameworks. *Chem. Soc. Rev*. **2009**, *38*, 1330–1352.

72. Li, H.; Eddaoudi, M.; O'Keeffe, M.; Yaghi, O. M. Design and Synthesis of an Exceptionally Stable and Highly Porous Metal-Organic Framework. *Nature* **1999**, *402*, 276–279.

73. MacDowell, N.; Florin, N.; Buchard, A.; Hallett, J. An Overview of CO2 Capture Technologies. *Energy Environ. Sci.* **2010**, *3*, 1645–1669.

74. Farrusseng, D.; Aguado, S.; Pinel, C. Metal-Organic Frameworks: Opportunities for Catalysis. *Angew. Chem., Int. Ed*. **2009**, *48*, 7502–7513.

75. Furukawa, H.; Cordova, K. E.; O'Keeffe, M.; Yaghi, O. M. The Chemistry and Applications of Metal-Organic Frameworks. *Science* **2013**, *341*, 1230444.

76. Zhou, H. C.; Long, J. R.; Yaghi, O. M. Introduction to Metal-Organic Frameworks. *Chem. Rev.* **2012**, *112*, 673–674.

77. Abánades Lázaro, I.; Forgan, R. S. Application of Zirconium MOFs in Drug Delivery and Biomedicine. *Coord. Chem. Rev*. **2019**, *380*, 230–259.

78. Janiak, C.; Vieth, J. K. MOFs, MILs and More: Concepts, Properties, and Applications for Porous Coordination Networks (PCNs). *New J. Chem*. **2010**, *34*, 2366–2388.

79. Liu, J.; Keskin, S.; Sholl, D. S.; Johnson, J. K. Molecular simulations and theoretical predictions for adsorption and diffusion of CH4/H2 and CO2/CH4 mixtures in ZIFs. J. *Phys. Chem. C* **2011**, *115*, 12560–12566.

80. Cheng, N.; Ren, L.; Xu, X.; Du, Y.; Dou, S. X. Recent Development of Zeolitic Imidazolate Frameworks (ZIFs) Derived Porous Carbon-Based Materials as Electrocatalysts. *Adv. Energy Mater*. **2018**, *8*.

81. Wu, Y.; Chen, H.; Liu, D.; Qian, Y.; Xi, H. Adsorption and separation of ethane/ethylene on ZIFs with various topologies: Combining GCMC simulation with the ideal adsorbed solution theory (IAST). *Chem. Eng. Sci*. **2015**, *124*, 144–153.

82. Ighalo, J. O.; Gazi, M.; Sebunya, T. M.; Bello, O. S.; Ebenso, E. E. Zeolitic Imidazolate Frameworks (ZIFs) for aqueous phase adsorption – A review. *J. Ind. Eng. Chem*. **2022**, *105*, 34–48.

83. Sharma, R. K.; Pandey, M.; Soni, H.; Singh, A. K.; Rai, V. K.; Dhakate, S. R. Recent development of covalent organic frameworks (COFs): Synthesis and catalytic (organic-electro-photo) applications. *Mater. Horiz*. **2020**, *7*, 411–454.

84. Liu, X.; Ding, X.; Shi, W.; Tang, B. Z. Recent advances in covalent organic frameworks (COFs) as a smart sensing material. *Chem. Soc. Rev*. **2019**, *48*, 5266–5302.

85. Wang, J.; Zhuang, S. Covalent organic frameworks (COFs) for environmental applications. *Coord. Chem. Rev*. **2019**, *400*.

86. Ding, S. Y.; Wang, W. Covalent organic frameworks (COFs): From design to applications. *Chem. Soc. Rev*. **2013**, *42*, 548–568.

87. Xin, C.; Sun, D.; Zhang, Y.; Tian, J.; Lu, J.; Han, B.; Zhao, H.; Guo, Y.; Song, C.; Hu, Y.; Wang, C. Construction of Au and C60 quantum dots modified materials of Institute Lavoisier-125(Ti) architectures for antibiotic degradation: Performance, toxicity assessment, and mechanistic insight. *J. Colloid Interface Sci*. **2022**, *623*, 417–431.

88. Yang, S.; Yuan, S.; Zhu, L.; Chen, Y.; Zhou, H.-C. Materials Institute Lavoisier (MIL) based materials for photocatalytic applications. *Coord. Chem. Rev*. **2021**, *438*.

89. Lestari, W. W.; Kartini, I.; Adi, W. A.; Hilman, N. M. A. Fabrication of hybrid membranes based on poly(ether-sulfone)/Materials Institute Lavoisier (MIL-53) (Al) and its enhanced CO2 gas separation performance. *Chem. Pap*. **2021**, *75*, 6519–6530.

90. Martí-Rujas, J.; Castillo, O.; Raineri, F. O.; Sánchez, F.; Sánchez, L.; Velázquez, M. M.; Yuste, F. Dramatic structural rearrangements in porous coordination networks. *J. Am. Chem. Soc*. **2011**, *133*, 5853–5860.

91. Zhang, M.; Chen, Y. P.; Zhou, H. C. Structural design of porous coordination networks from tetrahedral building units. *CrystEngComm* **2013**, *15*, 9544–9552.

92. Kesanli, B.; Lin, W. Chiral porous coordination networks: Rational design and applications in enantioselective processes. *Coord. Chem. Rev*. **2003**, *246*, 305–326

93. Kawano, M.; Kawamichi, T.; Haneda, T.; Kojima, T.; Fujita, M. The modular synthesis of functional porous coordination networks. *J. Am. Chem. Soc.* **2007**, *129*, 15418–15419.

94. Maji, T. K.; Kitagawa, S. Chemistry of porous coordination polymers. *Pure Appl. Chem.* **2007**, *79*, 2155–2177.

95. Uemura, T.; Yanai, N.; Kitagawa, S. Polymerization reactions in porous coordination polymers. *Chem. Soc. Rev.* **2009**, *38*, 1228–1236.

96. Foo, M. L.; Matsuda, R.; Kitagawa, S. Functional hybrid porous coordination polymers. *Chem. Mater.* **2014**, *26*, 310–322.

97. Kitagawa, S.; Kitaura, R.; Noro, S. I. Functional porous coordination polymers. *Angew. Chem., Int. Ed.* **2004**, *43*, 2334–2375.

98. Li, P.; Ryder, M. R.; Stoddart, J. F. Hydrogen-Bonded Organic Frameworks: A Rising Class of Porous Molecular Materials. *Acc. Mater. Res.* **2020**, *1*, 77–87.

99. Liu, J.; Wang, J.; Su, X.; Zhang, Y.; Wei, G.; Xu, G.; Du, Y.; Wang, X. Rational Stepwise Construction of Different Heterometallic–Organic Frameworks (HMOFs) for Highly Efficient CO2 Conversion. *Chem. Eur. J.* **2020**, *26*, 5400–5406.

100. Li, J. R.; Kuppler, R. J.; Zhou, H. C. Selective gas adsorption and separation in metal-organic frameworks. *Chem. Soc. Rev.* **2009**, *38*, 1477–1504.

101. Wang, L.; Wang, K.; Wang, X.; Yao, J.; Wang, Y.; Wu, K. Metal–organic frameworks for energy storage: Batteries and supercapacitors. *Coord. Chem. Rev.* **2016**, *307*, 361–381.

102. Horcajada, P.; Gref, R.; Baati, T.; Allan, P. K.; Maurin, G.; Couvreur, P.; Férey, G.; Morris, R. E.; Serre, C. Metal-organic frameworks in biomedicine. *Chem. Rev.* **2012**, *112*, 1232–1268.

103. Vikrant, K.; Kumar, V.; Kim, K. H.; Kukkar, D. Metal-organic frameworks (MOFs): Potential and challenges for capture and abatement of ammonia. *J. Mater. Chem. A* **2017**, *5*, 22877–22896.

104. Farha, O. K.; Hupp, J. T. Rational design, synthesis, purification, and activation of metal-organic framework materials. *Acc. Chem. Res.* **2010**, *43*, 1166–1175.

105. Sumida, K.; Rogow, D. L.; Mason, J. A.; McDonald, T. M.; Bloch, E. D.; Herm, Z. R.; Bae, T.-H.; Long, J. R. Carbon dioxide capture in metal-organic frameworks. *Chem. Rev.* **2012**, *112*, 724–781.

105. Hon Lau, C., Babarao, R. & Hill, M. R. A route to drastic increase of CO2 uptake in Zr metal organic framework UiO-66. *Chem. Commun.* **2013**, *49*, 3634–3636.

106. Usman, M.; Liu, B.; Shoaib, M.; Zhang, Z.; Chen, H.; Sun, K.; Xia, Q.; Wang, Y.; Xia, Y.; Wang, Y. Trends and Prospects in UiO-66 Metal-Organic Framework for CO2 Capture, Separation, and Conversion. *Chem. Rec.* **2021**, *21*, 1771–1791.

107. Mutyala, S., Jonnalagadda, M., Mitta, H. & Gundeboyina, R. CO2 capture and adsorption kinetic study of amine-modified MIL-101 (Cr). *Chem. Eng. Res. Des.* **2019**, *143*, 241–248.

108. Ban, Y.; Liu, Y.; Zhao, L.; Liu, Y.; Li, Z.; Zhao, S. Confinement of Ionic Liquids in Nanocages: Tailoring the Molecular Sieving Properties of ZIF-8 for Membrane-Based CO2 Capture. *Angew. Chem. Int. Ed.* **2015**, *54*, 15703–15707.

109. Zheng, W.; Deng, M.; Tang, H.; Zhang, X.; Wang, S.; Wang, L.; Wang, S.; Xiao, J.; Song, Y.; Ma, X. ZIF-8 nanoparticles with tunable size for enhanced CO2 capture of Pebax based MMMs. *Sep. Purif. Technol.* **2019**, *214*, 111–119.

110. Thomas, A., Ahamed, R. & Prakash, M. Selection of a suitable ZIF-8/ionic liquid (IL) based composite for selective CO2capture: The role of anions at the interface. *RSC Adv.* **2020**, *10*, 39160–39170.

111. Song, C.; Huang, R.; Li, Z.; Zhang, L.; Chen, J.; Ma, Y.; Li, Y.; Li, J. Enhanced CO2 sorption and selectivity by functionalization of a NbO-type metal-organic framework with polarized benzothiadiazole moieties. *Chem. Commun.* **2014**, *50*, 12105–12108.

112. Darunte, L. A., Oetomo, A. D., Walton, K. S., Sholl, D. S. & Jones, C. W. Direct Air Capture of CO2 Using Amine Functionalized MIL-101(Cr). *ACS Sustain. Chem. Eng.* **2016**, *4*, 5761–5768.

113. Soltanolkottabi, F., Talaie, M. R., Aghamiri, S. & Tangestaninejad, S. Introducing a dual-step procedure comprising microwave and electrical heating stages for the

morphology-controlled synthesis of chromium-benzene dicarboxylate, MIL-101(Cr), applicable for CO2 adsorption. *J. Environ. Manage.* **2019**, *250*, 109473.

114. Mu, Q.; He, Y.; Zhang, S.; Chen, H.; Yang, Y.; Qiao, Z.; Zhang, Z.; Wang, X.; Zhao, D.; Wei, Y. Enhanced CO2 Adsorption Affinity in a NbO-type MOF Constructed from a Low-Cost Diisophthalate Ligand with a Piperazine-Ring Bridge. *Chem. Asian J.* **2015**, *10*, 1864–1869.

115. Yu, J.; Zhang, Y.; Lu, J.; Zhou, H.-C. CO2 Capture and Separations Using MOFs: Computational and Experimental Studies. *Chem. Rev.* **2017**, *117*, 9674–9754.

117. Bao, Z.; Yu, L.; Ren, Q.; Lu, X.; Deng, S. Adsorption of CO2 and CH4 on a magnesium-based metal organic framework. *J. Colloid Interface Sci.* **2011**, *353*, 549-556.

118. Caskey, S. R.; Wong-Foy, A. G.; Matzger, A. J. Dramatic tuning of carbon dioxide uptake via metal substitution in a coordination polymer with cylindrical pores. *J. Am. Chem. Soc.* **2008**, *130*, 10870-10871.

119. Wong-Foy, A. G.; Matzger, A. J.; Yaghi, O. M. Exceptional H2 saturation uptake in microporous metal-organic frameworks. *J. Am. Chem. Soc.* **2006**, *128*, 3494-3495.

120. Dietzel, P. D. C.; Besikiotis, V.; Blom, R. Application of metal-organic frameworks with coordinatively unsaturated metal sites in storage and separation of methane and carbon dioxide. *J. Mater. Chem.* **2009**, *19*, 7362-7370.

121. Yu, D.; Yazaydin, A. O.; Lane, J. R.; Dietzel, P. D. C.; Snurr, R. Q. A combined experimental and quantum chemical study of CO2 adsorption in the metal-organic framework CPO-27 with different metals. *Chem. Sci.* **2013**, *4*, 3544-3556.

122. Britt, D.; Furukawa, H.; Wang, B.; Glover, T. G.; Yaghi, O. M. Highly efficient separation of carbon dioxide by a metal-organic framework replete with open metal sites. *Proc. Natl. Acad. Sci. U.S.A.* **2009**, *106*, 20637-20640.

123. Valenzano, L.; Civalleri, B.; Chavan, S.; Bordiga, S.; Nilsen, M. H.; Jakobsen, S.; Lillerud, K. P. Computational and experimental studies on the adsorption of CO, N 2, and CO2 on Mg-MOF-74. *J. Phys. Chem. C* **2010**, *114*, 11185-11191.

124. Drisdell, W. S.; Poloni, R.; McDonald, T. M.; Pascal, T. A.; Wan, L. F.; Liriano, M. L.; Neaton, J. B.; Long, J. R. Probing adsorption interactions in metal-organic frameworks using x-ray spectroscopy. *J. Am. Chem. Soc.* **2013**, *135*, 18183-18190.

125. Zou, Y.; Wang, S. An Investigation of Active Sites for electrochemical CO2 Reduction Reactions: From in Situ Characterization to Rational Design. *Adv. Sci.* **2021**, *8*.

126. Lei, Z.; Zhang, J.; Wu, X.; Luo, L.; Lin, Y.; Chen, B. MOFs-Based Heterogeneous Catalysts: New Opportunities for Energy-Related CO2 Conversion. *Adv. Energy Mater.* **2018**, *8*.

127. Guo, Y.; Liu, X.; Li, X.; Li, Y.; Yan, J.; Huang, Y. Electrocatalytic Reduction of CO2 to CO with 100% Faradaic Efficiency by Using Pyrolyzed Zeolitic Imidazolate Frameworks Supported on Carbon Nanotube Networks. *J. Mater. Chem. A* **2017**, *5* (49), 24867–24873.

128. Pan, Y.; Lin, R.; Chen, Y.; Liu, S.; Zhu, E.; Yuan, S.; Wang, D.; Wang, Y.; Zheng, N. Design of Single-Atom Co-N5 Catalytic Site: A Robust Electrocatalyst for CO2 Reduction with Nearly 100% CO Selectivity and Remarkable Stability. *J. Am. Chem. Soc.* **2018**, *140* (13), 4218–4221.

129. Wang, Y. R.; Liu, Y.; Wu, J.; Yang, X. H.; Zhang, J.; Yuan, Y.; Zhang, L. Oriented Electron Transmission in Polyoxometalate-Metalloporphyrin Organic Framework for Highly Selective Electroreduction of CO2. *Nat. Commun.* **2018**, *9* (1), 520.

130. Zhu, M.; Zhang, M.; Du, Y.; Cheng, F.; Zhang, X.; Chen, J. Covalently Grafting Cobalt Porphyrin onto Carbon Nanotubes for Efficient CO2 Electroreduction. *Angew. Chem., Int. Ed.* **2019**, *58* (19), 6595–6599.

131. Nishihara, H.; Kyotani, T. Synthesis of Ordered Carbonaceous Frameworks from Organic Crystals. *Nat. Commun.* **2017**, *8* (1), 358.

132. Wang, X.; Maeda, C.; Wang, D.; Chen, L.; Yuan, Y.; Zhao, J.; Gong, Y.; Luo, Z.; Zhang, X.; Chen, J. Regulation of Coordination Number over Single Co Sites: Triggering the Efficient Electroreduction of CO2. *Angew. Chem., Int. Ed.* **2018**, *57* (7), 1944–1948.

133. Ye, L.; Liu, X.; Liu, J.; Sun, X.; Zhang, H.; Cui, Y.; Li, Z.; Chen, W.; Liu, J. Highly Oriented MOF Thin Film-Based Electrocatalytic Device for the Reduction of CO2 to CO Exhibiting High Faradaic Efficiency. *J. Mater. Chem. A* **2016**, *4* (39), 15320–15326.

134. Ye, Y.; Sun, D.; Fan, L.; Fu, X.; Zhu, G.; Wei, X.; Zheng, N. Surface Functionalization of ZIF-8 with Ammonium Ferric Citrate toward High Exposure of Fe-N Active Sites for Efficient Oxygen and Carbon Dioxide Electroreduction. *Nano Energy* **2017**, *38*, 281–289.

135. Zhang, X.; Wang, T.; Chang, K.; Ma, Y.; Chen, P. Highly Selective and Active CO2 Reduction Electrocatalysts Based on Cobalt Phthalocyanine/Carbon Nanotube Hybrid Structures. *Nat. Commun.* **2017**, *8* (1), 14675.

136. Huan, T. N.; O'Neill, B. J.; Zhao, Y.; Li, J.; Kumar, B.; Baek, K.; Gewirth, A. A.; Chen, Z. Electrochemical Reduction of CO2 Catalyzed by Fe-N-C Materials: A Structure-Selectivity Study. *ACS Catal*. **2017**, *7* (3), 1520–1525.

137. Dou, S.; Tao, L.; Huo, J.; Wang, S.; Guo, W.; Bao, X. Boosting Electrochemical CO2 Reduction on Metal-Organic Frameworks via Ligand Doping. *Angew. Chem., Int. Ed*. **2019**, *58* (13), 4041–4045.

138. Jiang, X.; Zhang, L.; Wu, K.; Liu, C.; Cao, R.; Lu, Q.; Zhang, J.; Tang, Z. Boosting CO2 Electroreduction to Formate via Bismuth Oxide Clusters. *Nano Res*. **2022**, 1–7.

139. Jiang, X.; Lu, Q.; Liu, C.; Wu, K.; Zhang, J.; Cao, R.; Tang, Z. Boosting CO2 Electroreduction over Layered Zeolitic Imidazolate Frameworks Decorated with Ag2O Nanoparticles. *J. Mater. Chem. A* **2017**, *5* (40), 19371–19377.

140. Kornienko, N.; Zhao, Y.; Kley, C. S.; Zhu, C.; Kim, D.; Lin, S.; Chang, C. J.; Yaghi, O. M.; Yang, P. Metal-Organic Frameworks for Electrocatalytic Reduction of Carbon Dioxide. *J. Am. Chem. Soc*. **2015**, *137* (43), 14129–14135.

141. Zhao, C.; Dai, X.; Yao, T.; Wu, Z.; Wang, C.; Wang, J.; Qiu, J.; Chen, Y.; Zhang, X.; Zhao, X.; Wang, Y. Ionic Exchange of Metal-Organic Frameworks to Access Single Nickel Sites for Efficient Electroreduction of CO2. *J. Am. Chem. Soc*. **2017**, *139* (27), 8078–8081.

142. Wang, Y.; Hou, P.; Wang, Z.; Kang, P. Zinc Imidazolate Metal-Organic Frameworks (ZIF-8) for Electrochemical Reduction of CO2 to CO. *ChemPhysChem* **2017**, *18* (22), 3142–3147.

143. Hod, I.; Deria, P.; Bury, W.; Mondloch, J. E.; Kung, C.-W.; So, M.; Sampson, M. D.; Peters, A. W.; Kubiak, C. P.; Farha, O. K.; Hupp, J. T. Fe-Porphyrin-Based Metal-Organic Framework Films as High-Surface Concentration, Heterogeneous Catalysts for Electrochemical Reduction of CO2. *ACS Catal*. **2015**, *5* (10), 6302–6309.

144. Xiao, T.; Liu, D. The Most Advanced Synthesis and a Wide Range of Applications of MOF-74 and Its Derivatives. *Micropor. Mesopor. Mat*. **2019**, *283*, 88–103.

145. Voskanyan, A. A.; Schneemann, A.; Hey-Hawkins, E.; Dinnebier, R. E.; Kaskel, S. Thermodynamics Drives the Stability of the MOF-74 Family in Water. *ACS Omega* **2020**, *5*, 13158–13163.

146. Howarth, A. J.; Liu, Y.; Li, P.; Li, Z.; Wang, T. C.; Hupp, J. T.; Farha, O. K. Best practices for the synthesis, activation, and characterization of metal-organic frameworks. *Chem. Mater*. **2017**, *29*, 26–39.

147. Kizzie, A. C.; Wong-Foy, A. G.; Matzger, A. J. Effect of humidity on the performance of microporous coordination polymers as adsorbents for CO2 capture. *Langmuir* **2011**, *27*, 6368–6373.

148. Tan, K.; Zuluaga, S.; Gong, Q.; Li, J.; Wojtas, L.; Chabal, Y. J. Water reaction mechanism in metal organic frameworks with coordinatively unsaturated metal ions: MOF-74. *Chem. Mater*. **2014**, *26*, 6886–6895.

149. Zuluaga, S.; Tan, K.; Gong, Q.; Li, J.; Chabal, Y. J. Understanding and Controlling Water Stability of MOF-74. J. Mater. Chem. A **2016**, 4, 5176–5183.

150. Lin, X.; Li, X.; Chen, C.; Jiang, H.; Wang, L. Amino-modified Mg-MOF-74: Synthesis, characterization and CO2 adsorption performance. *Environ. Eng. Res*. **2022**, *28*, 210569-0.

151. Banerjee, R.; Phan, A.; Wang, B.; Knobler, C.; Furukawa, H.; O'Keeffe, M.; Yaghi, O. M. High-Throughput Synthesis of Zeolitic Imidazolate Frameworks and Application to CO2 Capture. *Science* **2008**, *319*, 939–943.

152. Beamish-Cook, J.; Shankland, K.; Murray, C. A.; Vaqueiro, P. Insights into the Mechanochemical Synthesis of MOF-74. *Cryst. Growth Des*. **2021**, *21*, 3047–3055.

153. Appel, A. M.; Bercaw, J. E.; Bocarsly, A. B.; Dobbek, H.; DuBois, D. L.; Dupuis, M.; Ferry, J. G.; Fujita, E.; Hille, R.; Kenis, P. J. A.; Krauss, T.; Machan, C.; McNamara, W. R.; Muckerman, J. T.; Rakowski DuBois, M.; Rakowski, A. M.; Zuccaccia, C. Frontiers, opportunities, and challenges in biochemical and chemical catalysis of CO2 fixation. *Chem. Rev*. **2013**, *113,* 6621–6658.

154. Torrente-Murciano, L.; Mattia, D.; Jones, M. D.; Plucinski, P. K. Formation of hydrocarbons via CO2 hydrogenation – A thermodynamic study. *J. CO2 Util*. **2014**, *6*, 34–39.

155. Wu, J.; Sharma, P. P.; Harris, B. H.; Zhou, X. D. Electrochemical Reduction of Carbon Dioxide: IV Dependence of the Faradaic Efficiency and Current Density on the Microstructure and Thickness of Tin Electrode. *J. Power Sources* **2014**, *258*, 189–194.

156. Tekalgne, M. A.; Pan, J.; Wang, Y.; Yan, Y.; Liu, J.; Li, Y. Two-Dimensional Materials and Metal-Organic Frameworks for the CO2 Reduction Reaction. *Mater. Today Adv.* **2020**, *5*, 100038.

157. Chen, T. L.; Li, X. J.; Li, J.; Guo, L. W.; Zhan, T. G.; Hu, B. In Situ Unraveling of the Effect of the Dynamic Chemical State on Selective CO2 Reduction upon Zinc Electrocatalysts. *Nanoscale* **2020**, *12*, 18013–18021.

158. Hori, Y.; Kikuchi, K.; Suzuki, S. Production of CO and CH4 in Electrochemical Reduction of CO2 at Metal Electrodes in Aqueous Hydrogencarbonate Solution. *Chem. Lett.* **1985**, *14*, 1695–1698.

159. Hori, Y.; Wakebe, H.; Tsukamoto, T.; Koga, O. Electrocatalytic Process of CO Selectivity in Electrochemical Reduction of CO2 at Metal Electrodes in Aqueous Media. *Electrochim. Acta* **1994**, *39*, 1833–1839.

160. Daiyan, R.; Liu, W.; Liu, M.; Yao, T.; Zhang, H.; Song, L.; Sun, L.; Zhang, H.; Wang, Y. Uncovering Atomic-Scale Stability and Reactivity in Engineered Zinc Oxide Electrocatalysts for Controllable Syngas Production. *Adv. Energy Mater.* **2020**, *10*.

161. Nguyen, D. L. T.; Li, J.; Li, X. J.; Li, Y.; Hu, B. Selective CO2 Reduction on Zinc Electrocatalyst: The Effect of Zinc Oxidation State Induced by Pretreatment Environment. *ACS Sustain. Chem. Eng.* **2017**, *5*, 11377–11386.

162. Won, D. H.; Shin, H.; Kim, K. B.; Kim, C.; Kwon, Y.; Lee, H.; Choi, W. Highly Efficient, Selective, and Stable CO2 Electroreduction on a Hexagonal Zn Catalyst. *Angew. Chem. Int. Ed.* **2016**, *55*, 9297–9300.

163. Qin, B.; Liu, W.; Liu, M.; Yang, Y.; Li, L.; Wang, J.; Zhang, H.; Sun, L.; Wang, Y. Electrochemical Reduction of CO2 into Tunable Syngas Production by Regulating the Crystal Facets of Earth-Abundant Zn Catalyst. *ACS Appl. Mater. Interfaces* **2018**, *10*, 20530–20539.

164. Haynes, W. M. CRC Handbook of Chemistry and Physics. *CRC Press*, **2016**.

165. Vollbrecht, S.; Beuge, A.; Blume, C. Federal Institute for Geosciences and Natural Resources. **2022**.

166. Kang, M. P. L.; Kolb, M. J.; Calle-Vallejo, F.; Yeo, B. S. The Role of Undercoordinated Sites on Zinc Electrodes for CO2 Reduction to CO. *Adv. Funct. Mater.* **2022**, *32*.

167. Li, Y. H.; Liu, P. F.; Li, C.; Yang, H. G. Sharp-Tipped Zinc Nanowires as an Efficient Electrocatalyst for Carbon Dioxide Reduction. *Chem. Eur. J.* **2018**, *24*, 15486–15490.

168. Rosen, J.; Hutchings, G. S.; Lu, Q.; Zhu, W.; Zhang, L.; Chen, J. G. Electrodeposited Zn Dendrites with Enhanced CO Selectivity for Electrocatalytic CO2 Reduction. *ACS Catal.* **2015**, *5*, 4586–4591.

169. Geng, Z.; Li, X.; Li, Y.; Zhang, Y.; Li, G.; Chen, Y. Oxygen Vacancies in ZnO Nanosheets Enhance CO2 Electrochemical Reduction to CO. *Angew. Chem. Int. Ed.* **2018**, *57*, 6054–6059.

170. Zhang, T.; Gao, C.; Wei, M.; Hu, P.; Wang, X.; Cao, X.; Wang, Y.; Liu, X.; Sun, X. Multilayered Zn nanosheets as an electrocatalyst for efficient electrochemical reduction of CO2. *J. Catal.* **2018**, *357*, 154–162.

171. Liu, K.; Wang, J.; Shi, M.; Yan, J.; Jiang, Q. Simultaneous Achieving of High Faradaic Efficiency and CO Partial Current Density for CO2 Reduction via Robust, Noble-Metal-Free Zn Nanosheets with Favorable Adsorption Energy. *Adv. Energy Mater.* **2019**, *9*, (2019).

172. Serhan, M.; Sundberg, R. J.; Hsieh, K.; Revzin, A. Total iron measurement in human serum with a smartphone. *AIChE Annual Meeting, Conference Proceedings vols 2019-November* **2019**, (2019).

173. Jiang, X.; Zhang, H.; Tang, Y.; Shen, Y.; Wang, R.; Pan, J. Electrocatalytic reduction of carbon dioxide over reduced nanoporous zinc oxide. *Electrochem. Commun.* **2016**, *68*, 67–70.

174. Lu, Y.; Chen, W.; Wang, Y.; Xie, Z.; Yan, Y.; Su, H.; Wei, X. Efficient electrocatalytic reduction of CO2 to CO on an electrodeposited Zn porous network. *Electrochem. Commun.* **2018**, *97*, 87–90.

175. Jiang, X.; Zhang, H.; Shen, Y.; Wang, R.; Tang, Y.; Pan, J. Carbon dioxide electroreduction over imidazolate ligands coordinated with Zn(II) center in ZIFs. *Nano Energy* **2018**, *52*, 345–350.

176. Zhang, H.; Zhao, M.; Lin, Y. S. Stability of ZIF-8 in water under ambient conditions. *Microporous Mesoporous Mater.* **2019**, *279*, 201–210.

177. Qian, X.; Zhang, H.; Hu, J.; Liu, W.; Song, L.; Yao, T.; Sun, L.; Wang, Y. Enhanced Water Stability in Zn-Doped Zeolitic Imidazolate Framework-67 (*ZIF-67*) for CO2 Capture Applications. *ChemistrySelect* **2018**, *3*, 657–661.

177. Binder, K.; Horbach, J.; Kob, W.; Wolfgang, P.; Fathollah, V. Molecular dynamics simulations. *J. Phys. Condens. Matter* **2004**, *16*.

178. Pappalardo, R. R.; Martínez, J. M.; Sánchez Marcos, E. Application of the Hydrated Ion Concept for Modeling Aqueous Solutions Containing Highly Charged Ions: A Monte Carlo Simulation of Cr3+ in Water Using an ab Initio Intermolecular Potential. *J. Phys. Chem. B* **1996**, *100*, 14725-14730.

179. Martínez, J. M.; Rempe, S. B.; Skaf, M. S. Dynamics of a Highly Charged Ion in Aqueous Solutions: MD Simulations of Dilute CrCl3 Aqueous Solutions Using Interaction Potentials Based on the Hydrated Ion Concept. *J. Phys. Chem. B* **1998**, *102*, 1539-1549.

180. Martínez, J. M.; Pappalardo, R. R.; Sánchez Marcos, E. Coupling a polarizable water model to the hydrated ion-water interaction potential: A test on the Cr3+ hydration. *J. Chem. Phys.* **2000**, *112*, 2339–2347.

181. Martínez, J. M.; Pappalardo, R. R.; Sánchez Marcos, E. Shape and size of simple cations in aqueous solutions: A theoretical reexamination of the hydrated ion via computer simulations. *J. Chem. Phys.* **1999**, *110*, 1669–1676.

182. Bleuzen, A.; Jeannin, Y.; Milet, A.; Kahn, O. Second Coordination Shell Water Exchange Rate and Mechanism: Experiments and Modeling on Hexaaquachromium(III). *J. Phys. Chem. A* **1996**, *100*, 7274-7279.

183. Yazyev, O. V.; Helm, L. Hyperfine interactions in aqueous solution of Cr3+: An ab initio molecular dynamics study. *Theor. Chem. Acc.* **2006**, *115*, 190–195.

184. Akesson, R.; Pettersson, L. G. M.; Sandstrom, M.; Wahlgren5, U. Theoretical Calculations of the Jahn-Teller Effect in the Hexahydrated Copper(II), Chromium(II), and Manganese(III) Ions, [Cu(H2O)6]2+, [Cr(H2O)6]2+, and [Mn(H2O)6]3+, and Comparisons with the Hexahydrated Copper(I), Chromium(III), and Manganese(II) Clusters. *J. Phys. Chem.* **1992**, *96*, 10445-10452.

185. Åkesson, R.; Petterson, L. G. M. Theoretical study of the mono- and di-hydrated divalent ions of the first-row transition metals. *Chem. Phys.* **1994**, *184*, 85–95.

187. Salles, F.; Loiseau, T.; Llewellyn, P. L.; Bourrelly, S.; Serre, C.; Férey, G.; Maurin, G. Molecular Dynamics Simulations of Breathing MOFs: Structural Transformations

of MIL-53(Cr) upon Thermal Activation and CO2 Adsorption. *Angew. Chem., Int. Ed*. **2008**, *47*, 8487–8491.

188. Rosenbach, N.; Maurin, G.; Bourrelly, S.; Llewellyn, P. L.; Kärger, J. Quasi-Elastic Neutron Scattering and Molecular Dynamics Study of Methane Diffusion in Metal Organic Frameworks MIL-47(V) and MIL-53(Cr). *Angew. Chem., Int. Ed*. **2008**, *47*, 6611–6615.

189. Wehmeyer, C.; Schrader, M.; Andrienko, D.; Sebastiani, D. Water-Free Proton Conduction in Hexakis(p-Phosphonatophenyl)benzene Nanochannels. J. *Phys. Chem. C* **2013**, *117*, 12366–12372.

190. Qi, S. C.; Zhang, C. J.; Feng, J. J.; Wang, Y.; Wang, X.; Xu, B. Y.; Liu, Z. M. Fabrication of Porous Carbons from Mesitylene for Highly Efficient CO2 Capture: A Rational Choice Improving the Carbon Loop. *Chem. Eng. J*. **2019**, *361*, 945–952.

191. Frisch, M. J.; Trucks, G. W.; Schlegel, H. B.; Scuseria, G. E.; Robb, M. A.; Cheeseman, J. R.; Scalmani, G.; Barone, V.; Mennucci, B.; Petersson, G. A.; et al. Gaussian 16, Revision C.01. Gaussian, Inc.: Wallingford CT, **2016**.

192. Jorgensen, W. L.; Tirado-Rives, J. The OPLS Potential Functions for Proteins. Energy Minimizations for Crystals of Cyclic Peptides and Crambin. *J. Am. Chem. Soc.* **1988**, *110*(6), 1657–1666.

193. Jorgensen, W. L.; Maxwell, D. S.; Tirado-Rives, J. Development and Testing of the OPLS All-Atom Force Field on Conformational Energetics and Properties of Organic Liquids. *J. Am. Chem. Soc.* **1996**, *118*(45), 11225–11236.

194. Zhu, C.; Byrd, R. H. Algorithm 778: L-BFGS-B: Fortran Subroutines for Large-Scale Bound-Constrained Optimization. *ACM Trans. Math. Softw.* **1997**, *23*(4), 550–560.

195. Bussi, G.; Donadio, D.; Parrinello, M. Canonical Sampling through Velocity Rescaling. *J. Chem. Phys.* **2007**, *126*(1), 014101.

196. Parrinello, M.; Rahman, A. Polymorphic Transitions in Single Crystals: A New Molecular Dynamics Method. *J. Appl. Phys.* **1981**, *52*(12), 7182–7190.

197. Nosé, S.; Klein, M. L. Constant Pressure Molecular Dynamics for Molecular Systems. *Mol. Phys.* **1983**, *50*(5), 1055–1076.

198. Berendsen, H. J. C.; Postma, J. P. M.; van Gunsteren, W. F.; DiNola, A.; Haak, J. R. Molecular Dynamics with Coupling to an External Bath. *J. Chem. Phys.* **1984**, *81*(8), 3684–3690.

199. Páll, S.; Hess, B. A Flexible Algorithm for Calculating Pair Interactions on SIMD Architectures. *Comput. Phys. Commun.* **2013**, *184*(12), 2641–2650.

200. Essmann, U.; Perera, L.; Berkowitz, M. L.; Darden, T.; Lee, H.; Pedersen, L. G. A Smooth Particle Mesh Ewald Method. *J. Chem. Phys.* **1995**, *103*(19), 8577–8593.

201. Larsen, A. S.; Ruggiero, M. T.; Johansson, K. E.; Zeitler, J. A.; Rantanen, J. Tracking Dehydration Mechanisms in Crystalline Hydrates with Molecular Dynamics Simulations. *Cryst. Growth Des.* **2017**, *17*(9), 5017–5022.

202. Martinez, L.; Andrade, R.; Birgin, E. G.; Martínez, J. M. PACKMOL: A Package for Building Initial Configurations for Molecular Dynamics Simulations. *J. Comput. Chem.* **2009**, *30*(13), 2157–2164.

203. Sholl, D. S.; Steckel, J. A. Density Functional Theory: A Practical Introduction. *Wiley-Intersci. Publ.*, **2009**.

204. Moghadam, P. Z.; Li, A.; Wiggin, S. B.; Tao, A.; Maloney, A. G.; Wood, P. A.; Ward, S. C.; Fairen-Jimenez, D. Development of a Cambridge Structural Database Subset: A Collection of Metal-Organic Frameworks for Past, Present, and Future. *Chem. Mater.* **2017**, *29*, 2618–2625.

205. The Cambridge Crystallographic Data Centre.

206. Tomberg, A. Gaussian 09W Tutorial an Introduction to Computational Chemistry Using G09W And Avogadro Software.

207. Lian, J. X.; Siahrostami, S. A molecular insight into the dehydration of metal-organic framework and its impact on the CO2 capture. *Chem. Eur. J.* **2023***, e202203620*, 1-7.

208. Chung, Y. G.; Camp, J.; Haranczyk, M.; Sikora, B. J.; Bury, W.; Krungleviciute, V.; Yildirim, T.; Farha, O. K.; Sholl, D. S.; Snurr, R. Q. Advances, Updates, and Analytics for the Computation-Ready, Experimental Metal-Organic Framework Database: CoRE MOF 2019. *J. Chem. Eng. Data* **2019**, *64*, 5985–5998.

209. Lin, J.-B.; Xiang, S.; Zhang, Z.-J.; Zhou, H.-C. A Scalable Metal-Organic Framework as a Durable Physisorbent for Carbon Dioxide Capture.

210. Al-Attas, T. A.; Burtch, N. C.; Jasuja, H.; Walton, K. S. Ligand-Engineered Metal-Organic Frameworks for Electrochemical Reduction of Carbon Dioxide to Carbon Monoxide. *ACS Catal.* **2021**, *11*, 7350–7357.

211. Bard, A. J.; Faulkner, L. R. Electrochemical Methods: Fundamentals and Applications. *Wiley*, **2001**, *482*.

212. Ooka, H.; Figueiredo, M. C.; Koper, M. T. M. Competition between Hydrogen Evolution and Carbon Dioxide Reduction on Copper Electrodes in Mildly Acidic Media. *Langmuir* **2017**, *33*, 9307–9313.

213. Jiang, X.; Lin, J.-B.; Xiang, S.; Zhang, Z.-J.; Zhou, H.-C. Carbon dioxide electroreduction over imidazolate ligands coordinated with Zn(II) center in ZIFs. *Nano Energy* **2018**, *52*, 345–350.

214. Sassone, D.; Perna, A.; Marotta, R.; Milone, C. Imidazole-imidazolate pair as organo-electrocatalyst for CO2 reduction on ZIF-8 material. *Appl. Energy* **2022**, *324*, 119743.

215. Cho, J. H.; Kim, T.; Kim, D. J.; Jang, S.; Seo, M.; Joo, S. H. Transition Metal Ion Doping on ZIF-8 Enhances the Electrochemical CO2 Reduction Reaction. *Adv. Mater.* **2022**.

Appendix A: Forcefield Parametrization for CO_2 Capture

The bonded and Lennard-Jones parameters of the forcefield for the H_6L_1 ligand were prepared (Figure S1, Table S2 and Table S3), based on the parameters reported for hexakis(*p*-phosphonatophenyl)benzene by Wehmeyer et al. (2013).[190] The parameters corresponding to the dimethyl groups of the mesitylene arms were take from Qi et al. (2019).[191] Finally, the atomic partial charges were calculated at the wb97XD/cc-PVTZ level of theory, after structural relaxation with B3LYP/6-31G++ using Gaussian16 software package.[192]

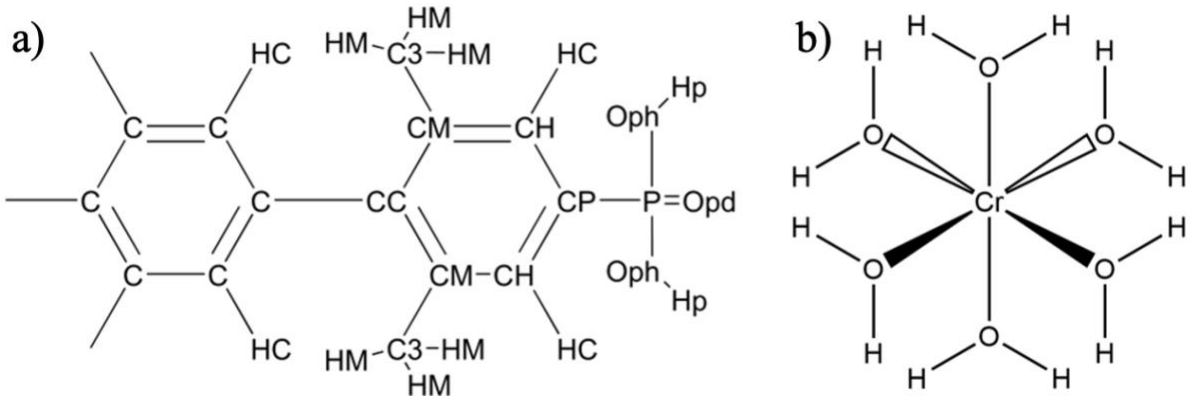

Figure S1: Molecular representation and atom types used in the forcefield for a) H_6L_1 ligand and b) HAC cluster.

In Figure S1a and b we report the Lennard-Jones and bonded parameters of the isolated H_6L_1 ligand and HAC cluster, respectively.

Table S1: Non-bonding parameters for HAC cluster. [a] partial charges *q* are taken from ref [180]; [b] Lennard-Jones parameters of Cr and inorganic oxygen are taken from ref [188]; [c] L-J parameters of water hydrogen taken from TIP4P-Ewald water model.[216]

Atom type	q^a [e]	σ^b [Å]	ε^b [kJ/mol]
Cr	2.45	2.69	0.06272
O	-1.1663	3.12	0.71111
H	0.6284	2.50[c]	0.1255[c]

Table S2: Non-bonding parameters for H_6L_1 ligand. Partial atomic charges *q* were calculated at the DFT level of theory (above).

Atom type	*σ* [Å]	*ε* [kJ/mol]	Reference
C	3.55	0.29288	[190]
CC	3.55	0.29288	
CH	3.55	0.29288	
CP	3.50	0.27614	
HC	2.50	0.12552	
P	3.74	0.83680	
Opd	3.15	0.83680	
Oph	2.90	0.58576	
Hp	0.00	0.00000	
CM	3.62	0.61923	[191]
C3	3.88	0.16318	
HM	2.45	0.15899	

Table S3: Atomic labels and types, partial atomic charges *q*, atomic mass *m* and Cartesian coordinates of the isolated H_6L_1 ligand.

	Atom name	Atom type	*q* [e]	*m* [a.u.]		*x* [nm]	*y* [nm]	*z* [nm]
1	P1	P	1.126	30.9738		5.138	4.414	5.477
2	P2	P	1.126	30.9738		4.44	5.459	5.154
3	P3	P	1.126	30.9738		5.434	5.132	4.409
4	Odp1	Opd	-0.914	15.9994		5.222	4.463	5.594
5	Op1a	Oph	-0.915	15.9994		5.007	4.363	5.531
6	Op1b	Oph	-0.913	15.9994		5.211	4.311	5.391
7	Op2a	Oph	-0.728	15.9994		4.319	5.429	5.057
8	Hp2a	Hp	0.382	1.008		4.271	5.368	5.09
9	Odp2	Opd	-0.775	15.9994		4.49	5.598	5.129
10	Op2b	Oph	-0.819	15.9994		4.4	5.429	5.296
11	Odp3	Opd	-0.815	15.9994		5.376	5.26	4.352
12	Op3a	Oph	-0.735	15.9994		5.407	5.014	4.308
13	Hp3a	Hp	0.383	1.008		5.346	5.036	4.255
14	Op3b	Oph	-0.772	15.9994		5.578	5.138	4.443
15	Cp1	CP	-0.097	12.011		5.108	4.555	5.368
16	C11	CH	-0.112	12.011		5.025	4.537	5.257
17	H11	HC	0.128	1.008		4.985	4.453	5.24
18	C12	CH	-0.421	12.011		5.001	4.644	5.17
19	H12	HC	0.136	1.008		4.944	4.632	5.096
20	Cc1	CC	0.739	12.011		5.059	4.767	5.191
21	C13	CH	-0.421	12.011		5.144	4.784	5.302
22	H13	HC	0.136	1.008		5.186	4.868	5.317

23	C14	CH	-0.112	12.011		5.165	4.677	5.389
24	H14	HC	0.128	1.008		5.222	4.69	5.465
25	Cp2	CP	-0.097	12.011		4.572	5.345	5.109
26	C21	CH	-0.112	12.011		4.703	5.384	5.117
27	H21	HC	0.128	1.008		4.723	5.474	5.137
28	C22	CH	-0.421	12.011		4.807	5.296	5.095
29	H22	HC	0.136	1.008		4.896	5.325	5.105
30	Cc2	CC	0.739	12.011		4.78	5.165	5.058
31	C23	CH	-0.421	12.011		4.649	5.126	5.045
32	H23	HC	0.136	1.008		4.629	5.038	5.018
33	C24	CH	-0.112	12.011		4.546	5.213	5.07
34	H24	HC	0.128	1.008		4.456	5.183	5.062
35	Cp3	CP	-0.097	12.011		5.338	5.089	4.557
36	C31	CH	-0.112	12.011		5.355	5.165	4.674
37	H31	HC	0.128	1.008		5.419	5.234	4.676
38	C32	CH	-0.421	12.011		5.276	5.138	4.787
39	H32	HC	0.136	1.008		5.288	5.189	4.866
40	Cc3	CC	0.739	12.011		5.181	5.037	4.785
41	C33	CH	-0.421	12.011		5.165	4.962	4.667
42	H33	HC	0.136	1.008		5.101	4.892	4.664
43	C34	CH	-0.112	12.011		5.243	4.989	4.557
44	H34	HC	0.128	1.008		5.231	4.937	4.478
45	C1	CC	-0.625	12.011		5.033	4.881	5.098
46	C2	CM	0.408	12.011		4.919	4.962	5.12
47	C3	CC	-0.625	12.011		4.896	5.071	5.031
48	C4	CM	0.408	12.011		4.981	5.097	4.923
49	C5	CC	-0.625	12.011		5.091	5.013	4.903
50	C6	CM	0.408	12.011		5.119	4.906	4.99
51	CT1	C3	-0.374	12.011		4.828	4.938	5.238
52	HM1a	HM	0.079	1.008		4.795	5.024	5.272
53	HM1b	HM	0.079	1.008		4.878	4.892	5.309
54	HM1c	HM	0.079	1.008		4.752	4.882	5.211
55	CT2	C3	-0.374	12.011		4.955	5.21	4.827
56	HM2a	HM	0.079	1.008		4.86	5.212	4.803
57	HM2b	HM	0.079	1.008		5.009	5.197	4.746
58	HM2c	HM	0.079	1.008		4.98	5.295	4.869
59	CT3	C3	-0.374	12.011		5.241	4.82	4.969
60	HM3a	HM	0.079	1.008		5.317	4.859	5.016
61	HM3b	HM	0.079	1.008		5.261	4.816	4.873
62	HM3c	HM	0.079	1.008		5.224	4.73	5.003

Table S4: Atomic labels and types, partial atomic charges *q*, atomic mass *m* and Cartesian coordinates of the isolated HAC residue.

HAC	Atom name	Atom type	*q* [e]	*m* [a.u.]		*x* [nm]	*y* [nm]	*z* [nm]
1	Cr3+	Cr	2.457	51.9961		0	0.862	1.671
2	O1W	O	-1.1663	15.9994		-0.153	0.965	1.74
3	H1Wa	H	0.6284	1.008		-0.222	0.915	1.736
4	H1Wb	H	0.6284	1.008		-0.162	0.991	1.82
5	O2W	O	-1.1663	15.9994		0.153	0.759	1.602
6	H2Wa	H	0.6284	1.008		0.222	0.809	1.606
7	H2Wb	H	0.6284	1.008		0.162	0.733	1.522
8	O3W	O	-1.1663	15.9994		-0.035	0.926	1.492
9	H3Wa	H	0.6284	1.008		0.029	0.979	1.464
10	H3Wb	H	0.6284	1.008		-0.106	0.979	1.491
11	O4W	O	-1.1663	15.9994		0.035	0.798	1.85
12	H4Wa	H	0.6284	1.008		-0.029	0.744	1.878
13	H4Wb	H	0.6284	1.008		0.106	0.745	1.851
14	O5W	O	-1.1663	15.9994		-0.123	0.71	1.635
15	H5Wa	H	0.6284	1.008		-0.113	0.695	1.551
16	H5Wb	H	0.6284	1.008		-0.201	0.735	1.655
17	O6W	O	-1.1663	15.9994		0.123	1.014	1.707
18	H6Wa	H	0.6284	1.008		0.113	1.029	1.79
19	H6Wb	H	0.6284	1.008		0.201	0.989	1.686

References

1. Wehmeyer, C.; Schrader, M.; Andrienko, D.; Sebastiani, D. Water-free proton conduction in hexakis(p-Phosphonatophenyl)benzene nanochannels. *J. Phys. Chem. C* **2013**, *117*, 12366–12372.
2. Qi, S. C.; Wang, J. X.; Zhao, Y.; Xu, J. H.; Tang, J. C.; Jiang, D. L.; Yu, S. H. Fabrication of porous carbons from mesitylene for highly efficient CO2 capture: A rational choice improving the carbon loop. *Chem. Eng. J.* **2019**, *361*, 945–952.
3. Frisch, M. J.; Trucks, G. W.; Schlegel, H. B.; Scuseria, G. E.; Robb, M. A.; Cheeseman, J. R.; Scalmani, G.; Barone, V.; Mennucci, B.; Petersson, G. A.; et al. Gaussian 16, Revision C.01. Gaussian, Inc.: Wallingford CT, **2016**.
4. Pappalardo, R. R.; Martínez, J. M.; Sánchez Marcos, E. Application of the Hydrated Ion Concept for Modeling Aqueous Solutions Containing Highly Charged Ions: A Monte Carlo Simulation of Cr 3+ in Water Using an ab Initio Intermolecular Potential. J*. Phys. Chem*. **1996**, *100*, 4346-4351.
5. Salles, F.; Maurin, G.; Jobic, H.; Llewellyn, P. L. Molecular dynamics simulations of breathing MOFs: Structural transformations of MIL-53(Cr) upon thermal activation and CO2 adsorption. *Angew. Chem. Int. Ed.* **2008**, *47*, 8487–8491.
6. Horn, H. W.; Tars, K.; Wu, C.; Sørensen, J.; Jensen, F.; Jensen, M. Ø.; York, D. M. Development of an improved four-site water model for biomolecular simulations: TIP4P-Ew. *J. Chem. Phys.* **2004**, *120*, 9665–9678.

Appendix B: Charges and Multiplicities Utilized for DFT in CO_2RR

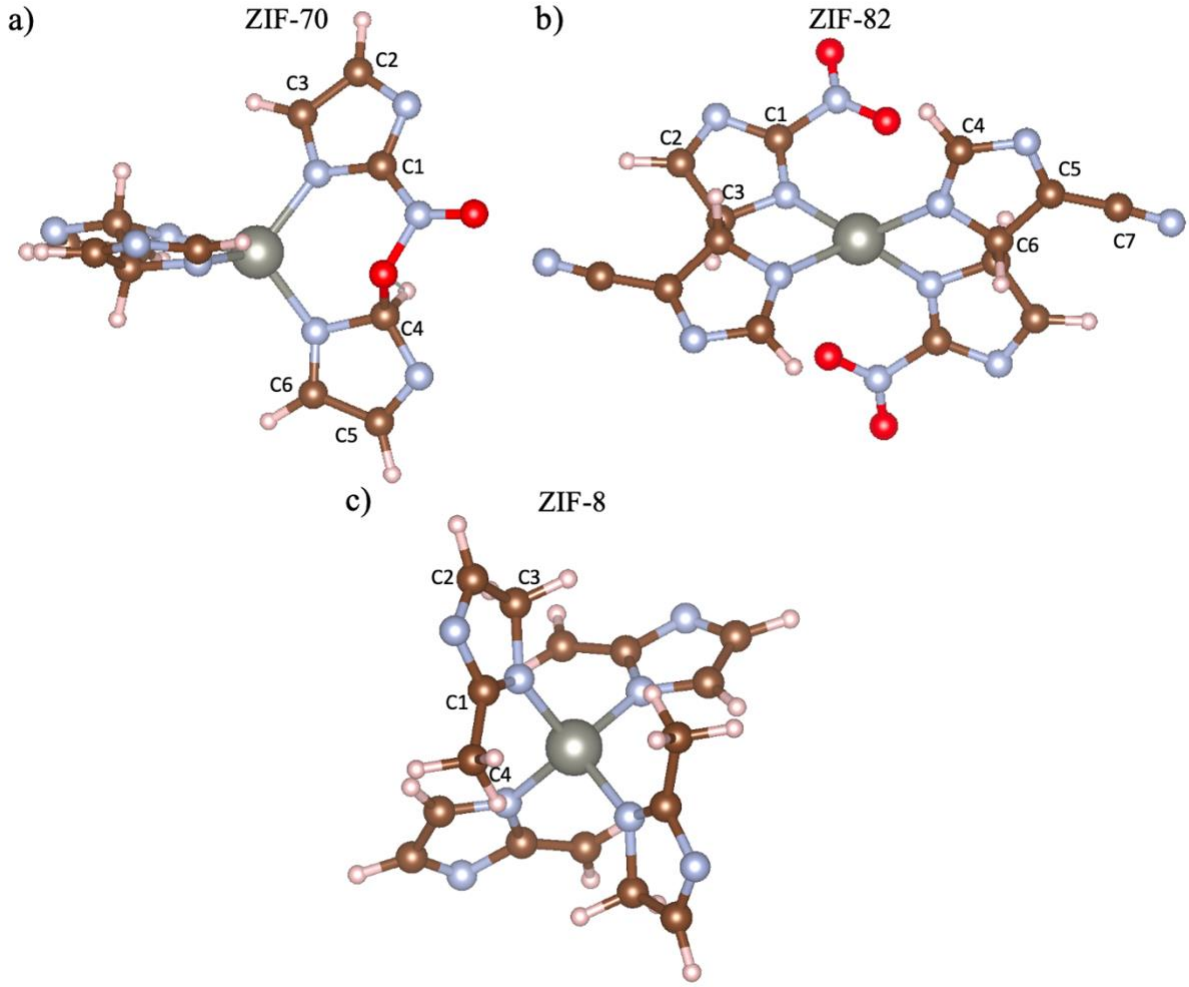

Figure S1: Labelled unit cells for a) ZIF-70, b) ZIF-82, and b) ZIF-8

Table S1: Multiplicity and charge associated with the investigated active sites on ZIF-8

	Clean	Zn_COOH	Zn_CO	C1_COOH	C1_CO	C2_COOH	C2_CO
Multiplicity	1	-	2	2	2	2	2
Charge	2	-	3	2	4	2	4

	C3_COOH	C3_CO	C4_COOH	C4_CO
Multiplicity	2	2	1	1
Charge	2	4	3	4

Table S2: Multiplicity and charge associated with the investigated active sites on ZIF-70

	Clean	Zn_COOH	Zn_CO	C1_COOH	C1_CO	C2_COOH	C2_CO	C3_COOH
Multiplicity	1	2	2	2	2	2	2	2

Charge	2	2	3	2	4	2	4	2
	C3_CO	C4_COOH	C4_CO	C5_COOH	C5_CO	C6_COOH	C6_CO	
Multiplicity	2	2	2	2	2	2	2	
Charge	4	2	4	2	4	2	4	

Table S3: Multiplicity and charge associated with the investigated active sites on ZIF-82

	Clean	Zn_COOH	Zn_CO	C1_COOH	C1_CO	C2_COOH	C2_CO	C3_COOH	C3_CO
Multiplicity	1	2	2	2	2	2	2	2	2
Charge	2	2	3	2	4	2	4	2	4
	C4_COOH	C4_CO	C5_COOH	C5_CO	C6_COOH	C6_CO	C7_COOH	C7_CO	
Multiplicity	2	2	2	2	2	2	1	1	
Charge	2	4	2	4	2	4	3	4	

Initially the energy, ∆E, for the *COOH intermediate on each active site was calculated using the Equation 1:

$$\Delta E_{COOH} = E_{MOF_{COOH}} - E_{Clean\ MOF} - E_{CO_2} - \frac{1}{2}E_{H_2} \quad [1]$$

The ∆E for the *CO intermediate was then calculated using Equation 2:

$$\Delta E_{CO} = E_{MOF_{CO}} + E_{H_2O} - E_{Clean\ MOF} - E_{CO_2} - E_{H_2} \quad [2]$$

Finally, the Gibbs Free Energy, ∆G, was calculated using the Equation 3:

$$\Delta G = \Delta E + \Delta(ZPE - TS) \quad [3]$$

where the ZPE and TS for the *COOH intermediate used was 0.624 eV and 0.178 eV, respectively, and the ZPE and TS for the *CO intermediate used was 0.192 eV and 0.153 eV, respectively.[217]

Table S5: Calculated Gibbs Free Energies for the 2-electron CO_2RR on ZIF-8. The values italicized indicate structure which were converged in an unideal manner. Dashed lines indicate values that could not converge.

Active Site	ΔG_{COOH} (eV)	ΔG_{CO} (eV)
Zn	-	*-2.25*
C1	-3.49	-0.53
C2	-3.88	-1.02
C3	*-3.00*	*0.24*
C4	*6.61*	-

Table S6: Calculated Gibbs Free Energies for the 2-electron CO_2RR on ZIF-70. The values italicized indicate structure which were converged in an unideal manner.

Active Site	ΔG_{COOH} (eV)	ΔG_{CO} (eV)
Zn	*-1.02*	*1.90*
C1	-1.55	2.62
C2	-1.52	1.76
C3	*-1.90*	*2.00*
C4	*-3.51*	*1.81*
C5	-0.72	2.72
C6	*-0.19*	*2.44*

Table S7: Calculated Gibbs Free Energies for the 2-electron CO_2RR on ZIF-70. The values italicized indicate structure which were converged in an unideal manner. Dashed lines indicate values that could not converge.

Active Site	ΔG_{COOH} (eV)	ΔG_{CO} (eV)
Zn	*-0.90*	*2.71*
C1	*-0.08*	*1.44*
C2	-0.82	3.06
C3	*-1.20*	*3.02*
C4	*-0.45*	*3.05*
C5	-0.61	3.60
C6	*-1.58*	*2.34*
C7	*10.42*	-

Calculation of applied voltage:

$$\Delta G = -nFE^o \quad [4]$$

For *COOH intermediate at -0.12 V:

$$\Delta G = \Delta G^o - (1e \times 0.12\,V) \quad [5]$$

For *CO intermediate at -0.12 V:

$$\Delta G = \Delta G^o - (2e \times 0.12\,V) \quad [6]$$

Table S8: ΔG (eV) for ZIF-8, ZIF-70 and ZIF-82 for the applied voltages of 1 V, 0 V, and -0.12 V

Voltage (V)	ZIF-8 (eV)		ZIF-70 (eV)		ZIF-82 (eV)	
	*COOH	*CO	*COOH	*CO	*COOH	*CO
0	-4.23	-1.33	-1.87	1.45	-1.18	2.75
-0.12	-4.35	-1.57	-1.99	1.21	-1.30	2.51
-1	-5.23	-3.33	-2.87	-0.55	-2.18	0.75

Calculation of overpotential:

$$\eta = \Delta G_{CO} - \Delta G_{COOH} \quad [7]$$

Table S9: Calculated overpotentials (V) for ZIF-8, ZIF-70 and ZIF-82.

	ZIF-8 (eV)	ZIF-70 (eV)	ZIF-82 (eV)
η (V)	2.78	0.53	3.21

Calculation of limiting potential:

$$U_L = \eta - E^o \quad [8]$$

Table S10: Multiplicity and charge associated with the investigation of HER on the active sites of ZIF-8, ZIF-70, and ZIF-82

	ZIF-8	ZIF-70	ZIF-82
Multiplicity	2	2	2
Charge	2	2	2

The ΔE for the *H intermediate was calculated using Equation 9:

$$\Delta E_H = E_{MOF_H} - E_{Clean\ MOF} - \frac{1}{2}E_{H_2} \quad [9]$$

The Gibbs Free Energy, ΔG, was calculated using the Equation 3. Where the ZPE and TS for the *H intermediate used was 0.16 eV and 0.007 eV, respectively.[217]

Table S11: Calculated Gibbs Free Energies associated with the investigation of HER on the active sites of ZIF-8, ZIF-70, and ZIF-82

Active Site	ΔG_H (eV)
ZIF-8	-3.35
ZIF-70	0.67
ZIF-82	-0.78

References

1. Peterson, A. A.; Abild-Pedersen, F.; Studt, F.; Rossmeisl, J.; Nørskov, J. K. How copper catalyzes the electroreduction of carbon dioxide into hydrocarbon fuels. *Energy Environ. Sci.* **2010**, *3*, 1311–1315.